Title
Hydrodynamic Exchange in Estuarine Perimeter Habitats

Author
HSU, KEVIN KAI-WIN

Publication Date
2013

Peer reviewed|Thesis/dissertation

Hydrodynamic Exchange in Estuarine Perimeter Habitats

By

Kevin Kai-Win Hsu

A dissertation submitted in partial satisfaction of the

requirements for the degree of

Doctor of Philosophy

in

Engineering – Civil and Environmental Engineering

in the

Graduate Division

of the

University of California, Berkeley

Committee in charge:

Professor Mark Stacey, Chair

Professor Fotini K. Chow

Professor Ömer Savaş

Fall 2013

Abstract

Hydrodynamic Exchange in Estuarine Perimeter Habitats

by

Kevin Kai-Win Hsu

Doctor of Philosophy in Civil and Environmental Engineering

University of California, Berkeley

Professor Mark Stacey, Chair

Hydrodynamic exchange in estuaries is forced by tides, freshwater input, density forcing, and winds, and controls transport of important quantities such as salinity, sediment, nutrients, and pollutants. Previous work has characterized many aspects of estuarine transport and contributed to our understanding of transport mechanisms such as gravitational exchange, tidal dispersion processes, and residual flows due to tidal asymmetries. In general, studies of estuarine transport have focused on large-scale transport processes in the along-channel direction of the estuary, which determine the overall salinity and flow structure in estuarine environments. However, study of hydrodynamic exchange at the perimeter of estuaries has also been recognized to be important, as exchange at the perimeter is relevant for understanding questions related to environmental restoration and management and ecological habitat quality.

In this work, hydrodynamic exchange in estuaries and perimeter habitats is studied using numerical modeling and field observations of South San Francisco Bay. First, the exchange between the estuary and a small perimeter slough is measured using salinity and temperature as tracers to calculate hydrodynamic flushing of the slough through tidal exchange, using a modified tidal prism method. This method applies quasi-Lagrangian analysis to Eulerian measurements of exchange, and the results are compared to previous results from larger-scale estuarine systems, where tidal flushing is found to be significantly affected by the scale of mixing volumes in the system. Next, Lagrangian methods of particle-tracking and Lagrangian coherent structure (LCS) analysis, developed from dynamical systems theory in order to analyze complex, chaotic flows, are applied to analyze tidal transport. The results reveal the significant effects of tidal interactions with perimeter estuarine features on Lagrangian tidal transport over the tidal cycle, where perimeter interactions are found to significantly contribute to longitudinal estuarine dispersion. Finally, the effect of wind forcing on estuarine transport is examined, using Lagrangian analysis methods applied to cases of constant wind forcing with varying wind

direction relative to the main axis of the estuary. Wind forcing is found to have a significant effect on hydrodynamic exchange and connectivity between the estuary and perimeter habitats, where wind in all directions increases perimeter exchange and connectivity, with the greatest effect for winds aligned with the along-axis direction of the estuary. The results of these studies are relevant to a wide range of applications requiring analysis of connectivity near the estuarine perimeter, including sediment exchange and transport and seagrass population colonization in the context of wetland habitat restoration.

Acknowledgements

I would like to thank the members of the UC Berkeley EFM Laboratory for their help in the field data collection at Palo Alto Baylands, as well as research ideas, feedback, and support, and Prof. Mark Stacey for advising and guidance during my dissertation work. Special thanks to Rusty Holleman for help with SUNTANS numerical modeling, computation and coding. I would also like to thank Edward Gross for the use of his FISH-PTM particle tracking model. This work was funded by the California Coastal Conservancy, the National Science Foundation, and the Interagency Ecological Program.

Table of Contents

Chapter 1: Introduction and Motivation

Estuaries are bodies of water where fresh water flow meets the saline water of the ocean, with hydrodynamic forcing such as tides, freshwater input, and density exchange, and meteorological forcing such as wind. Estuaries are sites of great ecological importance because they provide critical habitat for wildlife, and they are also often located near large centers of human populations and used for water for recreation, industry, wastewater disposal, or other uses. The combination of the multiple environmental and economic functions and complex physical forcing makes estuaries a uniquely valuable and challenging area for the study of hydrodynamics, which controls estuarine transport of important quantities such as salinity, sediment, nutrients, biota, and pollutants.

San Francisco Bay is an example of a highly populated, economically and environmentally important estuary where human and ecological demands require careful management of estuarine environmental functions. Wastewater is discharged into the bay at multiple locations, and nutrient loading from the entire heavily agricultural Sacramento-San Joaquin basin enters the bay from the Sacramento-San Joaquin Delta, putting the estuary at possible risk for eutrophication and harmful algal blooms. In addition, salinity and other environmental quantities must be controlled in order to provide high quality habitat for a variety of endangered wildlife species. In particular, significant ongoing environmental restoration projects are intended to restore large areas of wetlands around the perimeter of the San Francisco Bay-Delta which have previously been converted to salt ponds and other human uses, in order to provide environmental and ecological functions such as wildlife habitat and recreation. The success of these restoration projects depends on knowledge of hydrodynamic transport in these perimeter environments, which will determine the effectiveness of processes such as sediment transport and sea grass population propagation in establishing wetland habitats. Hydrodynamic transport is also important for understanding environmental quality and flood control issues in these wetland habitats once they have been established.

The complex physical forcing of estuaries results in transport processes occurring at multiple temporal and spatial scales, and studies of estuaries must be able to separate estuarine transport mechanisms at various scales in order to characterize and analyze them. Temporally, the dominant modes of hydrodynamic transport and exchange in estuaries can often be characterized using tidal timescales, which can be diurnal or semidiurnal. Shorter timescale transport processes include waves and mixing by turbulent eddies, and transport over timescales longer than the tides is important for long-term balances and exchange analyses in estuaries, which can also be affected by longer timescale variations such as spring-neap tidal cycles and seasonal

variations in forcing. Spatial transport scales in estuaries are often set by topography, where large scale topographic and bathymetric features interact with physical forcing to create large-scale hydrodynamic motions, which then feed into smaller-scale turbulent motions. Spatial scales of estuarine transport are also affected by density effects from the salinity distribution in an estuary, where the longitudinal salinity gradient produces baroclinic density forcing which drives vertical gravitational exchange and the vertical salinity gradient produces density stratification which modifies of turbulence through buoyancy effects. The complexity of estuaries in terms of physical forcings and temporal and spatial variability has led to multiple approaches to analyzing estuarine transport, which will be briefly summarized in the following sections.

1.1 Tidally averaged estuarine balances

The simplest models of estuarine transport use mass balances to determine tidally averaged fluxes. Fischer (1979) used tidally averaged mass balances of water and salinity along with assumptions of constant ambient oceanic and estuarine salinities to determine tidal exchange at the mouth of an estuary in terms of freshwater inflow, tidal prism volume, and oceanic and estuarine salinity. In this analysis, a tidal exchange ratio can be computed which represents the ratio of new ocean water to the total volume of water that enters the estuary during a flood tide. A similar approach was also used to determine the mean concentration of effluent in an estuary at a given rate of discharge, where the discharge is diluted by both the freshwater tributary flow entering an estuary at its upstream end and the flow of ocean water circulating in and out of the estuary. These essentially one-dimensional approaches are quite simplified and yet nonetheless can be effective for predicting processes such as pollutant flushing under favorable estuarine conditions.

The tidally averaged momentum and salt balances can be used to analytically predict the tidally averaged, width-averaged structure of flow and salinity in estuaries (MacCready and Geyer 2010). These approaches rely on steady-state assumptions for flow and salinity structure, and estimates of vertical eddy viscosity and diffusivity as well as along-channel dispersion coefficients (e.g. Chatwin 1976, Armi and Farmer 1986). From these balances, analytical solutions for the scale of gravitational exchange circulation in estuaries, where the baroclinic pressure gradient due to the along-channel salinity gradient pushes deeper water into the estuary, and consequent elevation of the surface near the head of the estuary creates a barotropic response which forces surface flow out of the estuary to conserve mass. Turbulent bottom and interfacial stresses balance the barotropic and baroclinic pressure forcing to produce the steady state exchange flow. The exchange flow causes tilting of isohalines, producing a vertical gradient in salinity from the mean longitudinal gradient. Thus both exchange flow and stratification in estuaries depend on the along-channel salinity gradient. This gradient is approximately linear, with estuarine salinity roughly at oceanic salinity at the mouth and decreasing along the length of the salt intrusion towards the head of the estuary. The steady estuarine balance is useful as a framework for analyzing long-term salt budgets in estuaries (e.g. Banas et al. 2004). The

dynamics of the estuarine exchange flow have also been analyzed using salinity classes rather than Eulerian fluxes (MacCready et al. 2002, MacCready 2011).

1.2 Tidal dispersion in estuaries

The effect of tides in estuaries is to produce oscillatory, barotropically forced flows as the tides enter the estuary on the flood tide and exit the estuary on the ebb tide. These periodic tidal flows can in general be much larger in magnitude than the steady flows produced by the freshwater input entering an estuary alone, and thus tidal flows also usually contribute the bulk of turbulent mixing energy to the estuarine systems. Turbulent eddy diffusivity and viscosity are the most important parameters for vertical momentum and scalar transport in estuaries, and although they may be approximated using tidally averaged values (Hansen and Rattray 1966, Chatwin 1976), in reality these quantities are related to the input of turbulent mixing energy from tidally forced flows, and thus vary periodically with the tides. In addition, tidal oscillation generally greatly enhances horizontal estuarine dispersion though interaction of tidal flows with estuarine bathymetric and topographic features, often increasing the effective horizontal dispersion by orders of magnitude over dispersion parameterized by turbulence alone. Thus, tidal effects must be taken into account in any analysis of estuarine hydrodynamics, even in the tidally averaged analyses previously described.

Various approaches can be taken in order to characterize the effect of tides on dispersion in estuaries. One approach is to decompose mass fluxes in estuarine flows into components calculated using tidally averaged, tidally varying, spatially averaged, and spatially varying quantities of Eulerian velocities and scalar concentrations, and analyze each of these components separately, sometimes referred to as a Fischer decomposition (Fischer 1972). The component of the flux calculated from quantities steady in both space and time is the flux determined by one-dimensional estuarine mass balances, such as the steady, depth-averaged flow resulting from riverine freshwater input. The correlation in time of spatially uniform velocity and salinity is referred to as tidal pumping (Stommel and Farmer 1952). Fluxes resulting from correlation of tidally and spatially varying velocities and scalar concentrations characterize transport contributed by tidal oscillation and turbulent diffusion to longitudinal dispersion. The contribution to this term from mechanisms resulting from tidal oscillation is generally much larger than that from turbulent correlations in the absence of oscillatory shear. These mechanisms of longitudinal tidal dispersion can be characterized as oscillatory shear dispersion (Smith 1976, 1983, Fischer 1979), by applying theories of dispersion in turbulent shear flow (Taylor 1954, Elder 1958). The effect of tides on longitudinal dispersion can also be enhanced by a mechanism known as tidal trapping, where scalars are retained by traps created by topographic irregularities. This effect was be quantified analytically using both diffusive exchange (Okubo 1973) and advective exchange (MacVean and Stacey 2011) between the traps and the main channel.

Another method of characterizing the dispersive effect of tidal oscillatory flows is to use a Lagrangian approach to analyze the flow trajectories resulting from complex, spatially and

temporally variable tidal flows. The superposition of the periodic tidal flow with residual currents at different length and time scales can give rise to "Lagrangian chaos" where particles with nearby positions at a given time may follow strongly divergent paths, leading to enhanced dispersion. Zimmerman (1986) analyzed the Lagrangian effect of tidal oscillation on dispersion for a range of estuarine length scales. The tidal dispersion mechanisms were classified into Eulerian regimes of tidal turbulence and a shear-dispersion cascade at smaller length scales, and chaotic Lagrangian regimes of deterministic diffusion and tidal random walk for increasing scale and irregularity of estuarine tidal dispersion. The chaotic nature of advection in estuarine and other oceanic flows has prompted the use of approaches developed from dynamical systems theory to analyze fluid kinematics in such flows (Wiggins 2005). These techniques generally involve analysis of Lagrangian quantities in order to determine their effects on flow structure, such as the Okubo-Weiss criterion, finite-time Lyapunov exponent (FTLE), and finite-scale Lyapunov exponent (FSLE) (Boffeta et al. 2001). A method which has gained popularity in analyzing oceanic flows, and has begun to be applied to analyzing estuarine flows, is the identification of Lagrangian coherent structures (LCS) from ridgelines in spatial FTLE fields (e.g. Branicki and Malek-Madani 2010, Huhn 2012). These LCS have been demonstrated to be useful in identifying transport barriers, and can also often be associated with hyperbolic flow structures (Shadden et al. 2005).

1.3 Estuarine residual flows

The residual flow is defined as the flow which remains after removal of the tidal oscillating flow. This residual flow is therefore important in determining long-term transport in estuaries, over time scales much greater than the tidal period. Tidal residuals can be obtained from Eulerian flow fields through tidal averaging (Fischer 1979), or from Lagrangian trajectories to create tidal Poincaré maps (Zimmerman 1986). Residual flows in estuaries are generally driven by gravitational circulation and interaction of tidally forced flows with estuarine bathymetry. Residual circulation in estuaries is often analyzed in the longitudinal and vertical directions, but transverse residual circulation has also been recognized as important for lateral transport in estuaries (Smith 1976). Lateral salinity gradients produce from lateral straining of the along-channel salinity gradient, i.e. due to bathymetry-induced differential advection during flooding or ebbing tides, can produce secondary transverse gravitational circulation which produces surface convergence and divergence in estuaries on the flood and ebb tides, respectively (Nunes and Simpson 1985). Residual flows produced solely from interaction of tidal flows with lateral depth variation, rather than due to the presence of gravitational circulation from salinity gradients, is also common to many estuaries, including San Francisco Bay, which is a macrotidal shoal-channel estuary with a narrow, deep channel surrounded by broad, shallow shoals, and this bathymetric variation can produce longitudinal and lateral residual circulation.

Li and O'Donnell (1997) analyzed the residual circulation induced by tidal forcing and lateral depth variation in an estuary. Their results were obtained analytically using a perturbation method as applied to an estuary with idealized bathymetry and with the assumption of small tidal

range relative to depth. Nonetheless, their results demonstrate the general mechanisms by which tidal forcing produces residual flows in shoal-channel estuaries. In general, shallower regions of an estuary are more affected by frictional losses of tidal energy at the bed. In contrast, deeper areas have greater momentum and less friction relative to shallow areas, and thus do not respond as quickly to changes in the barotropic tidal forcing. This difference manifests itself as a lag in tidal phasing between areas with lateral variations in depth, with shallow areas leading and deeper areas lagging in tidal phase. For relatively short estuaries, this lag can result in net inward transport for deeper areas and net outward transport for shallower areas.

Li and O'Donnell (2005) extended this analysis to include the effects of channel length relative to the tidal wavelength. Another result of bed friction in estuaries is that as the tidal wave propagates upstream it loses energy, such that the reflected wave at the head of the estuary is smaller in amplitude than the incoming tidal wave. For an estuary with low frictional losses, the incoming and outgoing waves are nearly equal and the tide is close to a standing wave, but as estuary length increases, frictional losses decrease the amplitude of the reflected wave, and the tide behaves more like a progressive wave. The more progressive the tidal wave becomes, the more water mass is transported inward up the estuary, i.e. through Stokes' drift (e.g. Uncles et al. 1985). In estuaries which are long relative to the tidal wavelength, this inward transport creates a set-up at the head of the estuary which in turn drives barotropic return flow which is greatest in the deeper areas of the estuary, such that net residual flow is outward in deeper areas and inward for shallower areas. In both short and long cases, the differences in longitudinal residual currents between areas with lateral depth variation are balanced by lateral residual currents.

Tidal processes can also interact with the estuarine salinity field to influence the residual flow driven by gravitational circulation, for example in strain-induced periodic stratification (Simpson et al. 1990). Here, tidal straining of the horizontal salinity gradient due to vertical velocity shear on the ebb tide tends to tilt isohalines horizontally and increase stable stratification, while tidal straining in the opposite direction tends to tilt isohalines vertically and produce unstable stratification on the flood tide. The opposing effects on stratification affect the vertical eddy viscosity through buoyancy effects, where stable density stratification tends to decrease the effective vertical eddy viscosity and increase vertical shear. This strain-induced stratification effect on the flood and ebb velocity profiles produces tidal asymmetry and net circulation over the tidal cycle.

The three-dimensional structure of estuarine residual circulation is thus a complicated function of tides and salinity. In addition, estuarine circulation can also be significantly affected by wind forcing at the surface of the estuary. The effect of wind forcing in basins without oscillatory flow such as lakes generally sets up downwind transport in shallow areas and upwind return flow in deeper areas (Csanady 1973), and this is also true in idealized estuaries when wind is aligned with lateral depth variation (Wong 1994). Previous studies have analyzed the effects of wind on estuarine circulation and transport, for example using wind forcing aligned in the along-axis direction in idealized estuaries (Chen et al. 2009, Chen and Sanford 2009).

1.4 Summary and research directions in estuarine transport

Because of the complexity of estuarine transport, any study of estuaries must first define the scales and processes of interest for analysis. Transport questions in estuaries can range from the scales of turbulence dynamics such as dissipation and stratified turbulence effects, to tidal scale processes such as tidal straining, to longer term balances of salinity exchange and transport. Processes at each scale depend on and are affected by processes at other scales, but their contributions of each transport mechanism must be analyzed individually to understand the whole.

While the previous sections have provided an introduction to the previous work which has contributed to our understanding of hydrodynamic transport in estuaries, many questions remain regarding hydrodynamic exchange in estuaries. Active areas of research include Lagrangian methods of analyzing estuarine salinity transport and large-scale estuarine circulation, tide- and wind-driven sediment transport processes, and questions related to ecological processes such as transport of biota, habitat connectivity, and population dynamics. All of these topics are relevant to the successful management and restoration of estuarine environments. In particular, recent interest has focused on the estuarine perimeter, which is ecologically important in providing critical habitat for endangered wildlife such as fish and migratory birds. The focus of the research in the rest of this dissertation is on estuarine transport questions as they relate to hydrodynamic exchange in estuaries and their perimeter habitats.

1.4.1 Connections between estuaries and their perimeters

The estuarine perimeter is an area of great importance environmentally and ecologically. Perimeter habitats in estuaries can generally be characterized as shallow habitats with intermediate or varying salinity and relatively high concentrations of sediment and nutrients. They are also often highly dynamic, with tidal activity driving hydrodynamic transport and mixing as well as significant changes in salinity and water depth. Tidal inundation can change the total area of an estuarine environment which is wet or dry, and areas which are always inundated during the tidal cycle are referred to as subtidal, while areas which are inundated at high tide but become exposed at low tide are referred to as intertidal. The perimeter of estuaries thus often provides unique wetland habitat which is highly biologically productive and which provides environmental functions which are important for maintaining the health of estuarine ecosystems. Where large human populations are located near estuaries, the estuarine perimeter is also often the area where human interaction with the environment is the greatest, such as in discharge of pollution, human economic and industrial activity, and recreational activity.

In San Francisco Bay, the estuarine perimeter is particularly important as the site of large-scale efforts to restore wetland habitats around the perimeter of the estuary. The perimeter of the Bay consists largely of salt marsh habitat containing systems of tidal perimeter sloughs. These perimeter sloughs consist of long, narrow, relatively deep channels which are surrounded by either salt marsh vegetation or broad, intertidal mud flat shoals. The hydrodynamic exchange

which controls transport between these perimeter habitats and the rest of the estuary is important for understanding environmental and ecological questions which are relevant to management and restoration efforts. However, hydrodynamic transport processes in estuarine perimeter habitats, characterized by small topographic scales and very shallow, strongly tidal dynamics, have not been well studied.

1.4.2 Questions to be Addressed

The following questions will be addressed in the following chapters:

(1) How can we quantify hydrodynamic exchange between estuaries and perimeter habitats?

(2) What can Lagrangian methods of analysis reveal about estuarine perimeter transport?

(3) What is the effect of wind forcing on estuarine perimeter transport?

The first question is related to the concepts of flushing and residence times, but applied to the much smaller scales of the tidal sloughs which are found in perimeter marsh habitats in estuaries such as San Francisco Bay. This question is addressed in Chapter 2, where the exchange between the estuary and a small perimeter slough is measured using salinity and temperature as tracers to calculate hydrodynamic flushing of the slough through tidal exchange, using a modified tidal prism method. The second question explores the application of Lagrangian techniques such as particle-tracking and LCS to analysis of near-perimeter tidal transport in estuaries. This question is addressed in Chapter 3, where Lagrangian methods of particle-tracking and Lagrangian coherent structure (LCS) analysis, developed from dynamical systems theory in order to analyze complex, chaotic flows, are applied to analyze tidal transport. The third question examines the interaction of wind forcing with tidal flows in estuaries and resulting effects on perimeter exchange and transport. This question is addressed in Chapter 4, where the effect of wind forcing on estuarine transport is examined using Lagrangian analysis methods applied to cases of constant wind forcing with varying wind direction relative to the main axis of the estuary.

These questions will be studied using mostly numerical modeling methods, with some comparisons to field observations. The study of hydrodynamics often requires careful separation of wave and turbulent quantities in time series observational data, as both waves and turbulence produce fluctuations at similar frequencies but represent very different physical phenomena. A study comparing various methods for wave-turbulence decomposition of single-point time series data is included as an appendix to this work.

Chapter 2: Exchange Between an Estuary and an Intertidal Marsh and Slough[1]

2.1 Introduction

Hydrodynamic exchange in estuarine systems is driven by a variety of mechanisms, including density-driven exchange flows, tidal transport and exchange, and shear dispersion. Understanding estuarine exchange is critical to analyzing transport of quantities such as salt, sediments, nutrients, and pollutants which are important for environmental management and restoration. In coastal plain estuaries, the perimeter of the estuary is frequently fringed by critical habitats, such as tidal sloughs and marshes. We can therefore conceptualize the broad estuarine system as consisting of three components, extending from the ocean, through the estuary, to the shallow perimeter habitats that surround it. Exchange between the estuary and these perimeter slough systems may have significantly different hydrodynamic exchange characteristics and dynamics compared to more conventionally studied estuaries, due to differences in physical topography and spatial scale.

The complex time- and space-varying nature of estuarine hydrodynamics, as well as wide variation in physical characteristics between estuarine systems, makes quantifying and analyzing estuarine exchange challenging. There have been many previous studies of hydrodynamic exchange in estuaries, and in this body of literature a wide range of methods have been developed to quantify and analyze estuarine exchange using analytical solutions as well as observational and modeling studies (MacCready and Geyer 2010). These approaches have included tidally averaged balances (e.g. Hansen and Rattray 1965) as well as mixing parameterizations and scaling relations (e.g. Hetland and Geyer 2004). Many mechanisms of estuarine exchange have been described, including tidal asymmetries such as tidal pumping (Stommel and Farmer 1952) and shear dispersion due to oscillatory flows (Fischer et al. 1979). Studies have also explored the spatial structure of the estuarine circulation, including lateral circulation (Fischer 1972; Lerczak and Geyer 2004), as well as tidal effects on stratification and residual circulation, including tidal straining (Simpson et al. 1990).

A common goal in studying hydrodynamic exchange is to characterize exchange using transport time scales such as flushing time, residence time, and water age (Monsen et al. 2002). These transport time scales are useful because they reduce the often complex processes of hydrodynamic exchange down to quantities which can be applied to environmental analyses where the time scale of hydrodynamic transport is an important factor, including pollutant

[1] This work has been reproduced with permission from Hsu et al. (2013).

discharge problems and the study of chemical, biological or ecological environmental processes. Transport time scales can be defined in many ways, and can be broadly categorized as general, large-scale hydrodynamic time parameters defined over a control volume or local hydrodynamic time parameters defined at a specific location (Jouon et al. 2006). A first-order description of a general, large-scale transport time is often referred to as "residence time" or "flushing time", which measures the time scale of water retention within the boundaries of a hydrodynamic system. This flushing time T_f can be calculated as $T_f = V/Q$, where V is volume of the bounded system and Q is the volumetric flow rate through the system (e.g. Monsen et al. 2002; Jouon et al. 2006).

The focus of this study is on exchanges between an estuary and its shallow perimeter habitats. Although at a very different scale, these exchanges are analogous to the exchange between the ocean and an estuary (the ocean's "shallow perimeter habitat"). Ocean-estuary exchange processes have previously been studied using both numerical modeling studies and field observations at a number of different estuaries. Estuarine river plume dynamics have been studied using numerical models to analyze the effects of factors such as vertical mixing, bottom drag, and estuarine circulation (Chao and Boicourt 1986), as well as crossflow velocities and physical scales (O'Donnell 1990). The fate of estuarine water as it exits the mouth of an estuary is the result of interactions between factors such as density dynamics, tidal flows, and topographic and bathymetric effects, which may vary significantly from estuary to estuary (e.g. Valle-Levinson et al. 2003). In estuaries with strong tidal forcing, tidal interactions with topography such as tidal pumping (e.g. Fram et al. 2007) and crossflows at the mouth of the estuary, driven by ocean currents, wind currents, or tides, are likely to be important factors affecting ocean-estuary exchange and flushing dynamics in these systems.

In general, there are two main approaches to studying hydrodynamic exchange in estuaries. Eulerian methods analyze quantities which are fixed in space, whereas Lagrangian methods analyze quantities using a frame of reference which follows the transport of masses within a system. The Eulerian approach is often used because Eulerian measurements are usually simpler to deal with both for collecting measurements and for data analysis. However, due to the complex nature of estuarine mixing and transport, in studying estuarine hydrodynamics often Eulerian methods must be used with caution. For instance, it can be difficult to use Eulerian methods to calculate the net differences in fluxes necessary to analyze estuarine exchange, and in such cases it may be more appropriate to use a Lagrangian or quasi-Lagrangian approach. Studies have demonstrated that methods which use scalars such as salinity and temperatures as tracers can be used to estimate the magnitude of estuarine exchange in a system by using analyses of exchange based on salinity and/or temperature classes (e.g. MacCready and Geyer 2002; MacCready 2011). The use of salinity and temperature scalars in this context can be considered a quasi-Lagrangian approach to studying hydrodynamic exchange, in that although such approaches use Eulerian measurements, salinity and temperature scalars are used in order to keep track of masses of water as they are transported into, within, and out of an estuary, in a

manner similar to the use of Lagrangian tracers. In this study, we will investigate the estimation of estuarine mixing and exchange in a perimeter slough system using such an approach.

Because of the relatively small scales of perimeter sloughs compared to larger estuaries, tidal forcing is likely to be the dominant mechanism of hydrodynamic exchange in such systems, and thus hydrodynamic exchange can be characterized using a residence time based on tidal exchange. To estimate a residence time associated with tidal exchange in perimeter sloughs, we will use a method following a study by MacDonald (2006) and apply it to our system. This approach uses scalar (salinity and temperature) flux data from the mouth boundary of an estuarine system in order to estimate an estuarine residence time using a modified version of the tidal prism method (e.g. Fischer et al. 1979; Sanford et al. 1992). In the tidal prism method, the estuarine residence time is estimated by considering an estuarine volume $V_{estuary}$ which is repeatedly flushed by a tidal prism volume V_I over a tidal cycle with period T. An estimate for estuarine residence time associated with tidal exchange, ERT_T, can be calculated as $ERT_T = (V_{estuary} / V_I)*T$, if we assume both completely well-mixed conditions in the estuary and complete oceanic dilution or flushing of the tidal prism volume after it leaves the estuary (i.e. a return flow factor of 0). This simple estimate can be modified using two parameters, the tidal exchange ratio R (equivalent to 1 minus the return flow factor) and the volumetric exchange ratio M. R represents the fraction of water entering the estuary on each tidal cycle that is "new" ocean water (i.e. not return flow of previously discharged estuarine water) and is a measure of mixing and transport of discharged estuarine water outside the estuary mouth, while M represents the fraction of water leaving the estuary on each tidal cycle that is "new" estuarine water and is a measure of hydrodynamic mixing and replacement processes within the estuary. Thus the two parameters are defined as $R = V_{NO}/V_I$ and $M = V_{NE}/V_I$, where V_{NO} represents the volume of new ocean water entering the estuary on the flood tide, V_{NE} represents the volume of new estuarine water exiting the estuary on the ebb tide, and the tidal prism V_I is the total volume of water entering the estuary on the flood tide. Using R and M, the estuarine residence time associated with tidal exchange can then be estimated as $ERT_T = (V_{estuary} / (RMV_I))*T$ (MacDonald 2006).

The tidal prism method models tidal exchange as simple Eulerian flushing of a bounded estuarine system, but it can also be interpreted as incorporating Lagrangian aspects in its analysis of tidal exchange. In the Lagrangian formulation, the tidal prism method follows a volume of water, the tidal prism ($V_I \approx V_O$), as it is transported back and forth across the mouth boundary between an estuary and the ocean, partially exchanging water volumes with each of these reservoirs during each tidal cycle in two distinct phases. At high tide between flood and ebb, the tidal prism resides within the estuary and exchanges with the ambient estuary water $V_{estuary}$, and at low tide between ebb and flood, it resides outside the estuary and exchanges with ambient ocean water V_{ocean}. The exchange between volumes is modeled using a quasi-well-mixed assumption, where each water volume (estuarine volume $V_{estuary}$, oceanic volume V_{ocean}, and tidal prism $V_I \approx V_O$) is considered well-mixed before and after each tidal exchange "phase", and the amount of water exchanged in each phase is determined by the previously defined exchange ratios $R = V_{NO}/V_I$ and $M = V_{NE}/V_I$. The exchange ratios R and M are thus mixing parameters

which must be used to accurately apply the tidal prism method in order to estimate residence time and characterize hydrodynamic exchange in estuaries.

Methods for estimating *R* have been established in the literature (e.g. Fischer et al. 1979; Sanford et al. 1992), while methods for estimating *M* have been reported only relatively recently, with the introduction of the parameter by MacDonald (2006). The MacDonald (2006) study demonstrated the ability to arrive at an estimate for *M* solely from data collected from the estuarine mouth boundary, which is particularly useful in field studies, where observations are often limited by logistics. In this study we will explore the application of the first method of estimating *M* described in MacDonald (2006). We will refer to this method as the "flux bin method", because the method uses salinity and/or temperature signatures to bin incoming and outgoing fluxes of water masses in order to estimate *M*. The flux bin method has been applied to estuaries such as Mt. Hope Bay (Massachusetts/Rhode Island, USA) in MacDonald (2006), and the goal of this study is to investigate the application of this method to perimeter habitats by applying the method to estimate *M* in a small perimeter slough system. Because of the relatively small scales of perimeter sloughs compared to larger estuaries, in perimeter sloughs the tidal prism volume can be on the scale of or greater than the total system volume, and thus we can expect the strong tidal forcing in these systems to produce significantly different flushing and residence time dynamics in these small-volume systems than in conventionally studied estuaries.

2.2 Methods

The flux bin method, as described in MacDonald (2006), is a method for estimating the volumetric exchange ratio *M* in an estuary, using observations of salinity and temperature fluxes collected at the mouth boundary of the system. The first step in the method is to calculate volume fluxes entering and leaving the system at the mouth through some number of full tidal cycles, binning these fluxes by either salinity or temperature class and considering the direction of the flux into or out of the estuary. These volume fluxes are integrated over time to determine total incoming, outgoing, and net fluxes within each salinity or temperature bin. Once this is done, the volumetric exchange ratio *M* is estimated as $M \approx (\Sigma_{+} V_{net}/\Sigma V_{in})$, where the numerator is the sum across bins of net positive volume flux (directed into the estuary) and the denominator is sum across all bins of the total positive volume flux directed into the estuary. This approach produces an estimate of *M* using only observations of fluxes at the mouth of the estuary, based on the assumption that net volume influx V_{net} is a result of incoming flood water undergoing mixing or replacement through tidal exchange processes, and that this quantity can thus be used to approximate the volume of new estuarine water that exits the estuary on the subsequent ebb tide as a fraction of the incoming volume, such that $M = V_{NE}/V_{I} \approx (\Sigma_{+} V_{net}/\Sigma V_{in})$.

2.3 Observational Data

To analyze exchange between a small perimeter slough system and an estuarine subembayment, we applied the flux bin method to field observations collected from the Palo Alto Baylands Nature Preserve (PAB) in South San Francisco Bay, at a field site containing a

perimeter slough surrounded by tidal marsh habitat. The slough is typical of those in South San Francisco Bay and similar perimeter habitats, with a relatively deep, narrow channel (thalweg depth approximately 3 m below mean sea level, channel width roughly 15-20 m) surrounded by broad, intertidal shoals (Figure 2.1). Field observations were collected at the PAB site over a 2-week period from May 10-24, 2010, a length of time chosen to include spring-neap variation in the tidal cycle. Data was collected at the mouth of the slough using three instrument stations collecting velocity and CTD (conductivity, temperature, depth) data, one in the channel and two in the intertidal shoals (Figure 2.2). The channel station (Station 1) had a moored upward-looking acoustic Doppler current profile (ADCP) collecting velocity profile data, as well as 3 CTDs, one mounted on the frame (bottom) and two attached to a buoyed surface line attached to a clump weight separated from the frame by a line about 5 m in length, with one CTD just below the surface (top) and another CTD 1 m below the surface (mid). Stations 2 and 3 each had two acoustic Doppler velocimeters (ADVs) collecting velocity data at different elevations (25 cm and 65 cm above bed for Station 2 and 25 cm and 50 cm above bed for Station 3), as well as 2 CTDs at each station collecting data at the same heights as the ADVs.

Figures 2.3 and 2.4 show example time series for depth, velocity, salinity, and temperature data collected at the mouth of the slough, from which we can see the range of conditions which are present at the field site. The tidal range varies from 1-2 m; in the channel, maximum ebb velocities are about 1.2 m/s while maximum flood velocities are about 0.4 m/s. This asymmetry can be attributed to the small size of the channel compared to the intertidal regions and the resulting channelization of the flow during ebb tides. The salinity data show wide tidal variation ranging from 12-18 psu at low tide to 20-22 psu at high tide. The temperature data also show wide, mostly diurnal variation, with a range of about 12-24 ° C. The large tidal asymmetries in both flow and salinity mean that Eulerian flux calculations based on instantaneous fluxes (i.e. Fischer 1976) would be extremely vulnerable to errors, and we found such calculations to be unreliable at the site.

2.4 Field Data Processing and Results

Because the velocity data was collected using single-point (ADV) and profile (ADCP) observations at the mouth, an interpolation scheme had to be used to associate normal velocities with flux face areas, in order to calculate volumetric fluxes into and out of the system. Due to bathymetry variations and large differences in water depth and mouth cross-sectional area between high tide and low tide, this interpolation is non-trivial. However, because the flux bin method uses quasi-Lagrangian scalar tracers (S and T) to compare ratios of volumetric fluxes of water entering and leaving the estuary rather than using the absolute magnitudes of fluxes, we can still expect to arrive at reasonable estimates of M using the method even using rough estimates of the flux face areas. For our calculations, the Channel station velocities were assigned flux areas based on vertical ADCP bin height (25 cm) and a width of 15 m representing the average channel width. For the intertidal shoal stations, only the bottom (25 cm above bed) ADV velocities were used, as the shallowness of the water column resulted in the higher ADVs

spending relatively little time collecting data below water. The shoal ADV velocities were thus assigned flux areas based on total water column depth and a width of 150 m for each station.

Figure 2.1: Satellite image of the Palo Alto Baylands Nature Preserve (PAB) in South San Francisco Bay, taken at low tide and revealing bathymetry of the slough channel and intertidal shoals. Locations of the three instrument field stations (Stations 1, 2 and 3) collecting observations across the mouth of the slough are also shown. Inset shows approximate location of field site within South San Francisco Bay.

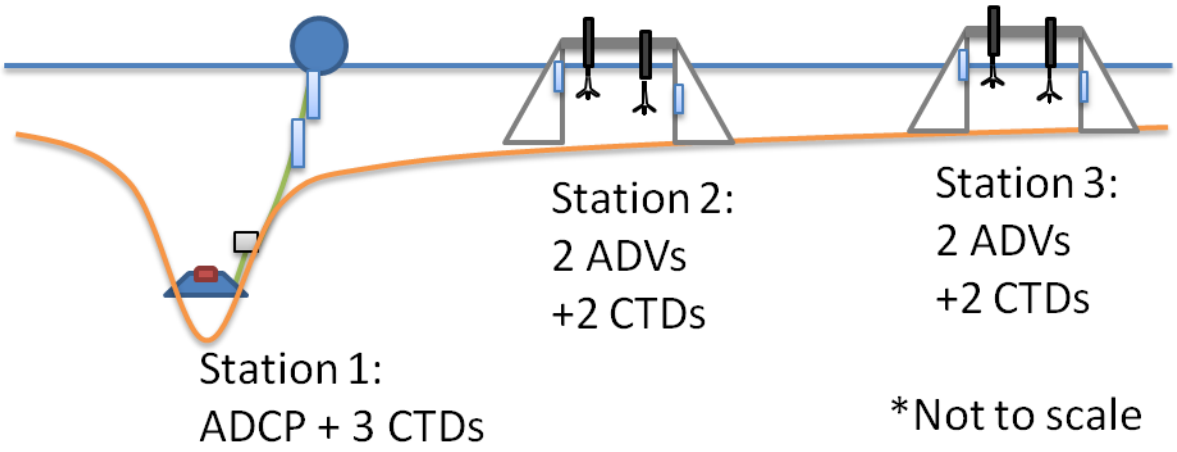

Figure 2.2: Schematic of stations collecting field observations at the Palo Alto Baylands Nature Preserve (PAB) in South San Francisco Bay. Illustration shows cross-sectional layout of the instrument stations and their locations over a representation of the channel-slough bathymetry at

the mouth (not to scale). Perspective is from within the slough looking outwards towards the mouth (see Fig. 2.1), and water level is shown indicating high tide (inundated shoals).

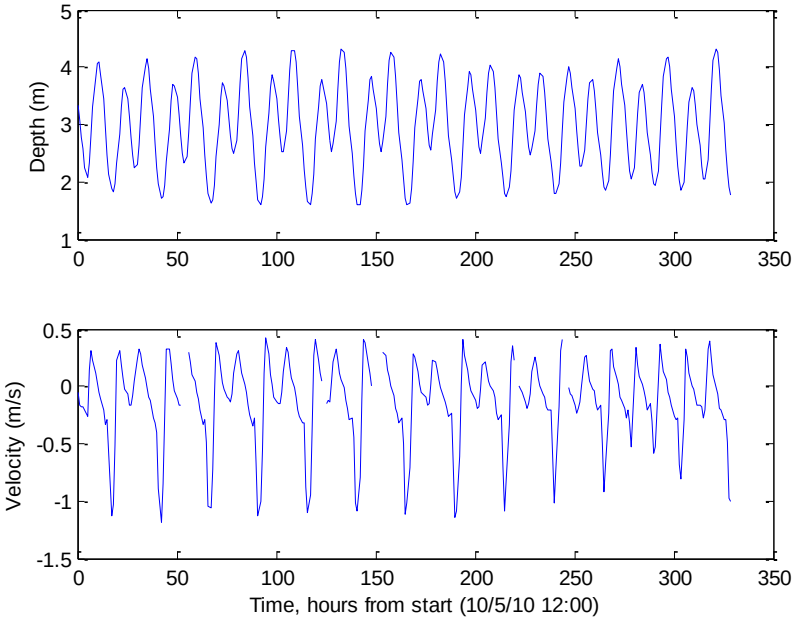

Figure 2.3: Depth and depth-averaged velocity at Station 1, located in the slough channel at the mouth of PAB. Depth varies tidally and shows a spring-neap cycle over about 2 weeks, with tidal range varying from about 1-2 m. Velocity calculated by depth-averaging ADCP data is shown (positive directed into the estuary), with peak depth-averaged flood velocities of about 0.4 m/s and peak depth-averaged ebb velocities of about 1.2 m/s.

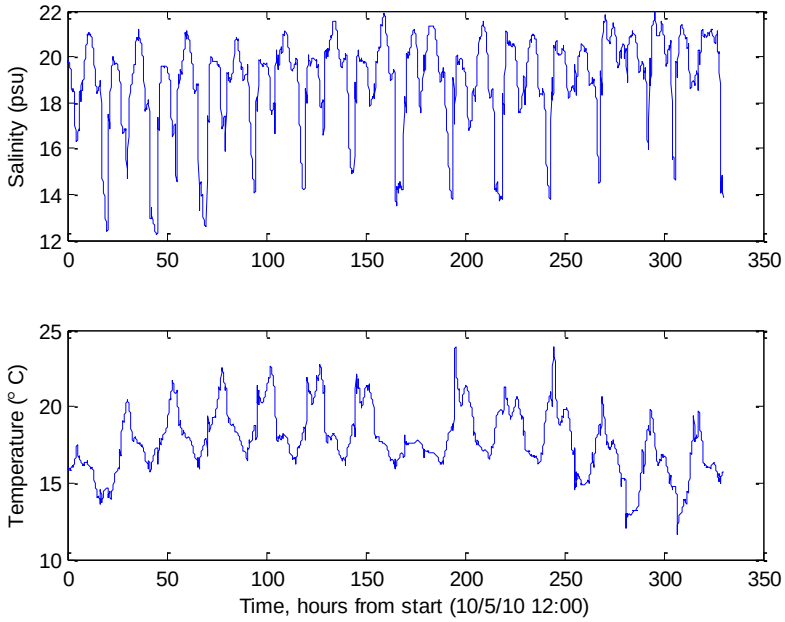

Figure 2.4: Salinity and temperature, averaged over the three sensors (bottom, mid, and top) at at Station 1 located in the slough channel at the mouth of PAB. Salinity varies over a range of 12-22 psu, and temperature varies over a range of 12-24 °C.

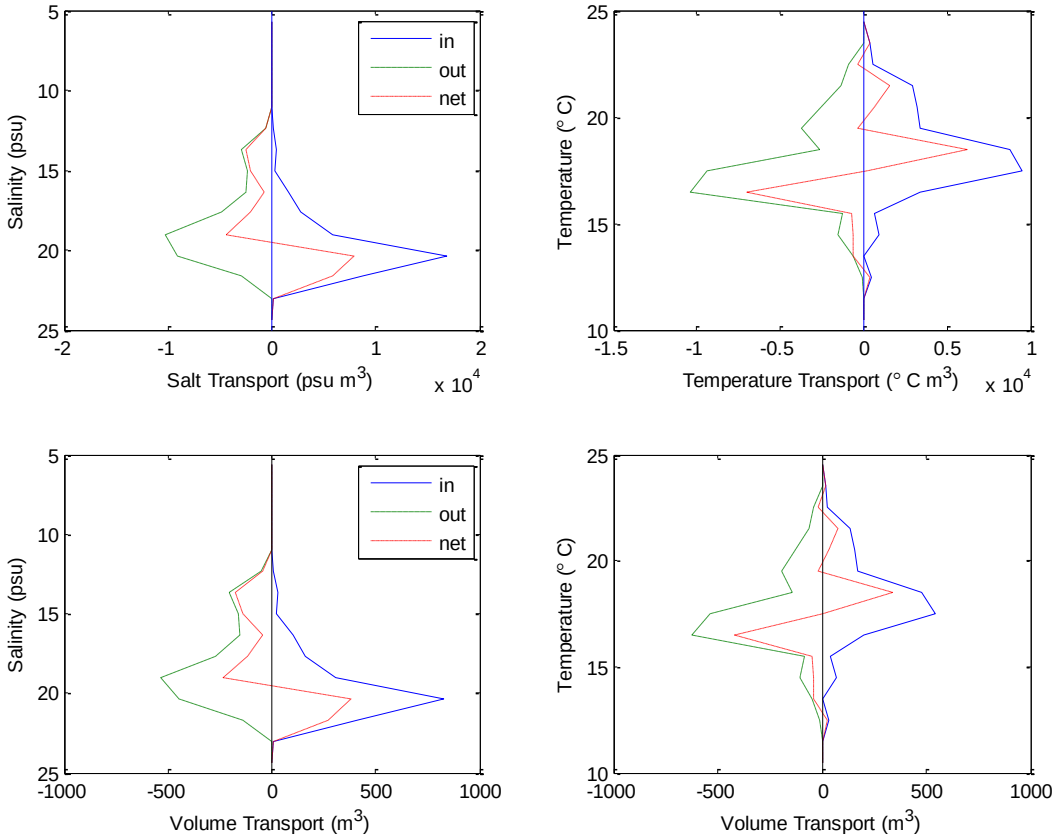

Figure 2.5: Results showing non-depth-averaged salt and temperature fluxes (top) and volume fluxes (bottom) from observations made at the mouth of the PAB slough integrated over 2-week sampling period. Fluxes were binned into 15 scalar classes ranging from 10-15 psu for salinity and from 10-25 °C for temperature. Positive fluxes are directed into the slough (in the flood direction), and negative fluxes are directed out of the slough (in the ebb direction).

To apply the flux bin method to estimate volumetric exchange ratio *M*, flux observations at the mouth of the slough were binned into scalar classes, using either salinity or temperature, over ranges of 5-25 psu for salinity and 10-25 degrees C for temperature (Figure 2.5). For each salinity and temperature class, volume fluxes at the mouth were integrated over the 2-week observation period to calculate total flux into and out of the estuary as well as net flux for each bin. For both salinity and temperature class analyses, *M* was calculated as the ratio of the sum of net volume flux over all scalar bins with positive net flux into the estuary over the total volume flux into the estuary for those bins, such that $M = (\Sigma_{+} V_{net} / \Sigma V_{in})$. Several data interpolation

schemes were tested, including depth-averaged and non-depth-averaged calculations. There was also some evidence in the data that suggested there may have been lateral drift of the floating top and mid CTD sensors at Station 1 towards the shoals during periods of inundation. Interpolation schemes were tested which accounted for this drift, but they did not result in a differences in

	Depth-Averaged	Non-depth-averaged
M (from salinity)	0.3388	0.3568
M (from temperature)	0.3630	0.3492

Table 2.1: Table of results for volumetric exchange ratio M estimated using the flux bin method applied to the field observations at PAB.

estimated *M* of more than 10%. The results for estimating *M* using the flux bin method applied to field observations at PAB are shown in Table 2.1 for cases using either depth-averaged or non-depth-averaged data and using salinity or temperature. The volumetric exchange ratio *M* for the perimeter slough at PAB was estimated to be about 0.35 in all cases. The values of *M* calculated generally agreed between salinity and temperature calculations, despite the likely presence of significant atmospheric temperature fluxes in the estuary which would make temperature non-conservative. The value of the results was found to fluctuate to some degree depending on the number of scalar bins used in the calculation: the initial number used of 15 scalar bins was too low to adequately represent the scalar flux classes for estuarine exchange at the mouth, whereas using a very high number of bins produced noisy results. As a balance between these two limits, an intermediate number of 30 scalar bins was used, which produced consistent results for all cases.

Thus the application of the flux bin method to the field data at PAB resulted in an overall estimate for volumetric exchange ratio of $M \approx 0.35$, and this value appeared relatively insensitive to the various interpolation cases used in the data processing. However, this estimate was significantly higher than previously reported results, for example M = 0.10-0.15 for Mt. Hope Bay in MacDonald (2006). The flux bin method was applied to the field observations in order to use the method to estimate *M* in perimeter slough habitats and gain insight into the nature of flushing and exchange in the system. The large difference between the result for *M* which was obtained from field observations from the small perimeter slough at PAB and the previously reported results for *M* reported by MacDonald (2006) for Mt. Hope Bay raised the question of what might be the cause of this discrepancy in volumetric exchange ratio *M* between sites. We hypothesized that the large difference in values of *M* could be a result of significant differences in the physical system characteristics of perimeter sloughs as compared to other estuarine systems, such as the sharp bathymetry changes between channel and shoal and very large tidal prism volume relative to total system volume. In order to address this question, we turned to numerical modeling in order to further investigate the application of the flux bin method to estimate *M* in small perimeter sloughs.

2.5 Numerical Modeling

The SUNTANS hydrodynamic numerical model (Fringer et al. 2006; Wang et al. 2009) was used to investigate the results obtained from application of the flux bin method to the field observations at PAB. Shoreline and bathymetric data representing the perimeter slough at the PAB field site were used to create an unstructured numerical grid model for the system, with spatial resolution ranging from 300 m in the open South Bay to 3 m within the slough (Figure 2.6). To simplify the analysis of the estimation of exchange using the flux bin method in the model results, only tidal forcing was used, and other physical forcings such as density/baroclinic exchange, salinity and freshwater input, and wind effects were not included. The hydrodynamic model solved the depth-averaged shallow-water equations, where a depth-averaged hydrodynamic model was determined to be appropriate for analyzing exchange at this site because the shallow and energetic nature of the system would presumably reduce the overall importance of baroclinic processes. The hydrodynamics were forced with idealized M2 tides (sinusoidal tides with period T of 12.4 hours) at the oceanic boundary of the model. The amplitude of the tidal forcing was varied between 1 cm and 1 m to test the response of the system to varying strength of tidal forcing, which also resulted in a wide range of ratios of tidal prism volume to total system volume.

To analyze the results of applying the flux bin method to the model to estimate the volumetric exchange ratio M, a passive tracer was released and tracked in the model. Model runs were designed to observe the volumetric exchange ratio by initializing the runs at the low tide phase of the tidal cycle, using a tracer to tag "estuarine" (slough) water within the boundaries of the PAB with a tracer concentration of 1 and "oceanic" (bay) water outside the slough with a tracer concentration of 0. For each tidal amplitude case, the hydrodynamic model was initialized in this way (after a hydrodynamic spin-up period of 2 days) and then run for a period of 4 simulation days, or about 8 tidal cycles (each cycle consisting of a flood tide and then an ebb tide). Qualitative model validation showed that the model produced velocities similar in range to those observed at the PAB field site. The numerical results were analyzed by measuring the tracer both as integrated "mass" within the slough system volume and using fluxes across the mouth cross-sectional boundary of the slough.

2.5.1 Methods

To calculate the volumetric exchange ratio M from the model output, two methods were used. The first method, which we will call the "mass ratio method", effectively allowed direct calculation of M from its definition using only the first tidal cycle (after initialization of the tracer at low tide) for each numerical model run. In this method M was calculated by integrating the total "mass" of the tracer within and outside the system volume, thus using tracer mass to keep track of volumes of water entering and leaving the system. Because the model is forced with constant, idealized tides, each tidal cycle is identical and the volume of the system is unchanged after each tidal cycle, which greatly simplifies our analysis of tidal exchange. Consequently, the volume of oceanic water within the system after the first tidal cycle (low tide

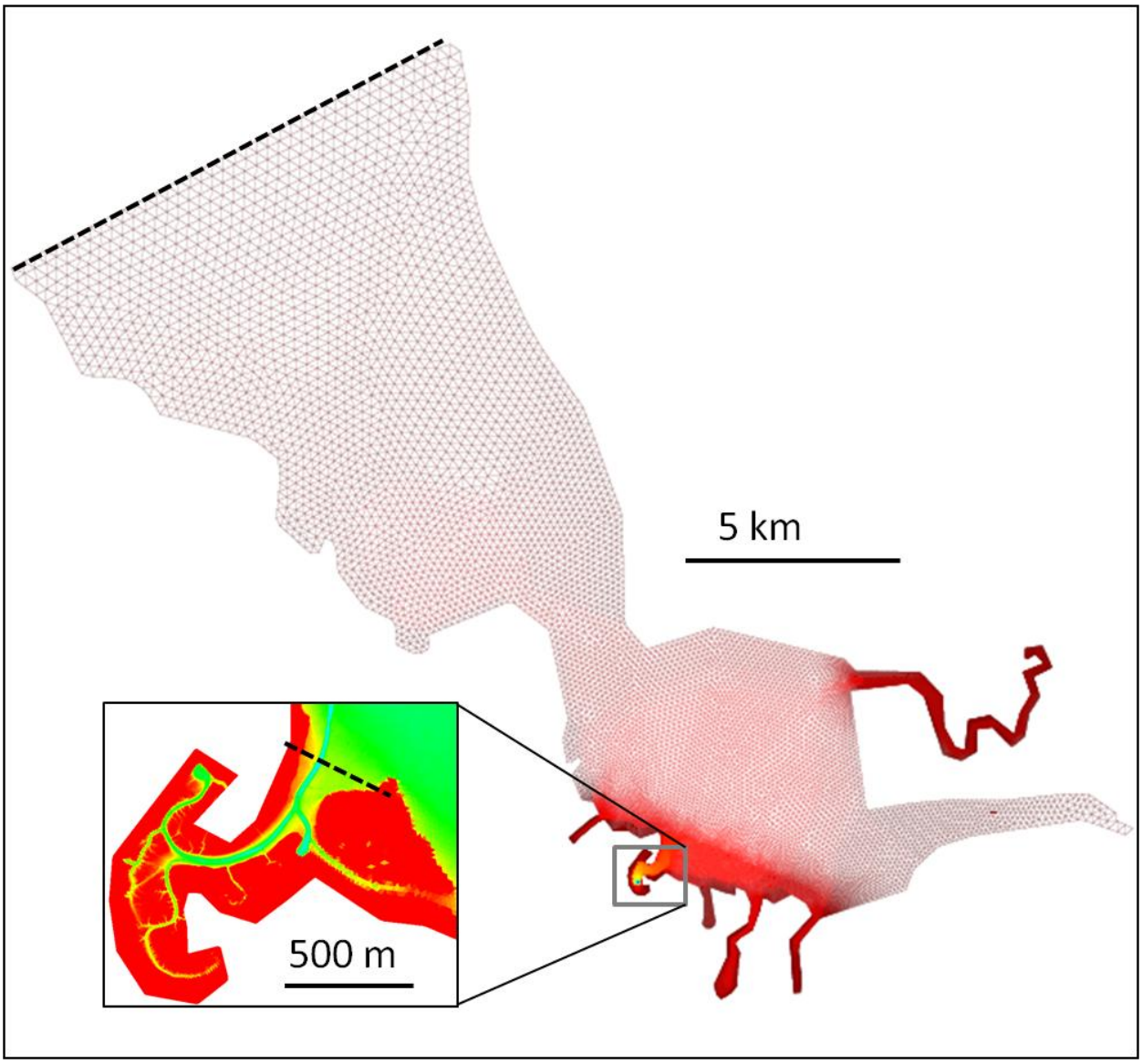

Figure 2.6: Grid domain used for SUNTANS numerical hydrodynamic modeling of South San Francisco Bay. The model used a unstructured grid with grid scales ranging from 3 m within the PAB slough to 300 m in the open South Bay. The model was forced using idealized tides at the open boundary (black dotted line), which is co-located with the San Mateo Bridge in South San Francisco Bay. Inset shows bathymetry at Palo Alto Baylands, with black dotted line indicating mouth boundary for calculating fluxes into and out of the slough system.

to low tide, i.e. flood then ebb) is equivalent to the amount of estuarine water exchanged, or V_{NE}. The volume of new estuarine water V_{NE} was therefore measured as the total integrated mass of "oceanic" water (tracer concentration 0) which was present within the volume of the slough system at low tide after the first tidal cycle. Tidal prism V_I was measured as the difference in high tide and low tide volume in the slough complex. Volumetric exchange ratio M was then calculated according to its definition as $M = V_{NE}/V_I$.

The second method used was the flux bin method (MacDonald 2006), but applied to the model output rather than field observations. A major difference in the application of the flux bin method to the numerical results as compared to the field observations was that because fluxes across the mouth boundary of the slough system were able to be calculated and obtained for each location in the numerical model, no interpolation of flux data at the mouth was necessary. Also, a much larger amount of flux data was available from the model output, so there was much greater flexibility in the number and size of tracer concentration bins used, and thus the bin size was chosen to maximize resolution of the tracer flux classes within the limits of noise (80 scalar bins were used in the calculations).

2.5.2 Results

The results for the volumetric exchange ratio M for both the mass ratio method and the flux bin method are shown in Table 2.2. The application of the mass ratio method to the numerical modeling results produced estimates for M ranging from 0.044 to 0.25 for tidal amplitudes of 1 m and 1 cm, respectively. The results of the flux bin method applied to the model output produced higher estimates for M, roughly 0.2-0.25 for all cases. These results are significantly higher than the results calculated from the mass ratio method, except for in the 1 cm case.

These results for M from the mass ratio method and the flux bin method can be compared to another calculated quantity, the ratio of low tide volume to tidal prism volume (V_{LT}/V_I), which is seen to vary oppositely with the amplitude of the tidal forcing (Table 2.2). For our model, this ratio should be a theoretical upper bound on $M = V_{NE}/V_I$, due to the fact that the volume of new estuarine water exchanged during the tidal cycle cannot be greater than the volume of water residing in the system at low tide (true in the model because there is no "riverine" input, i.e. $Q_R = 0$). Therefore, in our model $V_{NE} \leq V_{LT}$, which limits the range of possible magnitudes for $M = V_{NE}/V_I$ for large tidal forcing to $M \leq V_{LT}/V_I$. From comparing the results for M from the mass ratio method and the flux bin method to the model "limit" of V_{LT}/V_I, we see that for all results for the mass ratio method and for most results for the flux bin method, the estimate produced for M

Tidal Amplitude	$M = (V_{NE} / V_I)$ (From mass ratio method)	$M \approx (\Sigma_+ V_{net} / \Sigma V_{in})$ (From flux bin method)	(V_{LT} / V_I) (Ratio of low tide volume to tidal prism)
1 m	0.044	0.22	0.09
30 cm	0.058	0.18	0.38
10 cm	0.12	0.22	1.76
1 cm	0.25	0.24	21.0

Table 2.2: Comparison of results for volumetric exchange ratio M calculated from numerical model results using the mass ratio method and the flux bin method. Four modeling cases which were forced using a range of tidal amplitudes from 1 m to 1 cm (using idealized 12-hour period sinusoidal tides) are shown. The theoretical upper limit in the model for M is (V_{LT}/V_I), also shown for comparison.

is below the limit $M \leq V_{LT}/V_I$. However, in the 1 m amplitude tidal forcing case, the result for M is significantly larger than the V_{LT}/V_I model limit. The limits for volumetric exchange ratio M in the model and in estuarine systems in general will be analyzed in more detail in the discussion section below.

2.6 Discussion

2.6.1 Calculating Volumetric Exchange Ratio (M): Estimating Residence Time Based on Tidal Mixing

Before we discuss the results of estimating the volumetric exchange ratio M from the field observations and numerical modeling results, it is worth revisiting the definition of M, because this definition is key to interpreting our results for the value of M and understanding its application in calculating estuarine residence times based on tidal exchange. Recall that M is one of two ratios associated with tidal exchange as modeled using the tidal prism method, each being defined as $R = V_{NO}/V_I$ and $M = V_{NE}/V_I$. These parameters are defined so that they can be used to estimate an estuarine residence time associated with tidal exchange, ERT_T, calculated as $ERT_T = (V_{estuary}/(RMV_I))*T$, where the residence time is estimated using the flushing time equation $T_f = V/Q$ by substituting $T_f = ERT_T$, $V = V_{estuary}$, and Q as $(R*M*V_I)/T$. From these equations we can see that R and M are used as scaling factors which are multiplied by the tidal prism V_I in order to obtain the volume of water removed from the system on each tidal cycle, which is then used in conjunction with the tidal period T to approximate the tidal flushing rate Q in the residence time calculation.

To more clearly understand the physical interpretation of M in this calculation, we can simplify the situation by assuming for the purposes of this discussion that the tidal exchange ratio $R = 1$, which is equivalent to saying that $V_{NO} = V_I$, or that there is complete flushing of ebb water upon exiting the estuary mouth and that all of the incoming tidal prism V_I consists of new ocean water V_{NO}. In this case $Q = (R*M*V_I)/T = V_{NE}/T$, so we see that definition of $M = V_{NE}/V_I$ is simply a means of obtaining the flushing volume (in this case V_{NE}) from the tidal prism (V_I) to calculate the tidal flushing rate Q and ultimately the estuarine residence time. Included in this flushed volume V_{NE} is water that is flushed by a combination of two mechanisms: estuarine water can either first mix with ocean water within the estuary before exiting the estuary (thus changing the salinity signature of the oceanic water), or estuarine water may simply be expelled from the estuary without mixing (thus being "directly replaced" by oceanic water which is retained or "lost" within the estuary). Both estuarine mixing and replacement processes act to flush estuarine water through tidal exchange, and both mechanisms result in the net flux of water out of the estuary at estuarine scalar classes (corresponding to net positive influx of water into

the estuary at oceanic scalar classes). Thus the tidal prism method does not explicitly distinguish between the two mechanisms of estuarine flushing, and "tidal exchange" as considered in our analysis includes both mixing and replacement processes.

It is important to note here that although V_{NE} represents the volume of estuarine water flushed from the system, it does not necessarily represent the volume of incoming tidal water V_I which is mixed or replaced within the estuary. To demonstrate this, we can analyze the tidal exchange processes which occur within the estuary during the high tide phase of a tidal cycle (between flood and ebb) by considering the interaction between two volumes of water, the incoming tidal prism V_I and the estuarine low tide volume V_{LT}. In doing so, we will introduce a number of variables describing volumes of water and other related quantities, and a table summarizing the relevant variables is provided in Table 2.3. During this phase, there are fractions of V_{LT} and V_I which do not interact, undergoing no tidal exchange, and these fractions can be defined as "unchanged" volumes V_{UE} and V_{UI} for estuary and incoming volumes, respectively. The remaining fractions of V_I and V_{LT} undergo mixing and replacement processes through tidal exchange, and we can define these as the tidally "active" volumes V_{AE} and V_{AI} for estuary and incoming oceanic volumes, respectively. We can thus divide the incoming tidal prism into "unchanging" and "active" parts so that $V_I = V_{UI} + V_{AI}$, and similarly we can define an "outgoing active" volume V_{OA} representing the part of the outgoing tidal prism V_O which has been modified between flood and ebb, such that $V_O = V_{UI} + V_{OA}$, and if we apply mass conservation $V_O = V_I + Q_R*T$, we find that $V_{OA} = V_{AI} + Q_R*T$.

Now if we consider that the volumes V_{AE} and V_{AI} exchange with each other through some combination of mixing and direct replacement, we find that a part of the combined volume ($V_{AE} + V_{AI}$) subsequently exits the estuary on the ensuing ebb tide as the volume V_{OA} with some proportion of new estuarine water which we define as $C_{OA} = V_{NE}/V_{OA}$. Remember that $V_O = V_{UI} + V_{OA}$ (where by mass conservation V_{OA} is equal in volume to $V_{AI} + Q_R*T$), with the key difference between V_{UI} and V_{OA} being that V_{UI} remains unchanged and thus exits the estuary on the ebb with the same oceanic scalar class it entered with on the previous flood, while V_{OA} represents the fraction of V_O which has undergone tidal exchange processes and thus exits the estuary with a different, estuarine scalar class. The true amount of new estuarine water exiting the estuary on the ebb V_{NE} (and thus the value C_{OA}) depends on the nature of the exchange processes between the "active" estuarine and incoming tidal volumes V_{AE} and V_{AI}. In the case of direct replacement only, all of V_{OA} is new estuarine water, or $V_{NE} = V_{OA}$ and $C_{OA} = 1$. In the case of "simple" (complete) mixing between V_{AE} and V_{AI}, C_{OA} is equal to the mixed proportion $C_M = V_{AE}/(V_{AE} + V_{AI})$, which can range from 0 to 1, and $V_{NE} = V_{OA}*C_M$. In reality, the exchange between V_{AE} and V_{AI} can be a combination of direct replacement and mixing (with inhomogeneous mixing resulting in potentially multiple modes of mixing, each with a different mixing proportion C_M), but for our analysis these two simple cases of only direct replacement or only complete mixing will suffice as examples. If we use the approximation $V_I \approx V_O$ (valid if Q_R*T is much smaller than the tidal prism, as when tidal exchange is the dominant mechanism of flushing), then $V_{OA} \approx V_I - V_{UI} = V_{AI}$. Thus if we have only direct replacement and no mixing,

then from the above analysis we have $V_{NE} = V_{OA} \approx V_{AI}$, and the relationship between the new estuarine volume V_{NE} and the incoming tidal prism V_I is relatively simple, so that the volumetric exchange ratio $M = V_{NE}/V_I \approx V_{AI}/V_I$. However, when mixing is included as an exchange mechanism when considering the effects of tidal exchange processes, the relationship between V_{NE} and V_I becomes more complicated: for the simplest case, the complete mixing case, we

T	Tidal period
Q_R	Volume flowrate of riverine freshwater input
V_I (incoming tidal prism)	$V_I = V_O - Q_R*T$
V_O (outgoing tidal prism)	$V_O = V_I + Q_R*T$
M (volumetric exchange ratio)	$M = V_{NE}/V_I$
R (tidal exchange ratio)	$R = V_{NO}/V_I$
V_{NE} (volume of new estuarine water)	$V_{NE} = M*V_I$
V_{NO} (volume of new oceanic water)	$V_{NO} = R*V_I$
ERT_T (estuarine residence time for tidal exchange)	$ERT_T = (V_{estuary}/(RMV_I))*T$
$V_{estuary}$ (volume of estuary)	$V_{estuary} = V_{LT} + (1-R)*V_I$
V_{LT}	Volume of estuary at low tide
V_{UE} (volume of unchanged estuarine water)	$V_{LT} = V_{UE} + V_{AE}$
V_{AE} (volume of active estuarine water)	$V_{LT} = V_{UE} + V_{AE}$
V_{UI} (volume of unchanged incoming water)	$V_I = V_{UI} + V_{AI}$
V_{AI} (volume of active incoming water)	$V_I = V_{UI} + V_{AI}$
V_{OA} (volume of outgoing active water)	$V_O = V_{UI} + V_{OA}$
C_{OA} (proportion of new estuarine water)	$C_{OA} = V_{NE}/V_{OA}$
C_M (proportion for complete mixing)	$C_M = V_{AE}/(V_{AE} + V_{AI})$ (for simple complete mixing)
f (inflation factor)	$f = V_{AI}/V_{NE}$
M_f	$M_f = f*M = V_{AI}/V_I$
V_{net} (used in flux bin method to estimate M)	$M \approx (\Sigma_+ V_{net}/\Sigma V_{in}) \approx V_{AI}/V_I$

Table 2.3: Summary table of variable descriptions and definitions. Relevant equations and variable relationships are provided for context.

obtain $V_{NE} = V_{OA}*C_M \approx V_{AI}*C_M$, where $C_M = V_{AE}/(V_{AE} + V_{AI})$, and $M \approx (V_{AI}/V_I)*C_M$ (with modified results when allowing for multiple modes of mixing and/or when combining with the result for direct replacement).

As mentioned above, the tidal prism method does not explicitly distinguish between mixing and replacement processes, but as this analysis shows, the differences in these exchange mechanisms have significant effects on the overall flushing of new estuarine water V_{NE} through tidal exchange and thus on calculation of the volumetric exchange ratio $M = V_{NE}/V_I$. The consequences of these differences may be especially important in small-volume systems such as PAB where strong tidal forcing by the large tidal prism compared to system volume increases the relative strength of mixing processes over direct replacement, and this should be kept in mind when analyzing the results of estimating M by applying the flux bin method to numerical modeling and field observations as we have done in PAB.

2.6.2 Calculating and Interpreting M in Small-Volume Systems

Before discussing the specific results obtained for the estimating M from the PAB model using the flux bin method, we will first consider how the conditions in the model system affect how those estimates should be interpreted. As mentioned previously, in the model $M = V_{NE}/V_I$ can be considered to have a limit of V_{LT}/V_I, since the amount of estuarine water flushed from the system V_{NE} in the model cannot exceed the amount of water available in the system, which is equal to the low tide volume V_{LT} due to the absence of freshwater input Q_R (i.e., $V_{NE} \leq V_{LT}$ for a closed system). Any result for M that is above this limit, such as for the 1 m amplitude case, is essentially nonphysical, saying that a larger volume V_{NE} is flushed from the system than is actually available, that is the low tide storage V_{LT} ($V_{NE} > V_{LT}$). More generally, we can say that the amount of water available for exchange in a small-volume system using a closed model would be the sum of the low tide storage volume V_{LT} and the freshwater input Q_R over a tidal period, so that the upper limit for M would be $(V_{LT} + Q_R*T)/V_I$. The volume $(V_{LT} + Q_R*T)$ can be considered an absolute limit on the amount of water available for exchange only for models with closed boundaries; in the real world, estuaries are not closed at the head, so the amount of water available for tidal exchange is limited only by the extent of estuarine water that can access the tidal prism. In general, this volume is likely equal to or less than the theoretical limit of $(V_{LT} + Q_R*T)$, because the tidal prism is not likely to exchange with water upstream of the defined head of the estuary. Therefore, a limit of $(V_{LT} + Q_R*T)/V_I$ is still useful as a scaling estimate for what we can expect the upper bound of M to be in small-volume systems (i.e., $V_I > (V_{LT} + Q_R*T)$), and in the model it can be used to indicate when the flux bin method is giving us results which are nonphysical, that is if the estimate obtained for M results in $M > (V_{LT} + Q_R*T)/V_I$. As another consequence of the limit, it should also be noted that while the conventional interpretation of M is that a value of 0 indicates no exchange and a value of 1 indicates complete exchange, this interpretation must be modified for our model, or for any closed volume where $V_I > (V_{LT} + Q_R*T)$. As we have seen, when $V_I > (V_{LT} + Q_R*T)$, the volume of water exchanged is limited to $(V_{LT} + Q_R*T)$ and the limit to M is $(V_{LT} + Q_R*T)/V_I$. Thus, "complete" exchange in this case would not be 1, but rather the limit value of $(V_{LT} + Q_R*T)/V_I$. As a final note on using M to estimate residence time in small volume systems, when V_I is on the scale of or greater than V_{LT}, our choice of $V_{estuary}$ in the residence time calculation becomes important, because of the larger difference between mean, high tide, and low tide volume. $V_{estuary}$ is conventionally defined as the mean estuary volume, but in small-volume systems, we can consider the estuarine storage volume to be the sum of the low tide storage V_{LT} and the volume of water in the tidal prism which is not "new" ocean water V_{NO}, and is thus ambient estuarine water yet to be flushed. V_{NO} can be calculated from tidal prism V_I using the tidal exchange ratio R, so we can define the flushing volume of the estuary used for calculating residence time in small-volume systems as $V_{estuary} = V_{LT} + (1-R)*V_I$.

In addition to the differences in the interpretation of M that must be considered for small-volume systems, it is also important to consider the potential effects on mixing that large

differences between V_I and V_{LT} might have in such systems, and the subsequent consequences for estimating M using the flux bin method. In the previous section, we defined the volumes V_{AE} and V_{AI} which undergo tidal exchange processes within an estuary during the high tide phase of a tidal cycle between flood and ebb, and using these defined volumes, we found that the relationship between V_{NE} and V_{AI} was dependent on nature of the tidal exchange processes between V_{AE} and V_{AI}, so that for direct replacement only $V_{NE} = V_{OA} \approx V_{AI}$, and for complete mixing of V_{AE} and V_{AI}, $V_{NE} = V_{OA}*C_{OA} \approx V_{AI}*C_M$, where $C_M = V_{AE}/(V_{AE} + V_{AI})$. In larger systems ($V_{estuary} >> V_I$), "direct replacement" (i.e., estuarine water is directly expelled from an estuary on an ebb tide without first mixing with oceanic water from the previous flood) may be as or more important than "direct mixing" (i.e. estuarine water first mixes with incoming oceanic flood water before exiting on the subsequent ebb) in tidal flushing, so that the approximation $V_{NE} \approx V_{AI}$ is valid. This approximation is an inherent assumption in the flux bin method, where V_{NE} is estimated using the "net" inflow volume of water in oceanic scalar classes, V_{net}. This "net" volume V_{net} is used in the calculation to estimate V_{NE}, but from its method of calculation we can see it is actually a measure of V_{AI}, because it is directly measuring the net difference in incoming oceanic flood water, which is either a) mixed into estuarine scalar classes before exiting the estuary on the following ebb tide, or b) retained within the estuary. In other words, in the flux bin method V_{net} measures the net "loss" of flood water at oceanic scalar classes to estuarine mixing and replacement V_{AI}, rather than directly measuring flushing of ambient estuarine water V_{NE}, thus using the assumption $V_{NE} \approx V_{AI}$.

If we include the effects of significant "direct mixing" in tidal exchange, we find that the relationship between V_{NE} and V_{AI} deviates from the approximation $V_{NE} \approx V_{AI}$ used to estimate V_{NE} (and thus $M = V_{NE}/V_I$) in the flux bin method, and in fact the estimate of V_{NE} from V_{AI} is inflated by some factor $f = V_{AI}/V_{NE}$. From $V_{NE} = V_{OA}*C_{OA}$ and the approximation $V_{OA} \approx V_{AI}$, we see that $f \approx (C_{OA})^{-1}$ (valid for all combinations of direct mixing and direct replacement), where $f \approx 1$ (no inflation) for direct replacement only and $f \approx (C_M)^{-1} = (V_{AE} + V_{AI})/V_{AE}$ for complete mixing of V_{AE} and V_{AI}. For large systems, if the volumes of water which mix are relatively unconstrained by boundaries, it is reasonable to assume that any mixing which is present occurs "symmetrically" between nearly equal volumes of water, such that the mixing proportion (ratio of estuarine water to total mixed volume) is roughly 0.5; using this value $C_M \approx 0.5$ for the case of complete, equal-volume mixing of V_{AE} and V_{AI}, we obtain an inflation factor $f \approx 2$, which represents the maximum value of the inflation factor which occurs when there is only direct mixing (of equal volumes V_{AE} and V_{AI}) and no direct replacement. When some combination of direct replacement ($C_{OA} \approx 1$) and direct mixing ($C_{OA} \approx 0.5$) of V_{AE} and V_{AI} occurs, $f \approx (C_{OA})^{-1}$ is some intermediate value between 1 and 2. In larger estuaries, this inflation by $f = V_{AI}/V_{NE}$ of the estimate of V_{NE} from V_{AI} (and thus the estimate of $M = V_{NE}/V_I$) may not be particularly significant, and in fact often this inflation may be offset by underestimation of V_{AI} in the flux bin method (V_{net} is used to estimate $V_{NE} \approx V_{AI}$ to calculate M, where V_{net} is actually a lower-bound measure of V_{AI}). In small-volume systems such as small perimeter sloughs (including PAB), we can hypothesize that relatively large tidal prism relative to system volume ($V_I > V_{estuary}$) could

create conditions of strong tidal mixing, increasing the importance of direct mixing over direct replacement in tidal exchange and thus increasing the inflation factor relative to large estuaries. In cases of very strong tidally forcing small-volume systems where $V_I >> V_{LT}$, V_{AE} and V_{AI} may approach their respective limits of V_{LT} and V_I, such that $V_{AI} > V_{AE}$, and complete mixing of these volumes would result in "asymmetric" mixing of oceanic and estuarine volumes of water. If we consider the complete mixing case for asymmetric mixing where $V_{AI} > V_{AE}$, we see the inflation factor $f \approx (C_M)^{-1} = (V_{AE} + V_{AI})/V_{AE}$ under these conditions can be even greater than 2 (the value for complete symmetric mixing where $V_{AI} = V_{AE}$). In short, the results of analyzing tidal exchange by considering both direct mixing and direct replacement as tidal exchange processes between the oceanic incoming tidal prism and ambient estuarine water show that strong mixing conditions due to strong tidal forcing in small-volume systems can affect the estimation of the tidal exchange ratio M by increasing $f = V_{AI}/V_{NE}$ and thus inflating the estimate of V_{NE} using V_{net} in the flux bin method (which assumes $V_{NE} \approx V_{AI}$). Keeping this in mind is important when interpreting of the results obtained from estimating M using the flux bin method, especially when analyzing tidal exchange in small-volume systems with strong tidal forcing such as PAB.

2.6.3 Estimates of M from Numerical Modeling Results

Now that we have considered how to interpret the estimates of M in our system, we can discuss the specific results obtained from the numerical model by applying the flux bin method. From the numerical modeling results, it appears that in all cases where the tidal forcing is greater than 1 cm in amplitude, the flux bin method significantly overestimates the volumetric exchange ratio M as compared to the results of the mass ratio method, particularly for cases with very strong tidal forcing, which is consistent with the overestimation of M observed in the results from the field data. The inflation is most pronounced in the 1 m tidal amplitude case, where the estimate for M from the flux bin method is significantly larger than both the estimate from the mass ratio method and the ratio (V_{LT}/V_I) which is the theoretical upper limit for M when $Q_R = 0$ as in the model. As the strength of the tidal forcing decreases (i.e. for the 30 cm, 10 cm, and 1 cm tidal amplitude cases), the overestimation of M from the flux bin method as compared to direct calculation of M using the mass ratio method decreases, until for the 1 cm case the estimates from the two methods are roughly the same. This is consistent with the hypothesis that the overestimation is caused by tidal mixing associated with strong tidal forcing in small-volume systems where V_I is on the order of or larger than $V_{estuary}$ so that (V_{LT}/V_I) is small. We can also estimate the inflation factor $f = V_{AI}/V_{NE}$ by comparing the results of the estimate from the flux bin method $M \approx (\Sigma_+ V_{net}/\Sigma V_{in})$ to the direct calculation of $M = V_{NE}/V_I$ using the mass ratio method. Because V_{net} is a measure of V_{AI} (rather than V_{NE}), the estimate from the flux bin method becomes $M \approx (\Sigma_+ V_{net}/\Sigma V_{in}) \approx V_{AI}/V_I$, and we can define this result as a new ratio $M_f = V_{AI}/V_I$, so that taking the ratio of the two estimates gives an estimate of the inflation factor ($f = M_f/M = (V_{AI}/V_I)/(V_{NE}/V_I) = V_{AI}/V_{NE}$). Other than the 1 cm case where the estimates for the two methods are roughly the same ($f \approx 1$), the estimates for M from the flux bin method for the various tidal

forcing cases range from 2 to 5 times larger than the calculated M from the flux bin method, so that $f = M_f/M \approx 2\text{-}5$.

To directly observe the effects of strong tidal mixing, we can look at the case in the model results with the strongest tidal forcing, the 1 m amplitude case. From the results for this case in Table 2.2, we see that the ratio $(V_{LT}/V_I) = 0.09$, so that the tidal prism is roughly an order of magnitude larger than the low tide volume. From a plot of volumetric flux results for this case (Figure 2.7), we see that at the lowest (most "oceanic") scalar classes, nearly all of the incoming volume flux does not exit the system at the same oceanic scalar class, presumably due to the effects of strong tidal mixing, and this produces a disproportionately high net volume flux V_{net} as measured by the method, resulting in inflated value used to estimate V_{NE} and consequently an inflated estimate for M. In this case, we see that $f = V_{AI}/V_{NE} = M_f/M \approx 5$, which is an indication not only that strong "direct mixing" is present, but also that mixing of unequal volumes of water (large volumes of oceanic flood water with small volumes of estuarine water) has resulted in "asymmetric mixing" conditions so that the inflation factor $f \approx (C_M)^{-1} = (V_{AE} + V_{AI})/V_{AE}$ even is greater than $f = 2$ (the value for complete mixing of equal volumes $V_{AI} \approx V_{AE}$).

2.6.4 Observational Results from PAB

The strength of the flux bin method lies in its ability to estimate M from limited field observations at the mouth boundary of an estuarine system, since in modeling analyses M can be calculated directly (e.g. by the mass ratio method). In the previous section we have discussed possible mechanisms why the flux bin method appears to overestimate M in the numerical model results. We now use the analysis of our modeling results to help inform our discussion of our observational results and interpret the unexpectedly high estimates for M which were obtained from the application of the flux bin method to the field observations at the small perimeter slough in PAB.

The main question we will consider is whether conditions of "asymmetric" mixing discussed for the numerical modeling results are also able to explain the unexpectedly high results of estimating M from the field observations using the flux bin method. This condition was most clearly observed in the strongly forced, 1 m amplitude tide model case, where the ratio of low tide volume to tidal prism (V_{LT}/V_I) of 0.09 for the model is very low (recall that we expect the upper limit for M to be $(V_{LT} + Q_R*T)/V_I$, where $Q_R = 0$ for the model). The ratio of V_{LT}/V_I for the real site may be somewhat different than this due to differences in bathymetry, system storage, and forcing dynamics between field and model, and this difference may explain part of the difference between the field and the model results for M (about 0.35 and 0.2-0.25, respectively), along with the lack of freshwater input in the model. However, the model value for V_{LT}/V_I can be taken as representative for the system when tides are large (~ 1 m in amplitude). Using rough estimates for system volume and tidal prism ($V_{LT} \approx 4 \times 10^4$ m^3, $V_I \approx 2 \times 10^5$ m^3) from the field, we can estimate a conservative upper limit V_{LT}/V_I of about 0.2. If we include the freshwater input at the field site, the theoretical upper limit that we would expect for M is then $(V_{LT} + Q_R*T)/V_I$, which is on the order of $M \approx 0.35$ if we use an estimate for freshwater input of $Q_R \approx$

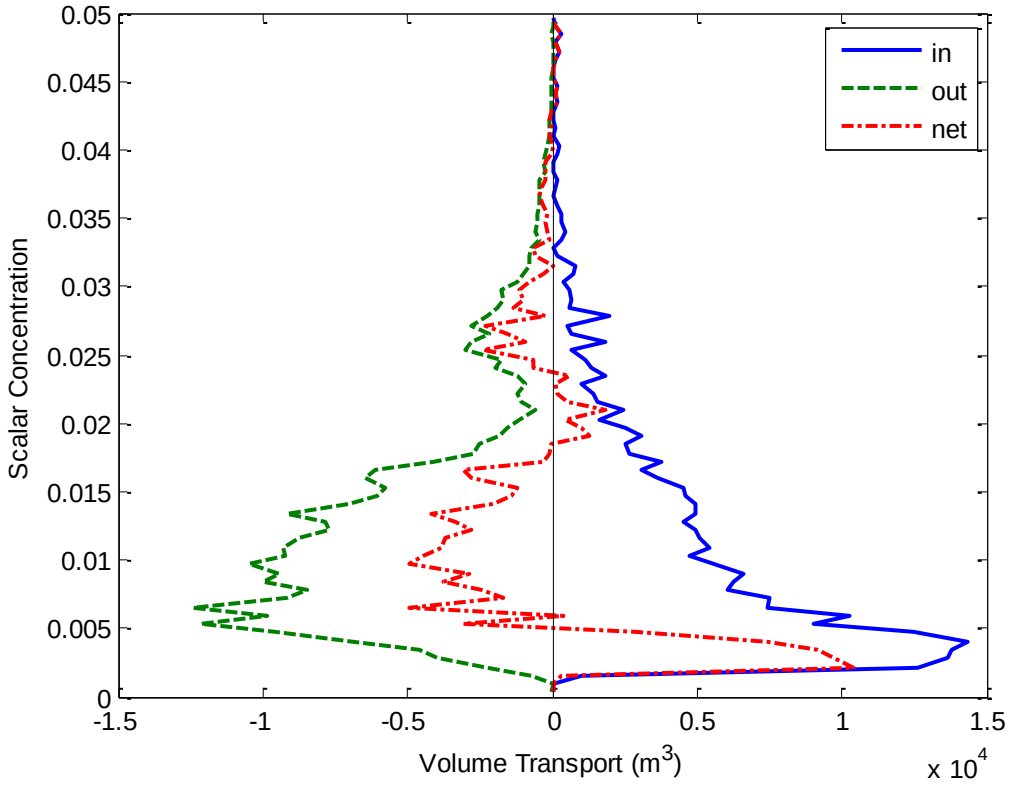

Figure 2.7: Volume flux results for the numerical model forced with 1 m tides. Results are shown for the sixth tide in the simulation.

0.7 m^3/s, or about 3×10^4 m^3 over an M2 tidal period T = 12.4 h. Since the results for estimating M from the field observations using the flux bin method were also in the range of 0.35, we see that these estimates are approximately equal to the theoretical upper limit value of 0.35 that we calculated from $(V_{LT} + Q_R*T)/V_I$. Although the calculation of this value is rough, it is still gives us a baseline with which to interpret the results for M for the field site. If the estimates of 0.35 for M at PAB obtained from the flux bin method were correct, this would mean that a volume V_{NE} approximately equal to our estimate for the entire low tide storage combined with the volume of freshwater input over a tidal period, that is $(V_{LT} + Q_R*T)$, is being mixed and replaced by tidal exchange processes over a single tidal cycle, a situation which seems physically unlikely. From these considerations we can reasonably conclude that the flux bin method is overestimating M from the field observations, as we also saw clear overestimation of M using the flux bin method for the model results. Given this, and given that conditions in the PAB field site are similar to those observed in the model, where we saw that in small-volume systems where $V_I > V_{estuary}$ strong tidal mixing can increase the estimate of M using the flux bin method by increasing $f = V_{AI}/V_{NE}$, we can infer that strong tidal mixing similar to that observed in the numerical modeling results is a probable cause of overestimation of M by the flux bin method in small-volume systems such as PAB.

Even if we allow that strong tidal mixing is inflating the estimate of volumetric exchange ratio *M* at PAB, the field results along with the numerical model results suggest that a significant fraction of the system volume is being mixed and replaced during each high tide phase of the tidal cycle, i.e. V_{NE} is a significant fraction of V_{LT}. For the 1 m case in the numerical model, the ratio of V_{NE}/V_{LT} is ~0.5, and this may be representative of the approximate value of this ratio in PAB. As mentioned above in the discussion on interpreting *M* in small-volume systems, if we want to estimate the residence time using $ERT_T = (V_{estuary}/(RMV_I))*T$, the volume of the estuary in a small-volume system can be considered to be $V_{estuary} = V_{LT} + (1-R)*V_I$. Thus although we can use *M* to estimate $V_{NE} = M*V_I$, we cannot estimate the residence time without also knowing tidal exchange ratio *R*, which was not observed in this study. If the value of *R* is large ($R \approx 1$), then $V_{estuary} \approx V_{LT}$, and if V_{NE}/V_{LT} is ~0.5, then about half of the volume of the estuary is being flushed on each tidal cycle ($Q = R*M*V_I/T = V_{NE}/T$) and the estimate for ERT_T becomes close in scale to a simple flushing process where $ERT_T = T_f = V/Q = (V_{LT}/V_{NE})*T$. Since V_{LT}/V_{NE} is small (~2), ERT_T is short, on the scale of twice the tidal period *T*. This represents an extreme, limiting case where *R* is at a maximum; conversely if $R \approx 0$ then $V_{estuary} \approx V_{LT} + V_I$, and ERT_T is very large.

2.7 Conclusions

From our findings we conclude that although the flux bin method is able to estimate and quantify mixing and exchange in estuaries as demonstrated from previous studies, there appear to be limits to the physical characteristics and conditions for hydrodynamic systems where this method can be applied, as in the case of very strong tidal forcing in small-volume systems. The usefulness of the flux bin method is in its ability to arrive at a simple estimate of the estuarine volumetric exchange ratio *M* from data collected only at the boundary of a system, and we can consider the same assumptions and approximations which make the method useful also to determine the limits on its application. Although the flux bin method can be considered robust in that it uses scalars as quasi-Lagrangian tracers to estimate ratios of volume fluxes without requiring precise magnitudes of total fluxes, the scalar flux class calculations in the method are sensitive to the nature of the tidal exchange processes within an estuary. The flux bin method inherently contains assumptions about estuarine mixing and exchange in the system, relying on the assumption of a steady tidal exchange of incoming water at oceanic scalar classes with outgoing water at estuarine classes, and particularly on the assumption that net exchange at oceanic classes can be used to estimate flushing of estuarine water through direct replacement by incoming oceanic flood water during a tidal cycle ($V_{NE} \approx V_{AI}$). We find that conditions of strong tidal mixing can introduce errors to the estimation of *M* using the flux bin method by increasing $f = V_{AI}/V_{NE}$, especially in systems such as small perimeter sloughs or other estuarine systems with very strong tidal forcing.

Even though the flux bin method appears to be overestimating *M* at PAB due to limitations caused by the characteristics of the perimeter slough system, we can consider whether the results from the method can be interpreted as measuring some other quantity that can characterize the

nature of estuarine exchange processes in the system. Since in the method V_{net} measures V_{AI} and not V_{NE}, we can reinterpret the flux bin method as calculating the value of $M_f = V_{AI}/V_I = f * M$, which represents the fraction of the tidal prism which undergoes tidal exchange through mixing and replacement processes within an estuary during a tidal cycle. Thus a value of $M_f = 0$ indicates no tidal exchange ($V_{UI} = V_I$), whereas a value of $M_f = 1$ indicates that all of the incoming tidal prism V_I is exchanged with estuarine water either through direct replacement or direct mixing ($V_{AI} = V_I$), and thus the outgoing tidal prism V_O contains no unchanged oceanic water ($V_{UI} = 0$) and consists entirely of water exiting the estuary at estuarine scalar classes ($V_{OA} = V_O$). For our field observations from PAB, the flux bin method produced estimates for M of roughly ~0.35, and if we interpret this value as estimating $M_f = V_{AI}/V_I$ rather than the volumetric exchange ratio M, this result means that about 35% of the tidal prism volume is undergoing tidal exchange with ambient estuarine waters within the slough system through mixing and replacement processes between flood and ebb during each tidal cycle.

In this study, we have used field observations and numerical modeling to examine and interpret the results of the flux bin method for estimating volumetric exchange ratio M, in order to analyze and quantify hydrodynamic exchange in a small perimeter slough. Further studies are necessary to continue to explore methods to quantify tidal mixing and exchange processes in systems such as small perimeter sloughs, where we find that previously developed methods of analyzing exchange may be unreliable or require reinterpretation due to conditions which may occur in small-volume hydrodynamic systems under strong tidal forcing. For our study, we were able to use numerical hydrodynamic modeling as a valuable tool for supplementing and aiding analysis of field observations in mixing and exchange studies. Future observational and modeling studies could help to answer questions of scalar structure and transport in small perimeter sloughs and responses of such sloughs to varying tidal, wind, and freshwater forcing dynamics, allowing us to further understand the nature of mixing and exchange process in these systems.

Chapter 3: Analyzing Tidal Transport in an Estuary Using Lagrangian Coherent Structures[2]

3.1 Introduction

The dynamics of many estuaries are dominated by tidally forced flows which interact with estuarine bathymetry and topography, and these interactions are particularly important to transport near the estuarine perimeter. On time scales shorter than the tidal period, tidal forcing in estuaries produces periodic flood and ebb currents, which for macrotidal estuaries have velocities generally many times greater than steady velocities produced from barotropic freshwater input forcing or salinity-induced density-driven exchange. On time scales longer than the tidal period, residual tidal velocities produce a net tidal transport which contributes to overall estuarine transport in a system. Because of the spatially and temporally complex nature of tidal transport, there are multiple approaches to analyzing tidal transport. These can be generally categorized as Eulerian approaches, which analyze quantities which are fixed in space, or Lagrangian approaches, which analyze quantities using a framework which follows the transport of mass in a system.

Eulerian analyses can be useful for quantifying total transport (i.e., advective and dispersive fluxes) in estuaries, for example using spatial and temporal averaging and decomposition (e.g. Fischer 1972, 1976). In order to understand the mechanisms of time- and space-varying tidal transport processes in estuaries, however, Lagrangian analyses using approaches such as particle-tracking can be more appropriate, because they follow the complex motions of specific masses of water. While Eulerian averages can be well-suited to describing and analyzing relatively uniform estuarine flows such as vertical and lateral exchange, the superposition of a relatively uniform tidal oscillatory flow with a highly non-uniform residual velocity field can result in the introduction of "Lagrangian chaos" into the tidal advection field (Zimmerman 1986), where small perturbations in initial location can have significant effects on particle trajectories. Various scaling comparisons, for example ratios of the length scales of tidal excursion to residual eddies or the ratio of residual and tidal velocity amplitudes, can be used to attempt to quantify the dispersive effects of chaotic advection regimes (Zimmerman 1976). Although these scaling comparisons are useful as a theoretical approach to analyzing Lagrangian dispersion due to the interaction of tides and idealized eddies, in real estuaries residual eddies may be present at multiple length and velocity scales, making application of analytical scaling for Lagrangian tidal dispersion difficult (Zimmerman 1986).

[2] Submitted to Journal of Geophysical Research - Oceans.

Recently, the effects of Lagrangian chaos on dispersive transport in hydrodynamic flows have been successfully analyzed using concepts from dynamical systems theory (Ridderinkhof and Zimmerman 1992, Beerens et al. 1994, Wiggins 2005). One method which has found application for analyzing Lagrangian transport in a wide variety of fluid flows is the identification of Lagrangian coherent structures (LCS) (e.g. Shadden et al. 2005, Peng and Dabiri 2009). For time-dependent systems, LCS can be defined as ridges in spatial fields of the finite-time Lyapunov exponent (FTLE), which is a measure of the linearized growth rate of a small perturbation in the initial particle position, calculated over a finite time for a given flow (either forward or backward in time). LCS are thus useful as tools for identifying flow structures which influence dispersive transport in complex and chaotic flows. Previous studies have shown the viability of analyzing coastal ocean flows using LCS (e.g. Shadden et al. 2009), with some studies of LCS in tidal flows in estuaries as well (Branicki and Malek-Madani 2010, Huhn 2012).

To analyze Lagrangian estuarine tidal transport, we will use FTLE and LCS to analyze hydrodynamic modeling and particle-tracking results for a numerical estuarine model representing South San Francisco Bay. This site was chosen because it is a well-studied macrotidal estuary where study of tidal interactions with the estuarine perimeter is motivated by ecological and environmental restoration considerations. The objectives of this study are to use Lagrangian methods to analyze, quantify, and compare the effects of Lagrangian tidal transport mechanisms in the model estuary, in particular interactions between tides and perimeter estuarine topography. In Section 3.2, the numerical modeling and particle-tracking used in the study as well as the Lagrangian analysis methods used to calculate FTLE fields and locate LCS are described. In Section 3.3, the results of using the numerical model and particle-tracking to calculate FTLE for various time scales are presented. In Section 3.4, the mechanisms of Lagrangian transport for various particle subregions in specific areas of focus for two release cases are examined. In Section 3.5, the significance and implications of the LCS results for analysis of tidal transport in estuaries are analyzed and discussed.

3.2 Methods

3.2.1 Numerical Modeling and Particle Tracking

The SUNTANS hydrodynamic numerical model (Fringer et al. 2006, Wang et al. 2009) was used to analyze tidal transport in a model domain representing South San Francisco Bay, which is a macrotidal estuary with a narrow, deep channel (up to about 15 m in depth) and broad, shallow shoals (about 1-4 m in depth). The tides in the South Bay are nearly standing, partially progressive waves. The tides are amplified in the landward direction along the axis of the estuary, with a mean tidal range of 1.5 m near the "mouth" of the South Bay which increases to about 2 m at the Dumbarton Narrows near the southeastern (landward) end of the bay (Walters 1982).

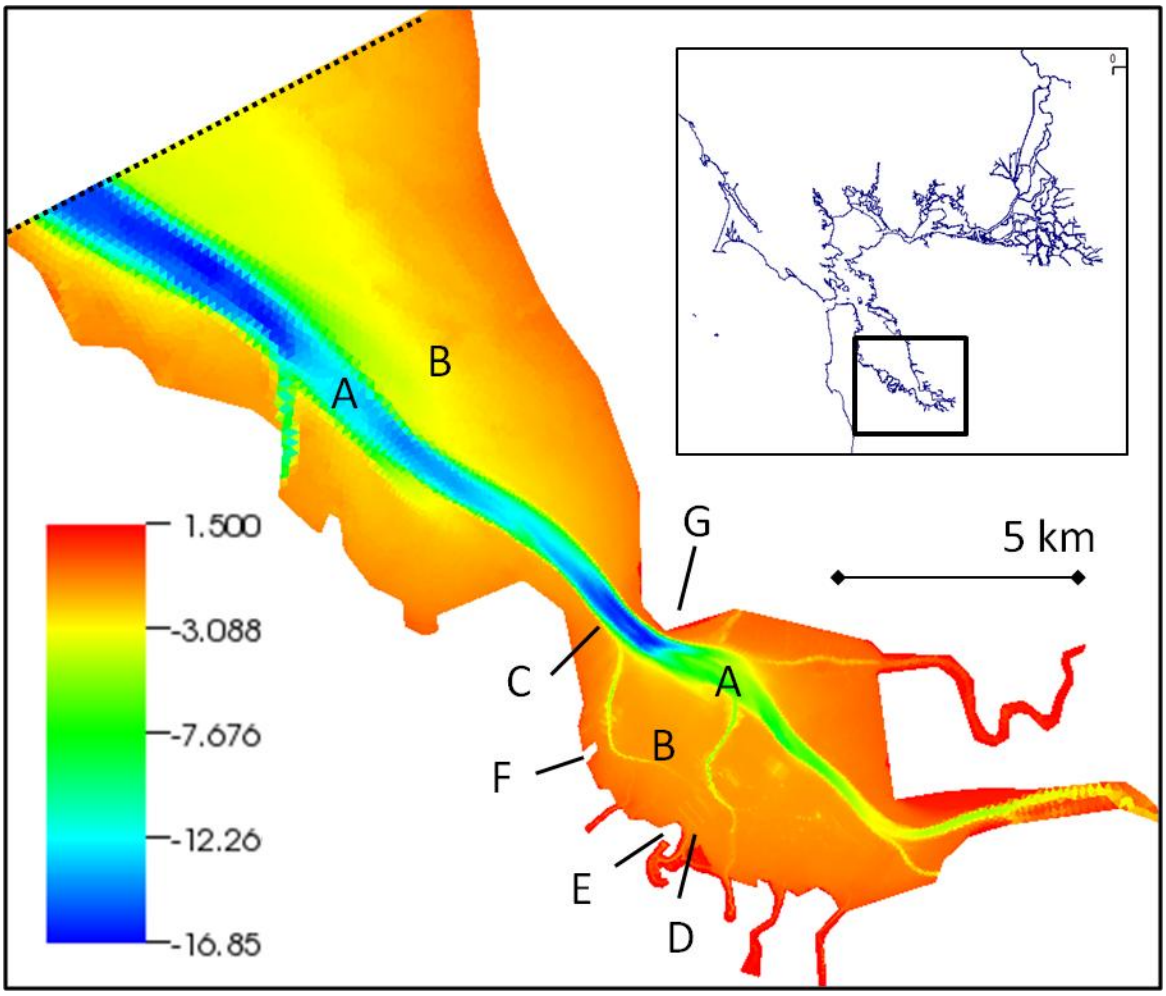

Figure 3.1: Map of grid bathymetry used in SUNTANS model of South San Francisco Bay, with colorbar showing elevation in meters. Inset shows location of model domain within San Francisco Bay. Black dotted line at northwest boundary of domain shows location of open, tidally forced boundary (roughly collocated with the San Mateo Bridge). Letters label locations of important features: A) main channel, B) shallow shoals, C) Dumbarton Narrows, D) Palo Alto Baylands (PAB) slough, E) Sand Point, F) Cooley Landing, G) Dumbarton Point.

The SUNTANS model used an unstructured grid based on shoreline and bathymetry data from San Francisco Bay (Figure 3.1). An open boundary was used at the northwest end of the model, collocated with the San Mateo Bridge, where tidal forcing was applied using idealized periodic harmonic tides (12 hour period, 75 cm amplitude). Our focus in this study is on the region south of the Dumbarton Narrows, which we will refer to as the Far South Bay, and forcing the model at the San Mateo Bridge provided sufficient separation between the boundary and the domain of interest. The horizontal resolution varied from 200 m at the open boundary to about 35 m in the Far South Bay, and vertical spacing used z-levels ranging from 0.5 m resolution at the surface to about 1.5 m resolution in the deepest parts of the channel. To focus on the effects of tidal transport on estuarine dispersion, the hydrodynamics were forced using

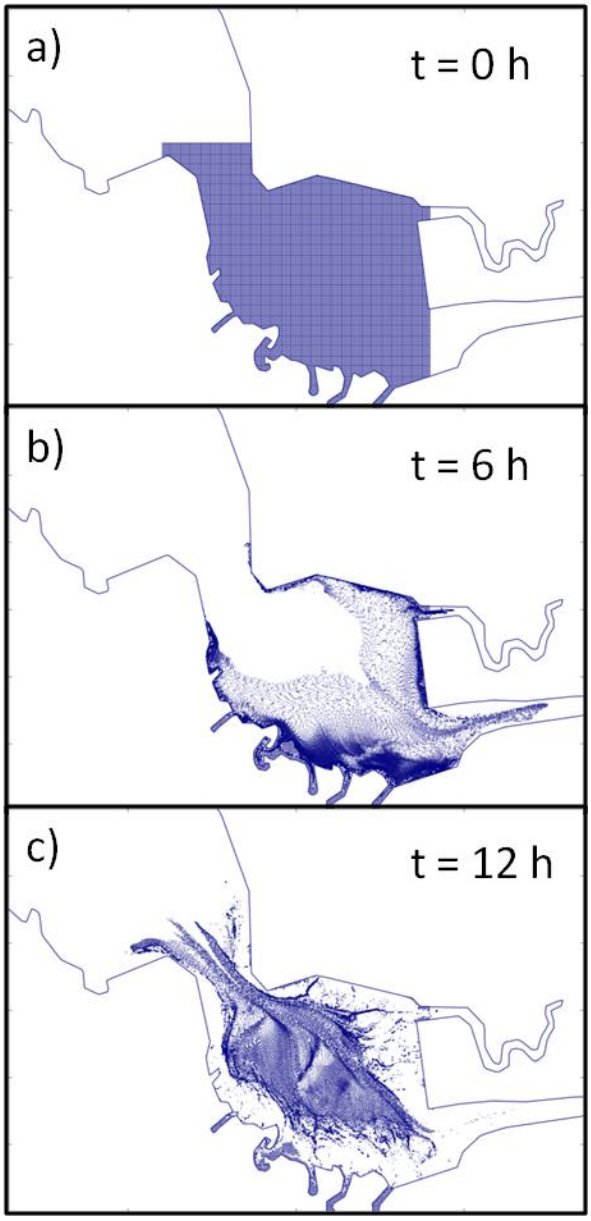

Figure 3.2: Particle locations from particle tracking model at 6 hour intervals over 12 hour integration time period (one full tidal cycle) with initial particle release t_0 at low tide. Particles positions are advanced using depth-averaged velocities. Subpanels: a) t = 0 hours (initial release locations at low tide), b) t = 6 hours (high tide), c) t = 12 hours (final particle locations at low tide).

only the tidal boundary condition, and other physical forcings such as wind, freshwater input, and density dynamics were not included in the model. The effects on tidal transport of wind forcing was also tested for certain cases, but these results will be explored elsewhere.

A particle-tracking model was used to obtain particle trajectories from the depth-averaged tidal velocity fields obtained from the hydrodynamic model (Figure 3.2). In the model, particle

positions were advanced using simple, deterministic advection during each time step, using 15 min resolution velocities from the hydrodynamic data. In this study, we focus on tidally-driven dispersion and therefore use of the depth-averaged velocities from full 3-dimensional tidal hydrodynamic runs is appropriate for particle advection. The dispersive effects of vertical shear will be considered in the discussion using analytic solutions and scaling to quantify the contribution of density effects. The particles were initialized in a 8 km x 8 km rectangular grid with 25 m horizontal spacing in the far South Bay. This area was chosen as a focus of this study because it contains features typical of many estuaries, such as channel-shoal bathymetry as well as significant interaction between tidal flows and complex perimeter topography, including various intertidal sloughs.

3.2.2 Locating LCS using FTLE

To analyze tidal transport, Lagrangian coherent structures (LCS) were located by calculating the finite-time Lyapunov exponent (FTLE) field. FTLE is a finite-time average measure of the particle separation rate in a flow, and thus LCS were located by identifying ridges in the FTLE field, which represent local maxima of separation rate (Shadden et al. 2005, Peng and Dabiri 2009). From the Eulerian flow field $\boldsymbol{u}(t,\boldsymbol{x})$, particle trajectories were used to obtain a Lagrangian particle flow map $\varphi_{t_0}^{t_0+T}(\boldsymbol{x})$, which maps particles with initial position $\boldsymbol{x}$ at time t_0 to their final positions after a time interval T (this particle flow map is dependent on both t_0 and T). For a slightly perturbed particle with initial position $\boldsymbol{y} = \boldsymbol{x} + \delta\boldsymbol{x}(0)$, a linearized approximation for perturbation growth gives the maximum magnitude of the perturbation after a time interval T as

$$\|\delta\boldsymbol{x}(T)\| = \lambda_{max}(\boldsymbol{\Delta})\|\delta\boldsymbol{x}(0)\|. \tag{3.1}$$

Here, the symmetric matrix

$$\boldsymbol{\Delta} = \frac{\mathrm{d}\varphi_{t_0}^{t_0+T}(\boldsymbol{x})}{\mathrm{d}\boldsymbol{x}}^{*} \cdot \frac{\mathrm{d}\varphi_{t_0}^{t_0+T}(\boldsymbol{x})}{\mathrm{d}\boldsymbol{x}} \tag{3.2}$$

is a finite-time version of the right Cauchy-Green deformation tensor (the '$\cdot$' operator indicates the inner vector product and the superscript '*' denotes the transpose of a tensor), and $\lambda_{max}(\boldsymbol{\Delta})$ is the square root of the maximum eigenvalue of $\boldsymbol{\Delta}$ (particle separation is largest when the initial perturbation is aligned with the eigenvector associated with $\lambda_{max}(\boldsymbol{\Delta})$). The FTLE, representing the maximum growth rate of a small perturbation at location $\boldsymbol{x}$ and time t_0 over a time period T, is defined as

$$\sigma_{t_0}^{t_0+T}(\boldsymbol{x}) = \frac{1}{|T|}\ln\left\|\frac{\delta\boldsymbol{x}(T)}{\delta\boldsymbol{x}(0)}\right\| = \frac{1}{|T|}\ln\lambda_{max}(\boldsymbol{\Delta}). \tag{3.3}$$

Using this definition, the FTLE can thus be interpreted as a finite-time, linearized measure of Lagrangian particle dispersion. The LCS, identifying "coherent structures" which influence transport in the flow, can then be defined as ridge lines in the FTLE field, where a ridge line is a

curve normal to which the topography of the field is a local maximum (Shadden et al. 2005). For the purposes of our analysis, visual inspection of FTLE fields was sufficient to identify LCS ridge lines, although more precise definitions of ridge lines can also be used. In addition, this definition can be used either with forward-time integration to locate repelling LCS (stable manifolds for time-independent hyperbolic trajectories) or with backward-time integration to locate attracting LCS (unstable manifolds for time-independent hyperbolic trajectories). In this study, we are primarily interested in Lagrangian dispersion mechanisms in tidal transport, and thus we only use forward-time FTLE to locate LCS.

As the notation indicates, the FTLE field $\sigma_{t_0}^{t_0+T}(\boldsymbol{x})$ (often abbreviated as $\sigma(\boldsymbol{x})$ for simplicity) can be dependent on both the initial time t_0 and the integration time T. This is especially important when calculating FTLE fields for time-dependent and/or periodic flows, such as for flows found in tidal systems. Thus the FTLE field in a tidal system will depend on the phase of the tide at initial time t_0, as well as the integration time T which may range from small to large as compared to the tidal period. Because we are interested in the effects on tidal transport processes from interaction of tidal flows with perimeter topography, we will focus our analysis on the effects of interaction of tidal transport with perimeter topography over a full tidal cycle. The tides in the South Bay are close to standing waves, so that low tide (low water) and slack water nearly coincide for all locations, and particles released with t_0 at low tide for T equal to the simulation tidal period of 12 h experience a full tidal cycle consisting of a flood tide followed by an ebb tide. Thus particles released at low tide are advected first towards and then away from perimeter features; the reverse is true for high tide releases, and we will use both to calculate FTLE fields to measure the effects on Lagrangian particle transport of tidal interactions with the perimeter.

To identify mechanisms of separation in time-varying tidal flows, we also calculated FTLE at shorter time scales. FTLE was calculated for integration time T = 6 h starting from low tide ,to analyze transport mechanisms over the flood tide only. In addition, FTLE fields were calculated with T = 1 h from particles initialized at mid-flood and mid-ebb during the tidal cycle in order to analyze transport mechanisms over time scales much shorter than the tidal period. Finally, FTLE fields were also calculated for time periods longer than 12 h, which would represent cumulative transport over multiple tidal cycles. However, analysis and discussion of these long time-scale results is beyond the scope of this study and will be reserved for future studies.

3.3 Results

3.3.1 Short Time-Scale Particle Separation Mechanisms

Although we are interested in total tidal transport, which requires analysis of dispersion over the full tidal cycle , it is instructive to first examine FTLE fields calculated for shorter time scales in order to identify mechanisms of short-term particle separation in the time-varying tidal flow. Figures 3.3 and 3.4 show the FTLE field in the far South Bay calculated using a 1-hour time interval, starting at mid-flood and mid-ebb respectively.

In the mid-flood FTLE field (Fig. 3.3), several flow separation mechanisms can be identified by locating LCS (ridges in the FTLE field). First, two LCS ridges can be clearly seen on either

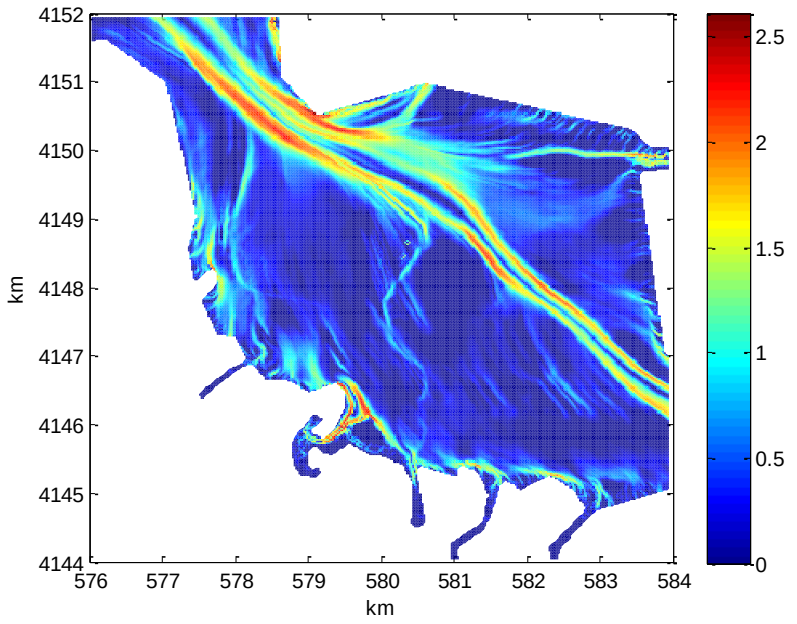

Figure 3.3: FTLE field (h^{-1}) for initial particle release t_0 at mid-flood with integration time period T = 1 hour. Horizontal and vertical axes show coordinates in kilometers.

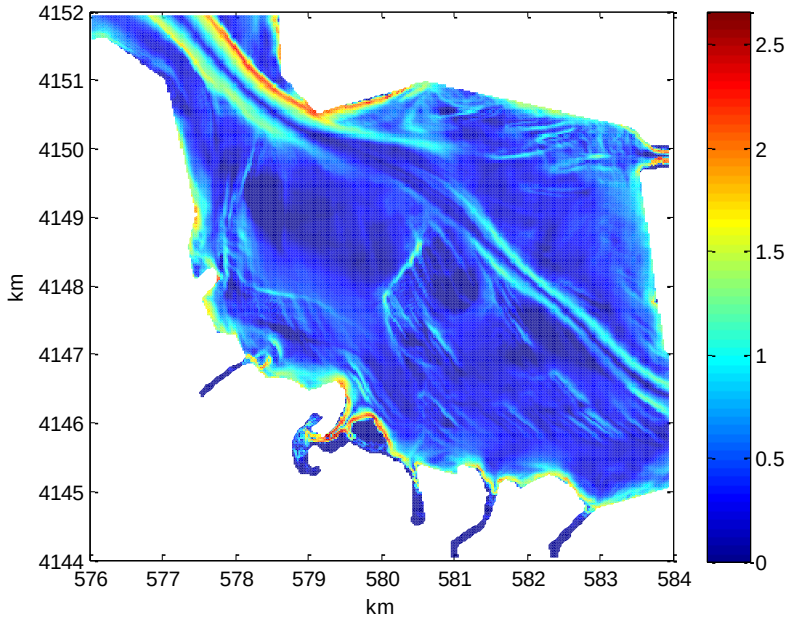

Figure 3.4: FTLE field (h^{-1}) for initial particle release t_0 at mid-ebb with integration time period T = 1 hour. Horizontal and vertical axes show coordinates in kilometers.

side of the main channel along the axis of the estuary. These arise as a consequence of the strong lateral velocity shear that develops on the slopes between channel and shoal, which result in differential longitudinal advection along the axis of the estuary with greater flood velocities in the deeper channel than in the shallow, friction-dominated shoals. Second, LCS can be identified near the mouths of the sloughs, with an especially prominent LCS ridge at the entrance to the large slough complex at the Palo Alto Baylands (D in Fig. 3.1), as well as near headlands, with a short LCS ridge visible near the small peninsula at Cooley Landing (F in Fig. 3.1). These FTLE ridges can be interpreted as repelling LCS associated with particle pathline divergence near hyperbolic trajectories attached to boundaries, where the length of the ridge is defined by the distance over which particles are advected to the hyperbolic point during the integration time *T* (Huhn et al. 2012). Finally, smaller FTLE ridges collocated with minor bathymetric channels are evidence of pathline divergence associated with these features during flood tide.

In the mid-ebb FTLE field (Figure 3.4), the LCS ridgelines along either side of the main channel are still present, but not as prominent as in the mid-flood FTLE. This can be explained by the asymmetry between the mid-flood and mid-ebb flows: during the ebb, flow is generally converging towards the main channel, resulting in lower FTLE. Similarly, the LCS associated with pathline divergence at slough mouths and headlands do not appear in the mid-ebb FTLE, because the ebb pathlines near these features are likely to be converging (rather than diverging as on the flood), resulting in low FTLE. The most prominent LCS during the mid-ebb, attached to Dumbarton point and extending northwest alongside the eastern slope of the main channel, occurs due to the conjunction of the flow separation at the headland and the influence of the lateral shear from the channel. Regions of high FTLE can also be observed in the Palo Alto Baylands slough due to particle separation from bathymetry-induced shear.

3.3.2 Tidal Time-Scale Particle Separations

From the short time-scale FTLE fields, we are able to identify mechanisms of short-term particle trajectory separation. These short-term mechanisms will allow us to interpret LCS identified from longer-term FTLE fields calculated using time scales of interest to tidal transport, namely those related to the tidal period. For a complete analysis of tidal transport, we must consider transport over the full tidal cycle, which for our simulation consists of a 12-hour sinusoidal tidal harmonic starting at low water which can be divided into a flood tide phase followed by an ebb tide phase (approximately 6 hours each). The final separation used to calculate FTLE results from the cumulative integration over time of the Lagrangian separation from the flow, and thus interpretation of the FTLE for long time scales requires knowledge of the Lagrangian separation mechanisms over the entire integration time. To analyze tidal flow, we calculated FTLE fields in the far South Bay for three cases, one case analyzing transport over the 6-hour flood period, and two cases analyzing transport over the full 12-hour tidal cycle (one case initialized at low tide, and another case initialized at high tide).

For the 6-hour FTLE field calculated over the flood period from low to high tide (Figure 3.5), we see some features similar to the 1-hour FTLE field calculated at peak flood, although the 6-

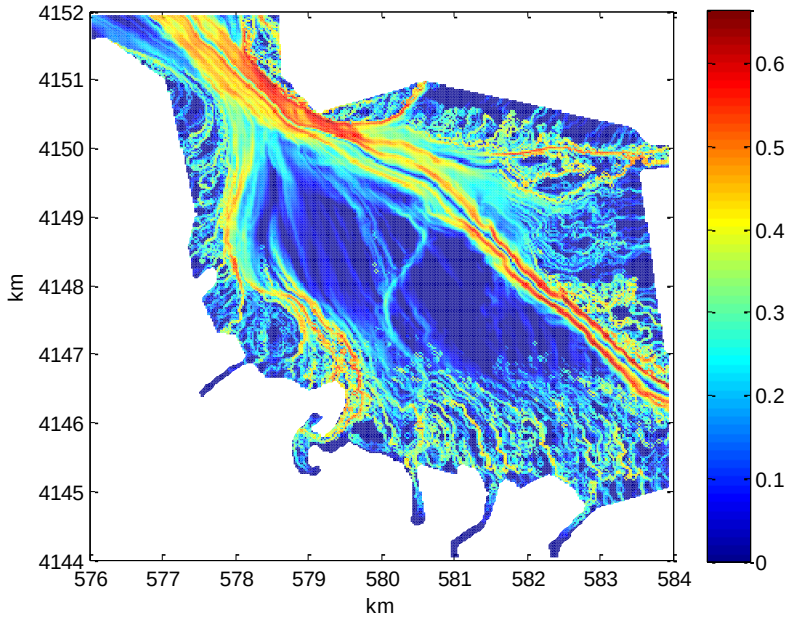

Figure 3.5: FTLE field (h^{-1}) for initial particle release t_0 at low tide with integration time period T = 6 hours, corresponding to flood tide.

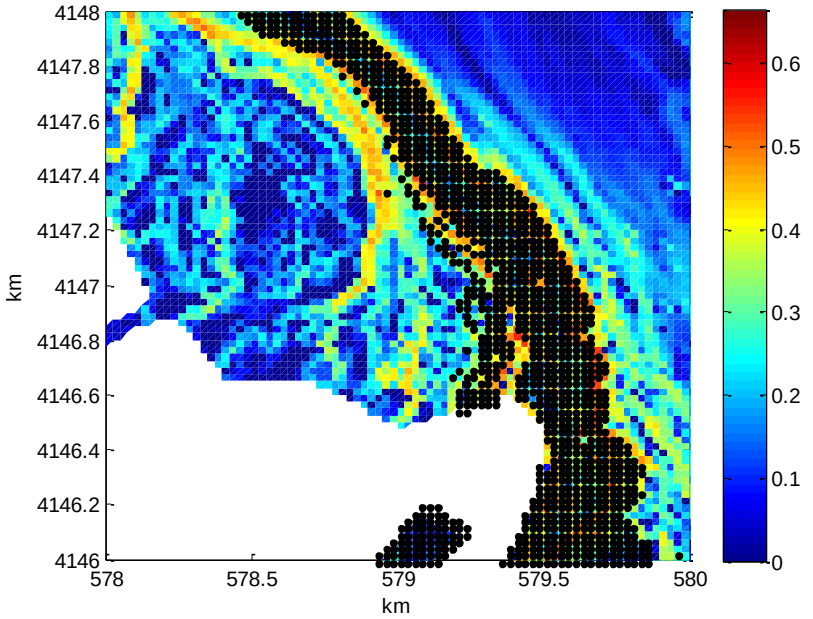

Figure 3.6: Close-up of FTLE field (h^{-1}) at mouth entrance to PAB slough for low tide particle release with integration time period T = 6 hours (see Fig. 3.5). Black dots show initial release locations of particles which have entered into the PAB slough after 6 hours.

hour FTLE is seen to have considerably more complexity than the 1-hour FTLE. In the 6-hour flood FTLE, prominent LCS indentified by FLTE ridges collocated with the slopes of main channel are present as in the 1-hour peak flood FTLE, and in the constriction at the Dumbarton Narrows, we see a large region of high FTLE. The LCS associated with flood pathline divergence caused by headlands and minor bathymetric channels that were observed in the 1-hour FTLE are also observed here (Fig. 3.5), to varying degrees of prominence. The perimeter of the estuary is characterized by striated patterns of high FTLE that have a complexity mirroring the perimeter topography. This band represents areas where particle trajectories experience interactions with the perimeter topography during the flood tide period, which affects perturbation growth (of initial perturbation at t_0 at these locations). In particular, LCS can be used to identify the subregion of flood water which enters the slough complex at the Palo Alto Baylands, where FTLE ridgelines identify LCS on either side of the region of water entering the slough on the flood tide (Figure 3.6).

The 12-hour FTLE field, initialized at low tide and calculated over the entire flood-ebb tidal cycle (Figure 3.7), is even more complex than the 6-hour flood FTLE field. Here several of the LCS observed in the 6-hour FTLE, including the LCS associated with the edges of the main channel and the LCS associated with pathline divergence in the minor channels, are not as prominent in the 12-hour FTLE as compared to the 6-hour FTLE. This is because the particle separation that occurs during the flood can be reversed on the following ebb, which for a perfectly reversible, symmetric flood-ebb cycle would result in zero net growth in particle separation for an initial perturbation. Because of the presence of tidal asymmetries, however, these mechanisms still produce LCS with elevated FTLE for the 12-hour period, though of somewhat lower magnitude than in the 6-hour FTLE. A particularly prominent feature in the 12-hour FTLE is the band of high, complex FTLE around the perimeter of the far South Bay where the tidal flow interacts directly with the perimeter topography over the full flood-ebb tidal cycle. This region is evidence that the tidal flood-ebb cycle produces flows which interact with perimeter topography in complex ways, producing Lagrangian flow separation mechanisms and elevated FTLE. There are also several areas of banded longitudinal (along-axis) LCS, such as in the Dumbarton Narrows and the perimeter area near the Palo Alto Baylands, which will be discussed further below.

The previous two examples both had an initial time t_0 during the same tidal phase (low tide), with different integration time period T (6 hours and 12 hours). For results with a different initial tidal phase, we can examine the FTLE field where the initial time t_0 of particle release is at high tide. The high-tide release FTLE results for a 6-hour integration time (over the ebb tide) are similar to the mid-ebb FTLE results (Fig. 3.4) and are thus not shown here, but the high-tide FTLE with a 12-hour integration time, shown in Figure 3.8, is significantly different than any of the previous results. In contrast with the flood releases, the most obvious feature of the high tide 12-hour FTLE is a region of ripple-like banded LCS near the perimeter of the Far South Bay,

which will be discussed further on. Thus we have seen that the results of LCS analysis using tidal time-scale FTLE depends significantly on both the integration time period (half or full tidal

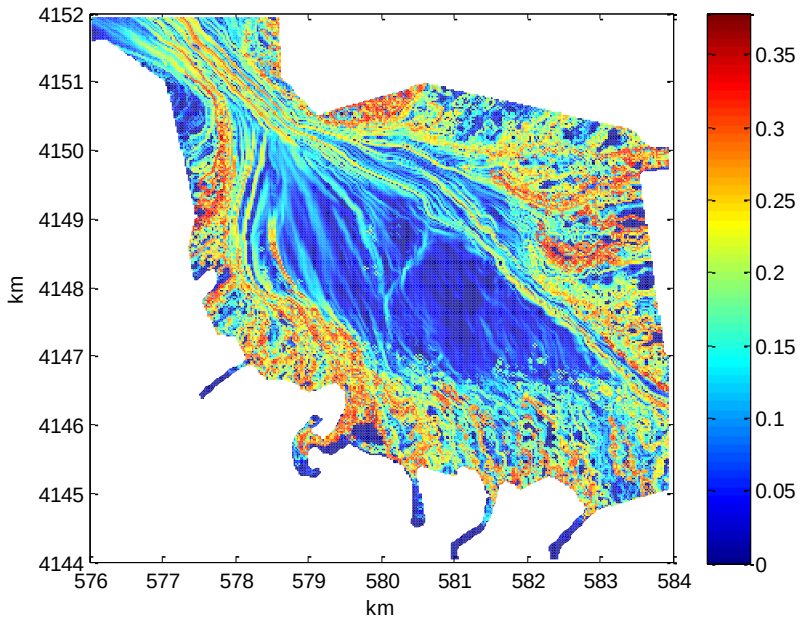

Figure 3.7: FTLE field (h^{-1}) for initial particle release t_0 at low tide with integration time period T = 12 hours, corresponding to full flood-ebb tidal cycle.

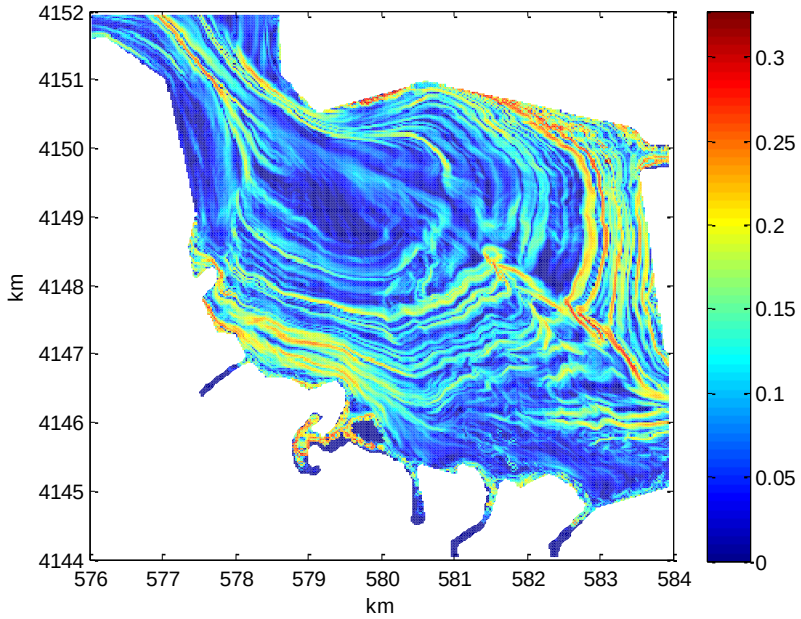

Figure 3.8: FTLE field (h^{-1}) for initial particle release t_0 at high tide with integration time period T = 12 hours, corresponding to full ebb-flood tidal cycle.

cycle) as well as the choice of initial time t_0 (low tide or high tide). To gain a more complete understanding of these results, in the next section we will examine specific mechanisms of particle mechanisms for each FTLE case.

3.4 Mechanistic Analysis of Lagrangian Particle Separation

This section will focus on the mechanistic analysis of the particle separation results for the FTLE field calculated for the full 12-hour tidal cycle, in order to analyze total tidal transport in the system. From the 12-hour FTLE field calculated from the full flood-ebb tidal cycle, we are able to identify complex LCS that represent the cumulative, time-integrated effects of particle separation mechanisms occurring over shorter time scales within the 12-hour period. Our goal now is to be able to interpret the LCS identified from the FTLE as the result of specific mechanisms tied to tidal transport processes which lead to the final particle separations. To do this, we will focus on two areas within the Far South Bay where we will more closely examine the LCS identified from the 12-hour FTLE, the first area from the low-tide release case, and the second area from the high-tide release case. For each of these two areas of focus, we divide the domain into particle subsets, where we flag particles at the start of the tidal time period (at low water) based on their positions relative to LCS ridgelines evident in the 12-hour FTLE. Once we have defined these Lagrangian subregions, we can then use the particle tracking model to analyze the Lagrangian behavior of each subregion (i.e., the Lagrangian advection of the particles in each subregion as a group) in order to identify the mechanisms causing high final particle separation between each subregion over the 12-hour tidal cycle (as is evidenced by the LCS defined by high FTLE).

The first area of focus is the area near the Dumbarton Narrows for the case of initial particle release at low water, where we find multiple LCS ridgelines aligned with the direction of tidal flow in the 12-hour FTLE field (Fig. 3.7). Using these LCS ridgelines, we can define seven approximate Lagrangian subregions, by taking regions between ridgelines as regions of relatively coherent Lagrangian transport. By defining subregions this way, we label seven subregions as A through G (Figure 3.9a), and observe the behavior of each subregion over the full flood-ebb tidal cycle using particle tracking.

Figures 3.9b-f show the location of the particles within each Lagrangian subregion at 3-hour intervals, which allows us to analyze the development over time of the displacement of each subregion due to tidal transport. The particle locations for each subregion at 6 hours, approximately at high water, is particularly illustrative of the separation which occurs between each Lagrangian subregion as a result of the tidal transport, as each region is transported to a different location after the flood tide (Fig 3.9d). At high water, subregion A is mostly trapped along the perimeter boundary by the flood tide. Subregion B, C, and D are relatively unconstrained by the perimeter boundary at high water, with C located in the main channel and experiencing larger displacement along the axis of the estuary than B or D due to the differential advection caused by lateral shear between the deep channel (C) and the friction-dominated shoals (B and D). From observing the locations of regions D through G at high water, we see

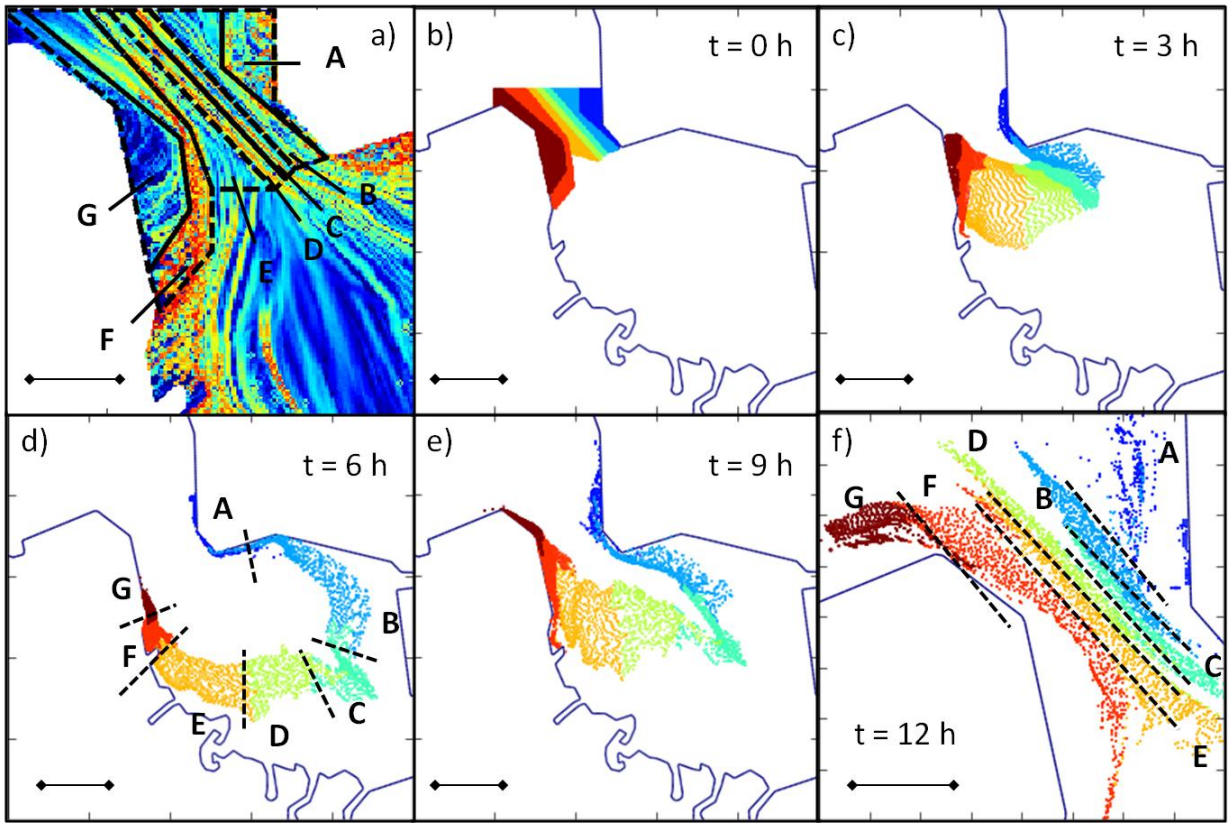

Figure 3.9: LCS subregion analysis for the Dumbarton Narrows area, for initial particle release t_0 at low tide with integration time period T = 12 hours. Subpanel a) shows subregion definitions (A-G) using approximate LCS ridgelines, and subpanels b) through f) show particle subregion trajectory locations at 3 hour intervals over the full 12-hour flood-ebb tidal cycle. Scale bars with a length of 1 kilometer are shown for each subpanel, and black dotted lines show approximate divisions between subregions.

that each subregion is progressively more affected by the interaction of the incoming flood tide with the southwestern perimeter boundary, and the separation between these subregions can be seen as originating from local topographical features along this boundary. For example, the separation between D and E occurs as a result of Sand Point west of the Palo Alto Baylands (PAB), and subregions E and F are similarly divided by the peninsula at Cooley Landing, northwest of PAB. The division between subregions F and G is less distinct, but occurs due to the smaller promontory north of Cooley Landing, and regions of high FTLE within subregion F are likely due to particle separation resulting from more complex, smaller-scale interactions between the tidal flow and the perimeter boundary for particles originating at these locations. The differences in Lagrangian displacement for each subregion at 6 hours represents transport over only half of the total 12-hour time period. Over the second 6-hour period, the ebb tide returns each Lagrangian subregion to a location close to its initial starting position, but with a final displacement which represents the cumulative effects of Lagrangian transport of each subregion over the total 12-hour integration time (Fig. 3.9f).

The fact that these subregions are separated by LCS indicates that the growth rate of particle separation is greater at the boundaries of these regions than within them. In other words, the boundaries of the regions are the most dispersive. The fact that several of these LCS are associated with particles that interact with particular bathymetric features on the perimeter illustrates the complexity of estuarine dispersion and the importance of the detailed tidal trajectories of water parcels as they move from the channel to the estuaries perimeter.

We would like to validate the identification of these Lagrangian subregions using LCS, which we have done in part by observing similarities in Lagrangian trajectories between subregions and differences between subregions, but which we can also do by using the observed final location of each subregion after the full 12-hour tidal cycle (Fig. 3.9f). The relative final displacement of each Lagrangian subregion is significant because it is differences in final displacement between adjacent subregions that produce the high FTLE used to identify LCS ridgelines and define the Lagrangian subregions. From the particle tracking observations, we can directly observe the difference in final Lagrangian displacement between adjacent subregions. We observe general similarities in Lagrangian trajectories and final displacement within subregions (and differences in trajectories and displacement between subregions) which are sufficient to confirm the validity of defining Lagrangian subregions based on identifying LCS ridgelines from the FTLE field.

For our second area of focus, we will analyze the area near the eastern boundary of the Far South Bay for the case of initial particle position at high tide. The high-tide 12-hour FTLE is characterized by banded LCS ridges parallel to the perimeter boundary, and in this area we define four approximate Lagrangian subregions, labeled A-D (Figure 3.10a), and observe their behavior, this time over a full ebb-flood tidal cycle (instead of flood-ebb as in the previous two cases). In Figures 3.10b-f we see that the Lagrangian subregions from this area become strained in the longitudinal direction as they are drawn into the main channel during the ebb tide, and at 6 hours (approximately at low water) they each occupy a different longitudinal section of the channel (Fig 3.10d). Over the subsequent flood tide, the subregions are then are pushed back towards their initial position during the flood tide.

From the final position of the high-tide perimeter Lagrangian subregions, we see that subregions A and C are transported relatively northward, and subregions B and D are transported relatively southward at the end of the ebb-flood tidal cycle (Fig. 3.10f). The relative north-south displacement clearly occurs as the subregions are "unstrained" over the flood tide, from 6-12 hours, and it is likely that relatively northward or southward subregion displacement is a function of residual circulation and is influenced by the position of the subregion at low water (6 hours) relative to the main channel and the perimeter (Fig. 3.10d). For example, at 6 hours subregion C is located very close to Dumbarton Point at low water and would feel the largest influence of the boundary, while subregion A is located on the bend of the main channel (see Fig. 3.1 for bathymetry), resulting in relative northward displacement for both subregions. Subregion D is also the only subregion that is advected past Dumbarton Point over the ebb tide, and is

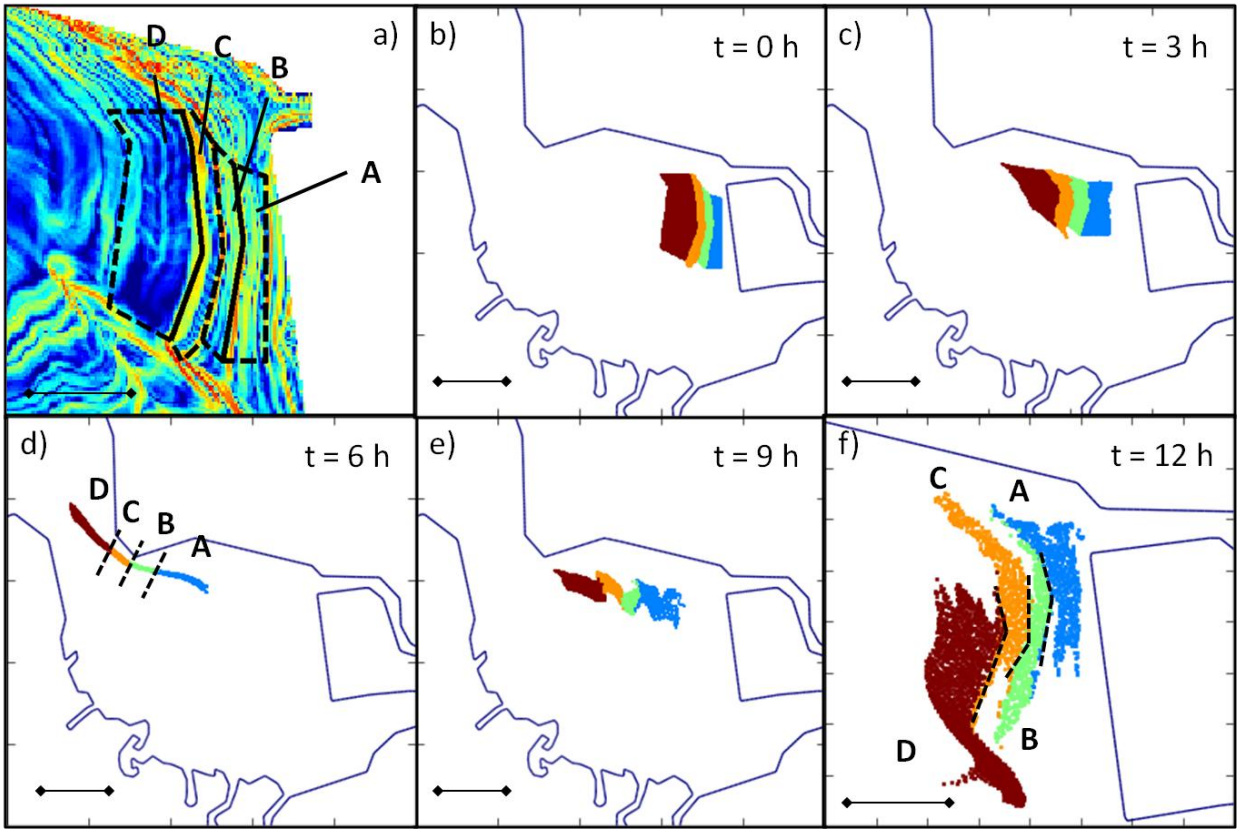

Figure 3.10: LCS subregion analysis for the area near the eastern boundary of the Far South Bay, for initial particle release t_0 at high tide with integration time period T = 12 hours. Subpanel a) shows subregion definitions (A-D) using approximate LCS ridgelines, and subpanels b) through f) show particle subregion trajectory locations at 3 hour intervals over the full 12-hour ebb-flood tidal cycle. Scale bars with a length of 1 kilometer are shown for each subpanel, and black dotted lines show approximate divisions between subregions.

subsequently the only subregion with net southward displacement (subregions A-C have net northward displacement).

3.5 Discussion

3.5.1 Dependence of Lagrangian Tidal Transport in Estuaries on Site-Specific Features

The particle-tracking analysis of the LCS-defined Lagrangian subregions in the previous section demonstrates that Lagrangian tidal transport is the cumulative result of interactions of Lagrangian flow trajectories with Eulerian tidal velocity fields, similar to the "Lagrangian chaos" used by Zimmerman (1986) to model tidal dispersion by superposing a mean oscillating tidal current over residual currents of various scales. For a given subinterval of time within the total integration time interval, each subregion is advected as a whole by the Eulerian tidal current, but due to differences in location each subregion samples a different region of the Eulerian velocity field, and as a result each subregion experiences a local displacement which is different from its

neighbors. At smaller scales, particles within each Lagrangian subregion experience similar trajectories as a result of being in generally the same Eulerian region over the same subinterval of time, resulting in low Lagrangian separation (measured by the FTLE) within each Lagrangian subregion. At larger scales, each Lagrangian subregion becomes separated from adjacent subregions, which in turn creates further opportunities for Lagrangian separation of subregions to create differences in final Lagrangian displacement. The result of the cumulative interactions of Lagrangian subregion trajectories with Eulerian tidal velocities over a tidal period is areas of high Lagrangian deformation between adjacent subregions, resulting in the LCS ridgelines in the 12-hout tidal FTLE which we use to define the Lagrangian subregions.

Our analysis of tidal transport in the Far South Bay using particle-tracking and LCS shows that Lagrangian tidal transport can be highly complex when considering the interaction of tidal flows with estuarine bathymetry and topography. Differences in transport between Lagrangian subregions were observed to result from multiple mechanisms for Lagrangian separation, including lateral shears induced by bathymetric features and Lagrangian separation associated with topographic features such as headlands and perimeter sloughs. An important implication of these results is that tidal transport for a given estuary may depend on highly site-specific Lagrangian interactions of tidal flows with local bathymetry and topography.

Much of previous research on estuarine transport has relied on generalized models for tidal transport, which model tidal transport by using simple parameterizations of estuarine geometry, e.g. using idealized lateral bathymetry profiles which are relatively uniform in the direction of the axis of the estuary. Generalized tidal transport models may be appropriate for analyzing tidal transport processes related to relatively simple estuarine features which can be easily parameterized, such as tidal residual circulation in estuaries with channel-shoal bathymetry (e.g. Li and O'Donnell 1997, 2005), and perimeter dispersion processes may also be characterized in an Eulerian framework using tidal trapping models, when parameters such as trap exchange rates and phases are known (Okubo 1973, MacVean and Stacey 2011). However, the results of our analysis show that the effects on Lagrangian tidal transport of perimeter interactions may depend on the geometry of individual perimeter features as well as the relative positions of other nearby features, suggesting that Lagrangian tidal transport, especially for perimeter tidal transport processes, can be highly site-specific. Thus the parameterization of Lagrangian tidal transport for arbitrary estuarine topographies using generalized transport models may be difficult, due to the wide variety and range of perimeter topographic features and configurations in estuarine geometries. Given this, a more effective approach to analyzing tidal transport processes involving tidal interaction with perimeter topography may instead be to use real estuarine flow geometries rather than generalized models or idealized geometries to model estuaries, and to develop numerical modeling methods such as the particle-tracking modeling which we have used to perform Lagrangian analysis of tidal transport in this study.

3.5.2 Comparison of Tidal Perimeter Interactions to Other Estuarine Dispersion Mechanisms

In order to quantify the overall importance of perimeter interactions to estuarine transport, we can measure the effects of these processes on particle subregion displacement and dispersion and compare them to other known estuarine transport processes. For particle subregion displacement, from the particle tracking results for the Lagrangian subregions in the Dumbarton Narrows (Fig. 3.9) we see that the overall relative displacement of the adjacent subregions over a tidal cycle (on the order of 500-1000 m) is roughly the same for both the tidal perimeter interactions and the channel-shoal particle separation processes. This shows that Lagrangian transport resulting from interaction of tidal flow with site-specific perimeter topographical features can be roughly the same scale as more conventionally analyzed tidal transport processes, i.e. channel-shoal tidal residual circulation.

To quantify the effects of the Lagrangian deformation processes identified from the LCS analysis on particle subregion dispersion, we can calculate the particle dispersion coefficient K from the 12-hour particle tracking results for each subregion for both low-tide and high-tide release cases. In each case, we calculate the dispersion coefficient within each subregion (A-G for the low-tide subregions in Fig. 3.9, and A-D for the high-tide subregions in Fig. 3.10). In order to evaluate the relative dispersive effects of subregion boundaries, as compared to within subregion dispersion, we then calculate the average of these single-subregion coefficients to define K_{single} and compare that with dispersion coefficients calculated for combined pairs of adjacent subregions, i.e. dispersion coefficients are calculated for the combination of subregions A and B, combination of B and C, etc. These coefficients are averaged to obtain a mean dispersion coefficient K_{pair} for a combined pairs of subregions which includes the effect on particle dispersion of the LCS ridge which separates adjacent subregions. Finally, we also calculate the total dispersion coefficient K_{all} for the combination of all subregions for both low-tide and high-tide release cases.

The results of the particle dispersion coefficient calculations are shown in Table 3.1. For both the low-tide and the high-tide release cases, K_{pair} is larger than K_{single} by approximately a factor of two, and likewise K_{all} is larger than K_{pair} by another factor of two. The increase in particle dispersion coefficient as more subregions are included in the calculation is to some extent expected, as including a larger region will incorporate larger dispersive mechanisms. By comparing K_{pair} to K_{all}, we can see the single subregions identified by taking regions between LCS ridges have significantly lower dispersion coefficients than subregion pairs, which include LCS ridges. This is consistent with the interpretation of FTLE as a measure of Lagrangian dispersion and the use of LCS in this study to identify regions of low dispersion and coherent Lagrangian transport. Similarly, K_{all} is larger than K_{pair} because multiple LCS ridges are included when the dispersion coeffeicient is calculated for all subregions combined for each case.

Finally, we can compare the values of K to dispersion coefficients for other known estuarine dispersion mechanisms which are not measured by our horizontal particle tracking study, e.g. vertical shear dispersion. Using an estimate for the vertical shear dispersion coefficient of K_s =

Table 3.1: Dispersion Coefficient Estimates[a]

		K_{single} (m^2/s)	K_{pair} (m^2/s)	K_{all} (m^2/s)
Low-tide release subregions		2.4	5.1	10.2
High-tide release subregions		0.7	1.4	3.5

[a]Averaged values for each case (low-tide and high-tide); K_{single} calculated for single subregions, K_{pair} calculated for combined paris of subregions, and K_{all} calculated for all subregions combined

$5.93u^*d$ (Elder 1959, Fischer 1979), with estimates for the Far South Bay of depth d = 15 m and shear velocity u^* = 0.06 m/s for the deeper channel, and d = 1.5 m and u^* = 0.03 m/s for the shallow shoals, we obtain estimates for shear dispersion coefficient of K_s = 5.3 m^2/s for the channel and K_s = 0.27 m^2/s for the shoals. Because the particles in the Far South Bay spend much of the tidal cycle in the very shallow shoals, the time-integrated vertical shear dispersion coefficient K_s is probably closer to the value for the shoals and thus relatively smaller than might be expected. By comparing these values of shear dispersion coefficient K_s to Table 3.1, we see that K_s can be assumed to be on the same order or smaller than K_{pair} for the low-tide release regions in the Dumbarton Narrows and even smaller than K_{single} for the high tide release regions near the eastern perimeter of the Far South Bay. This demonstrates that the effects of Lagrangian dispersion produced by tidal interaction with topography can be at least as significant as the effects of vertical shear dispersion, and likely even more significant in very shallow areas near the perimeter of shoal-channel estuaries.

3.5.3 Dynamical Systems Interpretation of Lagrangian Tidal Transport

In studies using LCS to analyze coastal ocean flows, LCS are often used to identify transport barriers, because the behavior of an LCS is close to that of a material line, so that flux across an LCS is small or negligible (Shadden et al. 2005). In addition, LCS ridges of FTLE can often be identified in flows near Lagrangian finite-time hyperbolic (i.e., saddle-point) trajectories, where fluid material is drawn towards the hyperbolic point in the "stable" direction, and it is pushed away from the hyperbolic point in the "unstable" direction. In this study, we do not attempt to analyze flow using the dynamical systems approach of identifying hyperbolic trajectories, for example using intersections of ridges of forward and backward FTLE maps, as this approach requires long-lived and well-preserved flow features and thus may be difficult to apply to tidal estuarine transport processes (Branicki and Malek-Madani 2010). However, it is interesting to interpret our results using some of the concepts borrowed from the framework of dynamical systems transport analysis, such as hyperbolic trajectories and "lobe dynamics".

From the particle-tracking results for the Lagrangian subregions for each of the three areas of focus, it is evident that the subregions are strained by the interaction of the tidal flow with the estuarine topography, becoming strained and unstrained in various directions on different phases of the tide. In each of these cases, we see the original Lagrangian subregions become strained in

one direction during the first phase of the tide as they are transported by the tidal flow, then unstrained (that is, strained in the opposite direction) on the subsequent phase of the tide as they are transported back towards their original locations (Figs. 3.9 and 3.10). The net result from differences in residual currents caused by local topography on the Lagrangian transport of the subregions over the tidal period is that adjacent subregions become displaced relative to each other, in an alternating pattern in the direction of straining experienced during the second tidal phase (i.e., subregions are strained and displaced in the longitudinal direction on the ebbing tide for the low tide release cases in Figs. 3.9 and 3.10 and in the lateral direction on the flooding tide for the high tide release case in Fig. 3.10). Effectively, initially subregions are strained and transported during the first tidal phase; these strained, translated subregions are subjected to relatively small perturbations due to residual currents and local topography; and finally these perturbation are amplified by straining in the opposite direction during the second tidal phase, resulting in the relatively large final displacements observed. This straining in multiple directions is characteristic of the behavior of flow in the vicinity of Lagrangian hyperbolic or "saddle" trajectories, and the behavior of the Lagrangian subregions can be interpreted using the dynamical systems framework of "lobe dynamics" for a hyperbolic trajectory under weak time dependence, where regions of fluid, called lobes, become squeezed and stretched as they feel the saddle-point influence of flow as they leave or approach hyperbolic trajectories, so that fluid lobes become transported laterally, alternatingly and in the direction of strain (Wiggins 2005). The areas of focus in this study were chosen because they had well-defined LCS ridges, and we can now interpret the dynamics which produce the subregion displacements (and thus the LCS ridges) as due to the influence of the interaction of estuarine boundaries with the tidal flow, where variations in flow geometry tend to produce straining, hyperbolic flows and lobe-like Lagrangian transport. Thus the conceptual framework of hyperbolic trajectories and lobe dynamics from dynamical systems analysis provides a mechanistic explanation of how the influence of local topography on Lagrangian tidal transport can be amplified by the interaction of tidal dynamics with estuarine flow geometry.

3.6 Conclusions

In this study, we have applied a Lagrangian approach to analyze transport in a flow produced by tidal forcing using tools and frameworks borrowed from dynamical systems analysis, namely FTLE and LCS. These tools have allowed us to gain greater insight into the mechanisms which play an important role in tidal transport, particularly the interaction of tidal flow with estuarine perimeter topography. Using FTLE and LCS, we find that we can define Lagrangian subregions which characterize transport over a tidal period, both in net Lagrangian advection measured by tidal residual displacement, and in Lagrangian dispersion measured by the FTLE.

The analysis of Lagrangian tidal transport in this study has necessarily been location-specific, focusing on individual areas and often individual features of the modeled tidal system. Further, we have chosen to focus on the dispersive effects of the barotropic tidal flows, but the results show that the dispersive effects of tidal interactions with the perimeter are comparable or greater

than other processes commonly invoked to explain estuarine dispersion. Although the current study does not necessarily provide a general formulation of dispersion, it does demonstrate that a particle-based Lagrangian analysis is likely to be necessary to comprehensively capture estuarine dispersion processes. Lagrangian methods such as those used in this study have been demonstrated to be an effective approach to analyzing complex, chaotic flows, and they can be applied to flows from numerical models or large scale field observation such as surface LIDAR measurements; indeed the interest in applying dynamical systems frameworks such as LCS to oceanographic flows has come about largely in response to the increased availability of such large flow data sets (Wiggins 2005). The fact that these techniques have only recently been applied to such flows, especially for estuarine flows with complex boundaries and forcings, suggests that a greater understanding of complex oceanographic transport processes can be gained by further studies using these methods.

Chapter 4: Effects of Wind-Driven Residual Circulation on Estuarine Exchange and Connectivity

4.1 Introduction

Hydrodynamic transport near the estuarine perimeter is controlled by multiple physical forcings, including barotropic tides, density-driven baroclinic exchange flow due to longitudinal salinity gradients, and wind forcing. Because of the complexity of the physical forcings and the temporal and spatial variations in estuarine transport, studies often focus on specific aspects of estuarine transport. For example, classical estuarine studies have analyzed the balance between stratification sustained by baroclinic density exchange driven by the along-channel salinity gradient and tidal mixing, as well as associated dynamics such as tidal straining and tidal variations over spring-neap cycles (e.g. Simpson et al. 1990, Stacey et al. 2001). In comparison to estuarine density exchange and tidally forced processes, the effects of wind on estuarine transport have been relatively less well-studied, even though wind and tidal energy inputs can be comparable in estuarine environments (Zhong and Li 2006).

Like tidal forcing and salinity dynamics, wind forcing in estuaries can be variable on multiple time scales. Wind in estuaries can be relatively constant or can vary diurnally, and individual wind events can also create strong sustained forcing over periods of several days. The direction of wind forcing in estuaries is also variable, and can be aligned either along the axis of the estuary, across the axis, or in some intermediate direction. Estuarine studies of wind effects often analyze wind forcing in a single direction and determine the effects on transport and circulation (e.g. Chen et al. 2009). Studies have demonstrated that wind-driven flow in estuaries is downwind in shallow areas with return flow in deeper areas, when depth variations occur in the direction perpendicular to the wind set-up (Csanady 1973, Wong 1994). It has also been shown that variations in wind forcing can have significant effects on subtidal estuarine exchange (e.g. Wang 1979). In general, most studies of wind forcing in estuaries have focused on along-axis winds, and the effect of wind direction on estuarine transport has not been well studied.

Although previous studies of wind effects in estuaries have focused on the effects of wind on estuarine stratification and subtidal exchange flows (e.g. Wang 1979, Chen and Sanford 2009), wind forcing may also be important in shallow estuaries which may be weakly stratified or unstratified. In shallow, macrotidal estuaries such as South San Francisco Bay, the predominant effect of wind on estuarine transport is likely to result from the interaction of wind-driven residual circulation with periodic barotropic tidal currents, which creates complex, time-dependent flows similar to the Lagrangian chaos observed in tidal interactions with estuarine topography (Zimmerman 1976, 1986, Ridderinkhof and Zimmerman 1992). An understanding

of the effects of wind on estuarine dispersion such environments is therefore relevant for environmental management and restoration in estuaries and their perimeter habitats, for example for analyzing sediment transport and ecological transport of biota in wetland restoration projects in the perimeter of the San Francisco Bay-Delta.

In particular, a common goal of environmental and ecological management is to understand connectivity between regions or habitats. Connectivity is a concept which can be broadly defined as a measure of exchange or fluxes between locations or subregions in a given domain or habitat (Cowen and Sponaugle 2009). This exchange again may refer to any number of physical, chemical or biological scalars, and transport processes of these scalars often have important implications for ecological function and habitat quality. Types of connectivity analyses in estuarine environments have included studies of exchange rates of ecological scalars (nutrients and biota) in simple ecosystem process and transport modeling (e.g. Cloern 2007, Lucas et al. 2009) as well as the use of numerical hydrodynamic models to trace exchange between each subregions, for example in modeling studies of larval recruitment and retention (e.g. Cowen at al. 2006, North et al. 2008). When reduced to the case of mass transport between two bodies of water, connectivity is related to the concept of flushing or residence times over which hydrodynamic exchange occurs between environmental subregions or subhabitats (Monsen et al. 2002).

In this study, our goal is to analyze the effects of constant wind forcing in multiple directions on estuarine transport in a shallow, macrotidal estuary, by using Lagrangian analysis techniques to examine wind effects on hydrodynamic transport in a numerical model representing South San Francisco Bay. Particle-tracking methods will be used to analyze the effects of wind forcing and direction on estuarine transport over the tidal cycle, both by directly observing transport as well as by using Lagrangian coherent structures (LCS), as in the previous chapter, in order to study the effect of wind on Lagrangian flow structures. In addition, connectivity analyses will be performed to observe wind effects on exchange between subregions in South San Francisco Bay and its perimeter habitats.

4.2 Methods

The SUNTANS hydrodynamic numerical model was used to analyze the effects of wind on estuarine transport in a model domain representing South San Francisco Bay, using the same unstructured grid domain and tidal boundary conditions as described in the previous chapter (Fig. 3.1). As in the previous chapter, particle-tracking was used to obtain particle trajectories from the depth-averaged velocity fields $\boldsymbol{v}(\boldsymbol{x}, t)$ obtained from the hydrodynamic model, where the particle trajectory $\boldsymbol{x}(t)$ is a solution of $\dot{\boldsymbol{x}} = \boldsymbol{v}(\boldsymbol{x}, t)$. Although wind forcing can create differences between surface flows and bottom flows, in the very shallow environments of South San Francisco Bay these effects are less important in comparison to transport in deeper estuaries. Because we are interested mainly in total horizontal transport, depth-averaged velocities were used in order to analyze 2-D particle dispersion representing depth-integrated exchange. The particles were deterministically advanced using velocities from the

hydrodynamic model. Stochastic horizontal diffusion in the particle tracking model was generally small compared to the dispersion resulting from the horizontal advection, and did not have a significant effect on the results. Thus the effect of stochastic diffusion is not included in the results presented, in order to focus analysis on the dispersive effects of large-scale horizontal advection.

The particle-tracking method used advanced particles numerically during each time step by translating the particle a distance determined by multiplying the time step by a particle velocity, which was interpolated from the hydrodynamic node velocities of the cell containing the current particle location. If the particle exited a cell within the time step, substepping was used so that the particle was advanced to the boundary of the cell in one time substep, and a new particle velocity would be calculated from the updated particle location to continue advection during the next time substep. If a solid boundary was encountered due to advection during a time step, particles would be reflected off the boundary in order to prevent particle accumulation at boundaries. Using methods described in the previous chapter, the particle tracking results were used to calculate two-dimensional finite-time Lyapunov exponent (FTLE) fields for Lagrangian coherent structure (LCS) analysis and also to analyze total depth-averaged transport. FTLE is a finite-time average measure of the particle separation rate in a flow, and thus LCS, which identify "coherent structures" which influence transport in the flow, were located by locating ridges in the FTLE field, which represent local maxima of separation rate [*Shadden et al.*, 2005; *Peng and Dabiri*, 2009].

The effect of wind on estuarine dispersion was tested using five different wind cases for the Far South Bay. The first case was the base case with only tidal forcing and no wind forcing, and the other four cases all used constant wind forcing at 10 m/s, with wind in each case directed from four different directions: northwest (NW, from downestuary towards upestuary), southeast (SE, from upestuary towards downestuary), northeast (NE, cross-estuary), and southwest (SW, cross-estuary). The wind forcing was applied uniformly in space as an upper boundary condition in the non-depth-averaged SUNTANS hydrodynamic model. The five cases were each spun up for five days, then particles were released at high tide and tracked over a single 12-hour tidal period to calculate FTLE and LCS. The particle were released at high water because in this study we are primarily interested in wind effects on exchange and connectivity between subregions of the South Bay and its perimeter. Thus high water releases are necessary to analyze the effect of wind as water is drawn away from the perimeter on the ebb and back towards the perimeter on the flood, rather than low water releases which are more useful for analyzing tidal dispersion resulting from the boundary effects of perimeter topographic features as water is pushed towards and then away from the boundary (e.g. as in the previous chapter). For each case, additional particle regions were released three locations: Ravenswood, Guadalupe Slough, and Coyote Creek (Figure 4.1). These particle release regions allowed visualization of particle transport over a single tidal cycle of particles originating at high tide in locations at the perimeter of the estuary, in areas coinciding with local marsh restoration efforts.

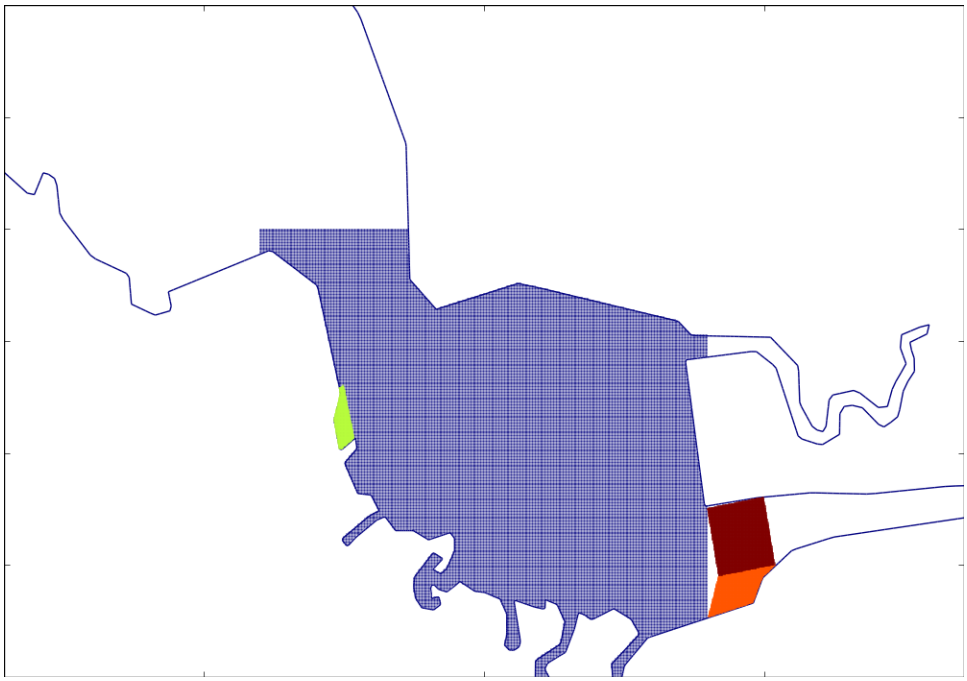

Figure 4.1: Particle releases in Far South Bay at T = 0 h. Main Far South Bay release is shown in blue, Ravenswood release is shown in green, Guadalupe Slough release is shown in orange, and Coyote Creek release is shown in red.

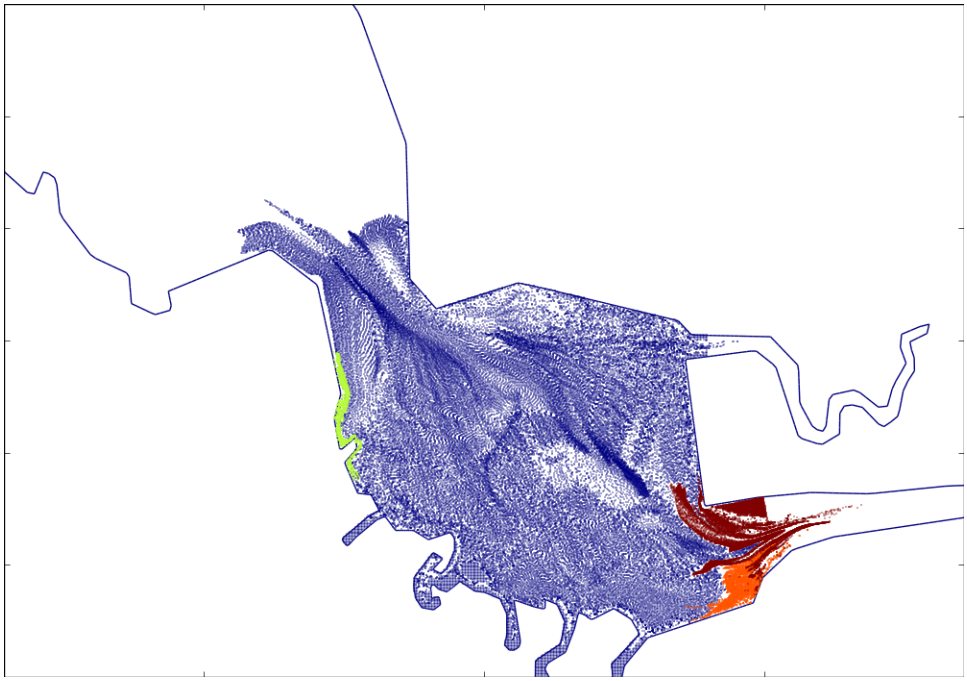

Figure 4.2: Particle releases in Far South Bay at T = 12 h for the case with no wind forcing. Main Far South Bay release is shown in blue, Ravenswood release is shown in green, Guadalupe Slough release is shown in orange, and Coyote Creek release is shown in red.

In addition, particle releases were used to analyze the effect of wind on hydrodynamic exchange and connectivity in the model domain. To do this, particles were released on a per-volume basis within an initial region, and the proportion of the initial particles which were located outside the initial region (representing the volumetric proportion of initial water which has exited the region) was determined as a function of time over a single 12-hour tidal cycle, for the case with no wind as well as for the four wind direction cases. This proportion thus represents a measure of exchange between the initial region and the rest of the domain over a tidal cycle, and a higher proportion indicates higher connectivity between regions due to the combination of tide and wind forcing. This connectivity analysis was applied to two particle release regions, the first release encompassing the entire Far South Bay and representing exchange between the Far South Bay and the main South Bay north of the Dumbarton Narrows, and the second release within the Palo Alto Baylands (Fig. 3.1) and representing exchange between a perimeter slough and the Far South Bay.

4.3 Results

4.3.1 Particle-Tracking Results

In this section, the particle-tracking results for transport of particles for each of the five cases are presented. For each case, we observed the overall residual transport of each particle release (the main particle release and the three perimeter releases) over the 12-hour tidal cycle, from high tide to high tide (Figures 4.2-4.6). In each of the figures, the final positions of the particle releases after 12 hours are shown, including the main Far South Bay particle release in blue, the Ravenswood release in green, the Guadalupe Slough release in orange, and the Coyote Creek release in red (see Fig. 4.1 for initial particle release positions, which are the same for all cases). By comparing these cases to each other, the effects of each wind direction can be analyzed. Here, the base case of no wind can be used as a benchmark for comparison. From the results in Figure 4.2 we see that without wind the residual transport of the particles is relatively small, except for some residual circulation which is upestuary (towards the southeast) in the channel and downestuary (towards the northwest) in the shoals as evidenced by the residual transport of the Coyote Creek particle release.

The results for the two along-axis wind cases are shown in Figures 4.3 and 4.4, which show results for the NW and SE wind cases, respectively. In the NW wind case, there is strong residual circulation which is downestuary in the deeper center channel and upestuary in the shallower shoals near the boundaries. Likewise, in the SE wind case, there is strong residual circulation in the opposite direction, upestuary in the center channel and downestuary near the boundaries. The transport of the individual region releases follows this general pattern of residual transport. In the NW wind case, the Ravenswood release is transported upestuary while the Coyote Creek and Guadalupe Slough releases are transported downestuary along the channel. In the SE wind case, the Ravenswood release is transported downestuary past the Dumbarton

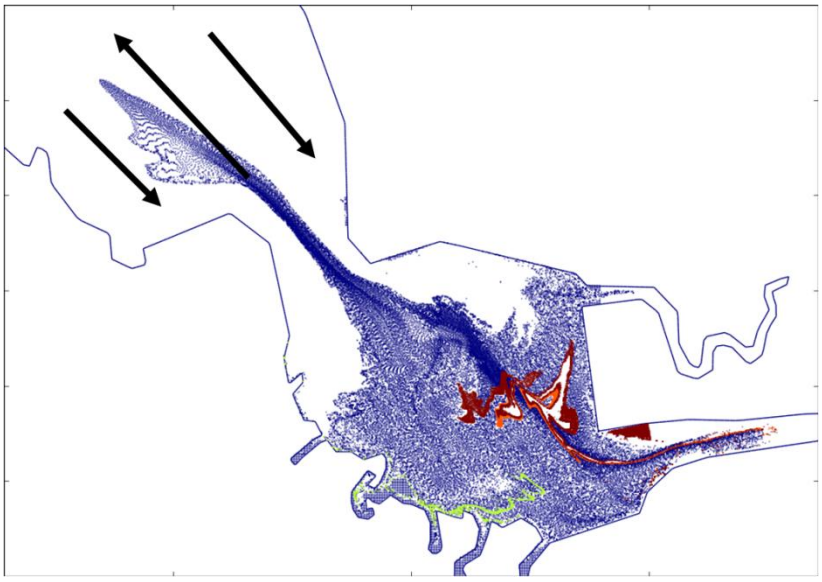

Figure 4.3: Particle releases in Far South Bay at T = 12 h for the case with wind forcing directed from the northwest (NW). Main Far South Bay release is shown in blue, Ravenswood release is shown in green, Guadalupe Slough release is shown in orange, and Coyote Creek release is shown in red. Black arrows show general direction of wind-induced residual circulation, with downwind flow in shallower areas and return flow in deeper areas.

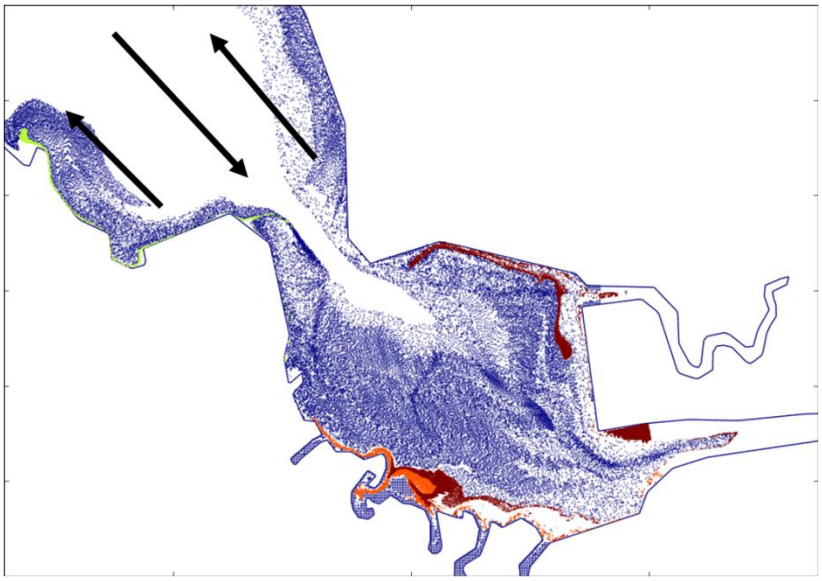

Figure 4.4: Particle releases in Far South Bay at T = 12 h for the case with wind forcing directed from the southeast (SE). Main Far South Bay release is shown in blue, Ravenswood release is shown in green, Guadalupe Slough release is shown in orange, and Coyote Creek release is shown in red. Black arrows show general direction of wind-induced residual circulation, with downwind flow in shallower areas and return flow in deeper areas.

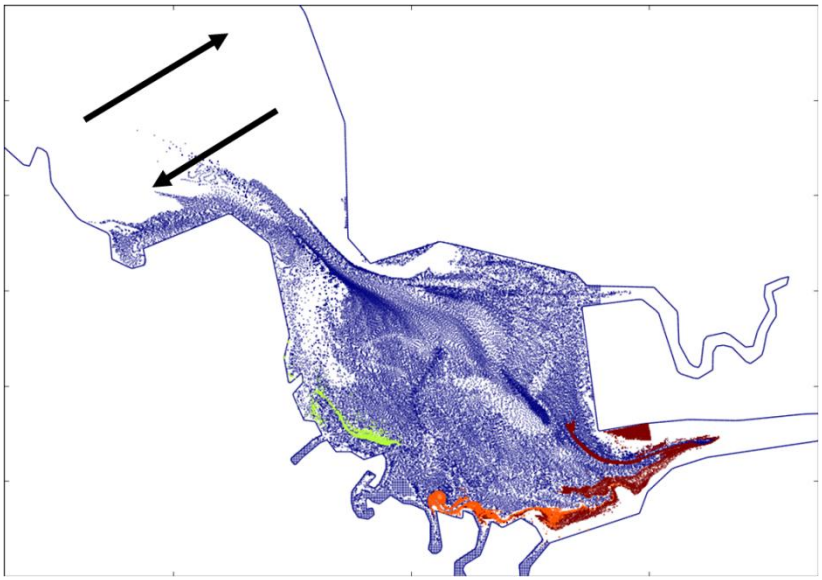

Figure 4.5: Particle releases in Far South Bay at T = 12 h for the case with wind forcing directed from the northeast (NE). Main Far South Bay release is shown in blue, Ravenswood release is shown in green, Guadalupe Slough release is shown in orange, and Coyote Creek release is shown in red. Black arrows show general direction of wind-induced residual circulation, with downwind flow in shallower areas and return flow in deeper areas.

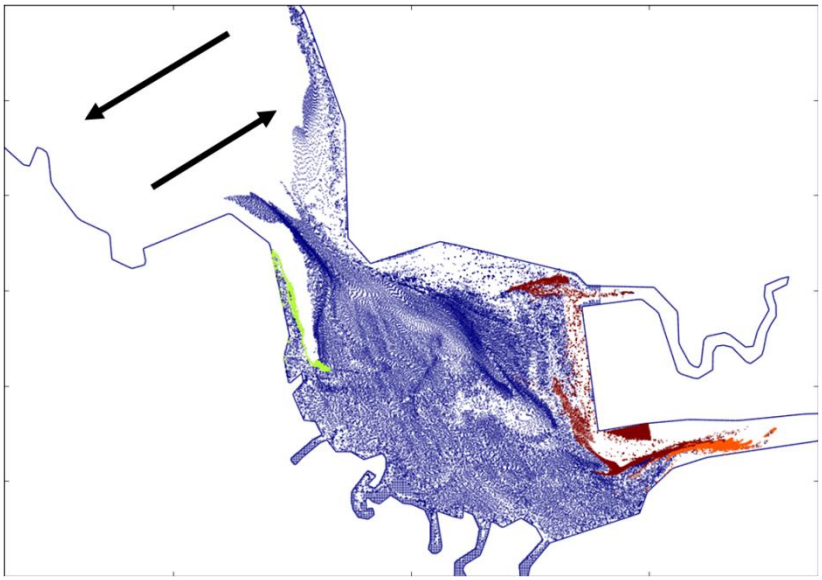

Figure 4.6: Particle releases in Far South Bay at T = 12 h for the case with wind forcing directed from the southwest (SW). Main Far South Bay release is shown in blue, Ravenswood release is shown in green, Guadalupe Slough release is shown in orange, and Coyote Creek release is shown in red. Black arrows show general direction of wind-induced residual circulation, with downwind flow in shallower areas and return flow in deeper areas.

Narrows, and the Coyote Creek and Guadalupe Slough releases are also transported downestuary along the shoals near the boundaries, with the Coyote Creek release split along the center channel and transported towards both the southwestern and northeastern boundaries

The results for the two cross-axis wind cases are shown in Figures 4.5 and 4.6, which show results for the NE and SW wind cases, respectively. In the NE wind case, the northern border of the main release shows transport at the Dumbarton Narrows which is downestuary on the western boundary of the Narrows and upestuary on the eastern boundary of the Narrows. Likewise, the SW wind case shows residual transport in the reverse direction, upestuary transport on the western boundary and downestuary transport on the eastern boundary. However, the effect of the NE and SW winds on transport of the Ravenswood release, located south of the Narrows on the western boundary, is in the opposite direction: upestuary for the NE wind case and downestuary for the SW wind case. The effect of the cross-axis winds on the Coyote Creek and Guadalupe slough releases is relative transport towards the southern boundary for the NE wind case and relative transport towards the eastern boundary for the SW wind case.

4.3.2 LCS Results

In this section, the LCS results using FTLE for each of the five cases are presented. For each case, an FTLE field was calculated, where areas of high FTLE indicate regions of high Lagrangian particle separation over the 12-hour tidal period. Again, the case of no wind is included as a base case against which the four wind cases can be compared. From the FTLE results for the no wind case (Figure 4.7), we see that the main feature present in the FTLE field for particles released at high tide with no wind is banded FTLE ridgelines near and close to parallel to the estuarine boundary. The transport mechanisms which cause these and other LCS features identified in this section were introduced and discussed in the previous chapter, and the effects of wind on these LCS features will be analyzed in the following discussion.

The FTLE results for the two along-axis wind cases are shown in Figures 4.8 and 4.9, which show results for the NW and SE wind cases, respectively. For the NW wind case, the LCS ridgelines near the boundary which appeared in the FTLE for the no wind case are also present, but the effect of the residual circulation induced by the NW wind is to rotate the orientation of these ridgelines clockwise southwest of the channel and counter-clockwise northeast of the channel. Likewise, the near-boundary LCS ridgelines are present in the FTLE field for the SE wind case, but the effect of the wind-induced residual circulation is to rotate the orientation of these ridgelines counter-clockwise southwest of the channel and clockwise northeast of the channel. In both cases, prominent LCS ridgelines appear on either side of the channel in the Dumbarton Narrows, and in the SE wind case there are ridgelines extending into the shoals and boundary on either side of the Far South Bay. In addition, for the SE wind case a prominent LCS ridgeline is present in the upestuary (southeastern) section of the main channel.

The FTLE results for the two cross-axis wind cases are shown in Figures 4.10 and 4.11, which show results for the NE and SW wind cases, respectively. For the NE wind case, the near-boundary LCS ridgelines are also present in the FTLE field, but the effect of the NE wind is to

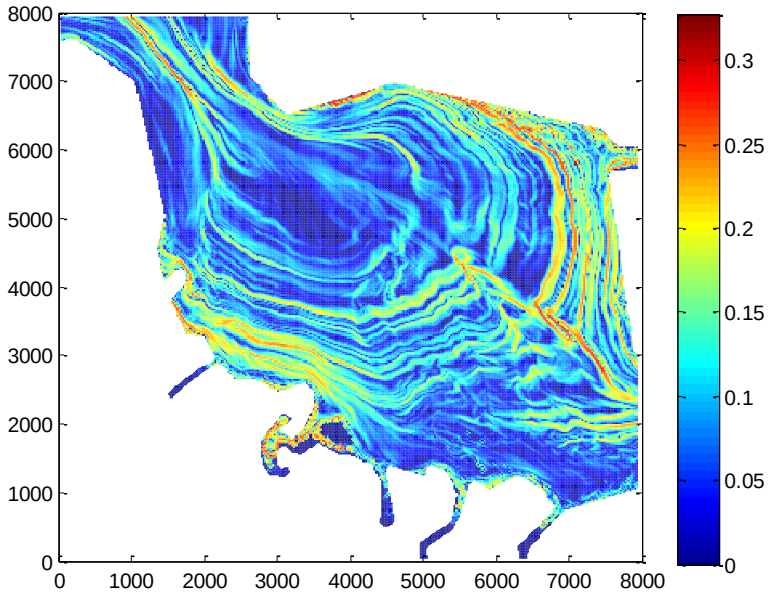

Figure 4.7: FTLE field (h^{-1}) for the case with no wind forcing. Initial particle release t_0 is at high tide, and FTLE is calculated using integration time period T = 12 hours, corresponding to full ebb-flood tidal cycle.

rotate the orientation of these ridgelines in a counter-clockwise direction on both sides of the channel. Likewise, the near-boundary LCS ridgelines are present in the FTLE field for the SW wind case, but the effect of the wind is to rotate the orientation of the ridgelines in a clockwise direction on both sides of the channel. For both cross-axis wind cases, the effects of the wind on Lagrangian transport also create patches of high FTLE near the boundary, which can be seen near the western boundary in the NE wind case and near the northern boundary in the SW wind case. In both cases, these patches also connect to a single prominent LCS ridgeline which extend into the Dumbarton Narrows.

4.3.3 Exchange and Connectivity Results

Figure 4.12 shows the connectivity analysis results from the particle-tracking results for the Far South Bay particle release for each of the five cases. For each case, about two-thirds of the initial volume at high water in the Far South Bay exits the Dumbarton Narrows and is located in the main South Bay at low water 6 hours after release. For the case with no wind, the proportion of particles remaining in the main South Bay at high water 12 hours after release is only 0.03, and the remainder of the particles return to the Far South Bay. This proportion is increased slightly in the cross-axis wind cases, to 0.05 for the SW wind case and 0.11 for the NE wind case. The proportion of particles which are exchanged into the main South Bay from the Far

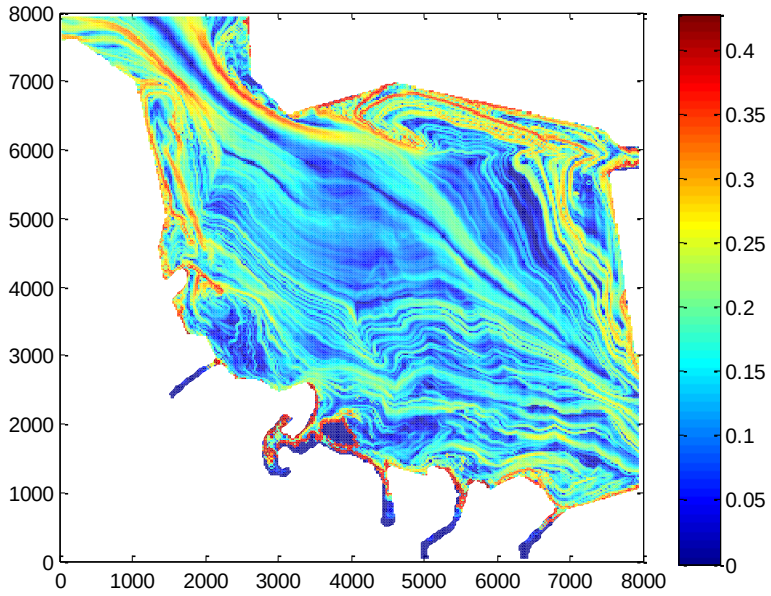

Figure 4.8: FTLE field (h^{-1}) for the case with wind forcing directed from the northwest (NW). Initial particle release t_0 is at high tide, and FTLE is calculated using integration time period T = 12 hours, corresponding to full ebb-flood tidal cycle.

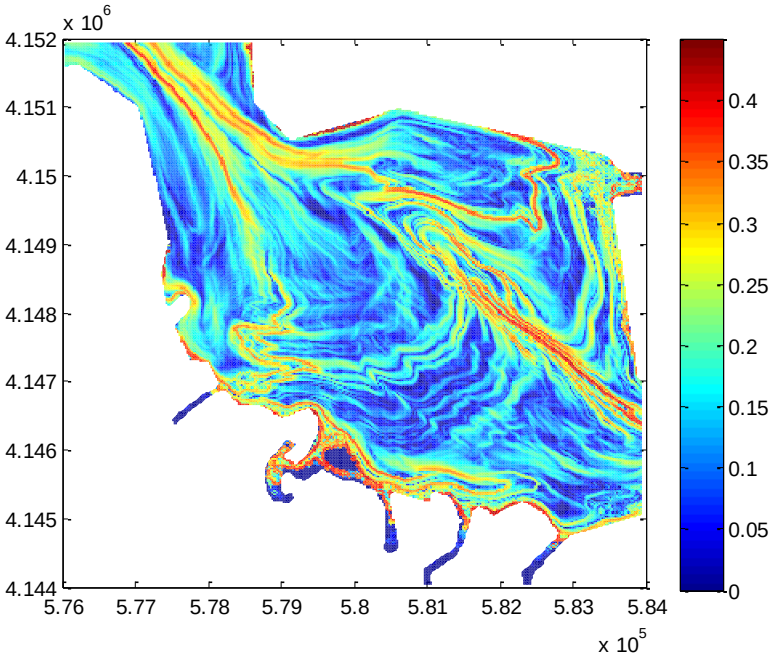

Figure 4.9: FTLE field (h^{-1}) for the case with wind forcing directed from the southeast (SE). Initial particle release t_0 is at high tide, and FTLE is calculated using integration time period T = 12 hours, corresponding to full ebb-flood tidal cycle.

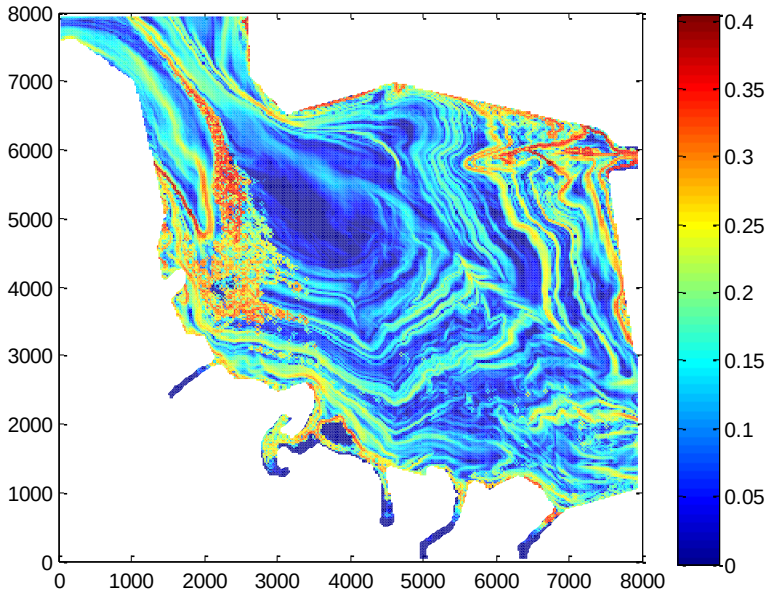

Figure 4.10: FTLE field (h^{-1}) for the case with wind forcing directed from the northeast (NE). Initial particle release t_0 is at high tide, and FTLE is calculated using integration time period T = 12 hours, corresponding to full ebb-flood tidal cycle.

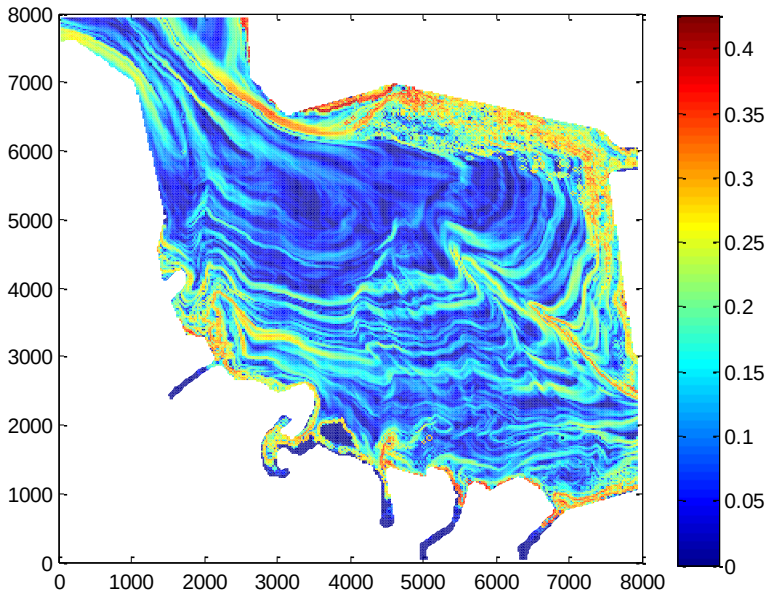

Figure 4.11: FTLE field (h^{-1}) for the case with wind forcing directed from the southwest (SW). Initial particle release t_0 is at high tide, and FTLE is calculated using integration time period T = 12 hours, corresponding to full ebb-flood tidal cycle.

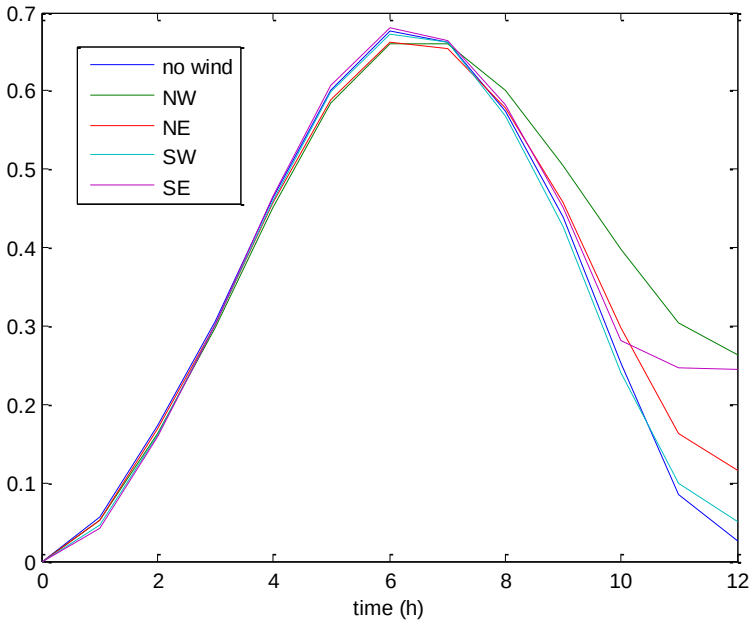

Figure 4.12: Connectivity results showing proportion of water released in the Far South Bay which is located in the Main South Bay over the tidal period (ebb-flood) for each of the wind forcing cases.

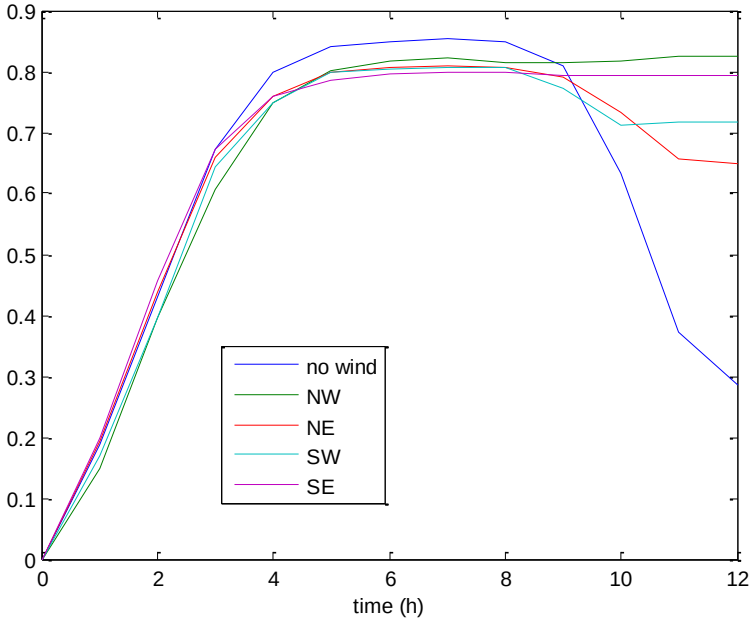

Figure 4.13: Connectivity results showing proportion of water released in the Palo Alto Baylands which is located in the Far South Bay over the tidal period (ebb-flood) for each of the wind forcing cases.

South Bay over a single tidal cycle is by far the greatest in the along-axis wind cases, 0.24 for the SE wind case and 0.26 for the NW wind case.

Figure 4.13 shows the connectivity analysis results from the particle-tracking results for the Palo Alto Baylands particle release for each of the five cases. For each case, a proportion of about 0.8 of the initial volume at high water exits the Baylands and is located in the Far South Bay at low water 6 hours after release. For the case with no wind, the proportion of particles remaining in the main South Bay at high water 12 hours after release is about 0.3, and the remainder of the particles return to the Far South Bay. This proportion is increased significantly in the cross-axis wind cases, to 0.65 for the NE wind case and 0.72 for the SW wind case, and is increased even further in the along-axis wind cases, to about 0.79 for the SE wind case and 0.82 for the NW wind case.

4.4 Discussion

The particle-tracking and LCS results in the previous section reveal the effects of wind in various directions on estuarine transport, including the effects of interactions between winds and tides. In general, the effect on depth-averaged transport of constant, uniform wind on a basin with variable bathymetry is to create residual circulation which is in the same direction as the wind for shallow areas, and a return flow in the opposite direction for deeper areas (Csanady 1973, Wong 1994). This wind-driven recirculation occurs in all four constant wind cases for both basins north and south of the Dumbarton Narrows (i.e., the main South Bay basin and the Far South Bay). These residual circulation patterns are combined with the non-wind driven transport patterns created by the interaction of barotropic tidal forcing and estuarine topography and bathymetry to influence overall estuarine transport. In the next sections, this effect of wind-driven recirculation on the particle-tracking and LCS results for the wind-forced cases will be discussed.

4.4.1 Particle-Tracking and LCS

The effect of the constant wind forcing for both along-axis wind cases (NW and SE) is to create residual circulation which is in the same direction for both basins. The NW wind creates upestuary transport in the shallower shoals and downestuary transport in the deeper channel for both the main South Bay and the Far South Bay, and the SE wind creates transport in the opposite direction, which is apparent in the particle-tracking results (Figures 4.3 and 4.4). For the cross-axis wind cases (NE and SW), there is not a strong recirculation set up in the Far South Bay, but the along-axis bathymetry gradient causes wind-driven recirculation in the main South Bay. For the NE wind case, there is wind-driven transport towards the southwest in the shallower areas near the Dumbarton Narrows and wind-driven transport towards the northeast in the deeper areas further from the Narrows, and transport in the opposite direction occurs for the SW wind case. This wind-driven circulation in the main South Bay is important to the transport of particles released at high tide in the Far South Bay which are transported past the Dumbarton Narrows at low slack water. During this period, these particles experience a general clockwise

or counter-clockwise rotation for the NE or SW wind cases, respectively, causing the overall residual upestuary or downestuary transport near the Dumbarton Narrows observed in the particle-tracking results.

The results of the FTLE and LCS analysis help to analyze the effects of the interaction of the wind-driven currents on the Lagrangian particle transport in the Far South Bay. In particular, it is useful to analyze the LCS results for each wind-driven case as compared to the LCS results for the base case with no wind forcing. The near-boundary LCS ridgelines present in the FTLE fields for all five cases are caused by tidal transport mechanisms where Lagrangian particle regions released at high water during the tidal cycle experience Lagrangian shear straining and deformation as they approach the boundary during the flood tide. In the previous section, these lines were observed to be rotated in various directions for each of the wind-forced cases. In each of these cases, the direction of rotation of the LCS ridgelines can be attributed to the overall residual rotation in the opposite direction which the particles experience over the tidal cycle. For example, particle regions which experience an overall counter-clockwise rotation approach the boundary on the flood tide in such a way that the LCS ridgelines in FTLE (which, importantly, is mapped to initial particle position) are rotated in a clockwise direction.

This effect of residual rotation induced by the wind on the LCS analysis of tidal transport is illustrated schematically in Figure 4.14. In this case, the division between two subregions (colored blue and green) within a combined high-tide release region is an LCS ridgeline in the 12-hour FTLE which is produced by shear straining as the subregions approach the boundary on the flood. Subpanels 14a-14c show the base case with no wind, while subpanels 14d-14f show the effect of wind-induced rotation. In both cases, as the combined region approaches the boundary on the flood, strain parallel to the boundary amplifies shear separation within the combined region. This shear produces high residual separation in the FTLE field calculated from T = 0 h to T = 12 h, which is subsequently identified as the LCS ridgeline (shown as a black dotted line in subpanels 14a and 14d) used to define the boundary between the two subregions. It is important to note that definition of the boundary between the two subregions in Fig. 4.14 at T = 0 h is contingent on knowledge of the shear displacement observed between the final subregion positions after the 12-hour integration period, representing residual transport over the full tidal cycle, which is provided by the FTLE and LCS analysis (also note that actual straining of the subregions is not shown in the figures, in order to more clearly illustrate rotational effects). Comparison of the two cases shows that although the sense of the wind-induced rotation is counter-clockwise, the net effect of the residual circulation is clockwise rotation of the LCS ridgeline, since FTLE is mapped to initial position.

With this schematic in mind, we can interpret the observed rotation of the LCS ridgelines in the FTLE fields as resulting from wind-induced residual rotation over the tidal period. In the results for the Far South Bay particle release, the rotation of the particles is particularly affected by the residual circulation experienced during low water in the main South Bay north of the Dumbarton Narrows, which is indicated by the black arrows in Figures 4.2-4.6. For the along-axis NW wind case, particles to the northeast of the channel experience a clockwise rotation and

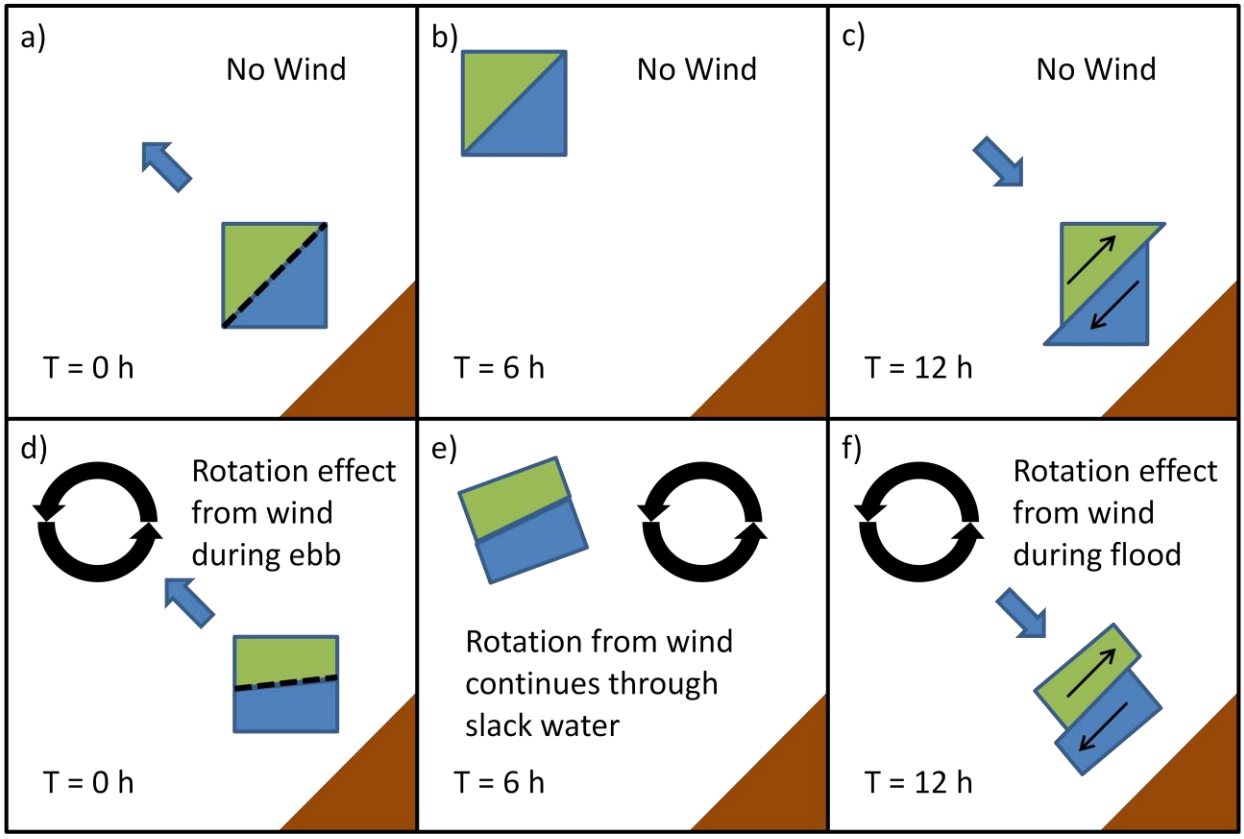

Figure 4.14: Schematic illustrating the effect of wind-induced residual rotation on LCS identified by forward-time FTLE. Subpanels a-c show the case with no wind, and subpanels d-f show the case with rotation from wind. The LCS dividing the blue and green subregions is represented by the black dotted line at T = 0 h, and counter-clockwise rotation from wind effects results in clockwise rotation of the LCS (cf. subpanels a and d). Note that the initial location of the LCS dividing the two subregions at T = 0 h is by definition a result of transport processes causing separation (in this case amplification of shear perturbations by tidal straining parallel to the boundary) over the entire integration time period of T = 12 h.

particles to the southwest of the channel experience a counter-clockwise rotation, hence the LCS ridgelines are rotated in the opposite direction in the FTLE field. For the cross-axis NE wind case, particles on both sides of the channel which are influenced by the wind-driven recirculation north of the Dumbarton Narrows during low slack water experience a general clockwise rotation, and hence the LCS ridgelines are rotated in a counter-clockwise direction. The opposite transport from the NW wind case occurs for the SE wind case, and the opposite transport from the NE wind case occurs for the SW wind case. Thus, the rotation of the LCS ridgelines in the FTLE field reveal the general effect of circulation driven by constant wind forcing on the structure of estuarine transport in each of the four wind direction cases.

Besides the near-boundary LCS ridgelines, other LCS features can also be analyzed as resulting from the influence of wind-driven transport. For both along-axis wind cases, transport

in the channel and shoals in and near the Dumbarton Narrows is in opposing directions, creating prominent LCS ridgelines caused by Lagrangian shear. For the cross-axis wind cases, dominant transport near the Dumbarton Narrows is either clockwise or counter-clockwise, creating only one dominant shear-induced LCS ridgeline near the Dumbarton Narrows. Additionally, wind- and tide-induced interaction of particle transport with the estuarine perimeter over the tidal cycle causes Lagrangian particle separation which creates patches of high FTLE near the western boundary for the NE wind case and near the northern boundary for the SW wind case. For the SE wind case, the LCS ridgeline in the upestuary section of the main channel results from particle separation caused by the wind-driven dual circulation (downestuary in the shoals, upestuary in the channel) in the Far South Bay, which creates divergence as flow approaches the southeastern end of the channel in the Far South Bay and splits towards either shoal.

4.4.2 Wind Effects on Exchange and Connectivity

In the particle-tracking and LCS results, the effect of the wind on estuarine transport appears to be greater in the along-axis wind cases than in the cross-axis wind cases. This is confirmed in the exchange and connectivity results, where for both the Far South Bay particle release and the Palo Alto Baylands release, exchange and connectivity was lowest for the no wind case, was increased in the cross-axis wind cases (NE and SW), and was greatest in the along-axis wind cases (NW and SE).

For the Far South Bay particle release, in all four wind cases, wind-induced circulation in the main South Bay increases flushing at the Dumbarton Narrows, as discussed in the particle-tracking and LCS results, and along-axis winds have the greatest effect on exchange and connectivity between the Far South Bay and the main South Bay, due to enhanced wind-driven exchange in the along-axis direction. The connectivity effects of the along-axis winds can also be seen to some extent in the LCS results for each case. In the SE wind case (Figures 4.4 and 4.9), water is flushed from the northern and western shoals of the Far South Bay, with clear LCS ridgelines indicating the boundaries between water that is flushed or retained. In the NW wind case (Figures 4.3 and 4.8), water is flushed from the middle of the Far South Bay, with strong convergence in this area and thus no prominent LCS ridgelines other than those caused by lateral shear due to intensified exchange in the Dumbarton Narrows. In the cross-axis (NE and SW) wind cases, a single shear LCS in the channel indicates exchange at the Dumbarton Narrows, and it is apparent that a larger region in the northwestern shoal is flushed in the NE wind case than the region in the northern shoal that is flushed in the SW wind case, which is consistent with the higher connectivity result for the NE wind as compared to the SW wind (Figures 4.10 and 4.11).

The results for the Palo Alto Baylands particle release are generally similar to those for the Far South bay release, except that particles are mainly affected by wind-induced circulation in the Far South Bay, with resulting increases in exchange and connectivity between the Palo Alto Baylands and the Far South Bay. The differences between the two connectivity releases come from the large difference in scale between the initial release regions, where the volumes of the Far South Bay and the Palo Alto Baylands at high tide are roughly 8.7×10^7 m^3 and 2.5×10^5 m^3

respectively, or a difference in volume of over two orders of magnitude. Thus the effect of wind on exchange and connectivity between the Palo Alto Baylands and the Far South Bay is not readily apparent from the LCS results, although they are consistent with the increased residual circulation observed in the wind cases, especially for the along-axis winds. Whereas in the Far South Bay release connectivity estimates for one tidal cycle ranged from 0.03 for the case with no wind to nearly 0.3 in the along-axis wind cases, in the Palo Alto Baylands release, even in the case with no wind, about 0.3 of the initial volume is flushed from the slough after a single a tidal cycle, due to the residual circulation in the Far south Bay which is present even without wind forcing. In the along-axis wind cases, this proportion was increased to about 0.8, such that effectively none of the water which exits the Palo Alto Baylands on the ebb tide reenters the Baylands on the subsequent flood tide, due to the wind-forced circulation in the Far South Bay.

Another difference between the two connectivity analyses is that for the case of the Far South Bay particle release, exchange between the Far South Bay and the main South Bay is in the direction of the main axis of the estuary (NW-SE), whereas for the case of the Palo Alto Baylands particle release, exchange is in the direction perpendicular to the main axis of the estuary (NE-SW). In both releases, exchange and connectivity were greatest in the same wind cases, i.e. the NW and SE cases, because wind-induced circulation was strongest in the along-axis wind cases. From this we can conclude that for the two releases it is the magnitude of wind-induced circulation that is important for determining which wind direction has the greatest effect on exchange and connectivity, rather than the direction of exchange with respect to the wind forcing.

4.5 Conclusions

The results of this study demonstrate that wind direction has significant effects on estuarine transport, which can be analyzed using particle-tracking and LCS analysis techniques. The depth-averaged effect of constant wind forcing is to set up circulation in the direction of wind with return flow in deeper areas. However, when this wind-driven residual circulation is combined with the periodic barotropic tide and complex boundaries as in estuaries, hydrodynamic transport becomes much more complex and chaotic, thus necessitating the use of Lagrangian transport analysis methods. Using particle-tracking and LCS to analyze transport mechanisms over a single tidal cycle, we are able to determine the effects of wind-driven circulation on the overall structure of estuarine transport in the domain for along-axis and cross-axis wind cases. We find that residual wind circulation affects the high-tide release FTLE fields and LCS by inducing rotation in the two-dimensional depth-averaged velocity field over the tidal period, and that regions of water experience rotation in the advective velocity field as they are transported during the tidal cycle, which in turn creates rotation in the opposite sense of the LCS ridgelines in the FTLE field calculated using initial particle positions.

In addition, we are also able to quantify the effect of wind direction on estuarine exchange and connectivity. We find that exchange and connectivity are greatly enhanced by wind-induced residual circulation, and that this effect is generally greatest when wind is aligned with in the

direction of the main axis of the estuary. The scale of the regions being analyzed has a large effect on the connectivity results and wind effects between regions, as is consistent with results from Chapter 2 of this dissertation. The connectivity analysis in this study is effectively a measure of the tidal exchange ratio *R* defined in Chapter 2, which is used to estimate estuarine flushing and residence times using tidal prism methods. The results of this study show that exchange and connectivity measured by *R* is greatly affected by the presence of wind forcing and wind direction, where *R* was increased an order of magnitude by along-axis winds for particle releases in the Far South Bay region, and also by the scale of exchange and connectivity, where *R* was generally much greater for particle releases in the much smaller Palo Alto Baylands region.

Finally, we note that from the connectivity results that the tidal signal of connectivity, caused by tidal velocities over the tidal cycle, can be quite large relative to the final connectivity results at the end of the tidal cycle. As we can see from the case of no wind for the Far South Bay particle release, this large tidal signal for connectivity can reverse itself over the tidal cycle for the case of symmetric tides, such that net exchange is close to zero. This implies that although for certain applications connectivity analyses are usually done using fixed time scales (e.g. Cowen at al. 2006, North et al. 2008), the connectivity in regions with large tidal forcing over short time scales can be thought of as time variable, and highly dependent on tidal phase. For longer time scales, the effect of the residual flow after removing the tidal signal becomes significant and controls long-term transport, and the connectivity is the result of the cumulative effects of many individual tidal cycles. To calculate this cumulative effect, exchange and connectivity results from individual tidal cycles, as in the results of this study, can be extrapolated to obtain connectivity results for long-term estuarine transport. This can be done using only analysis from a tidal cycle of only one amplitude in the case of repeating identical tides, but for analyzing exchange over longer periods where tides exhibit significant spring-neap variation the long-term time-variable, connectivity analysis should include the effects of varying tidal amplitude.

Although the magnitude of the wind circulation may be smaller than the tidal velocities and tide-induced displacements, the results show that for the Far South Bay particle release the wind forcing has a far greater effect on exchange and connectivity over the full tidal cycle than exchange from tides alone. For the smaller Palo Alto Baylands region, tidal asymmetries result in residual circulation so that significant net tidal transport occurs even in the case without wind forcing, but wind is still shown to have a large effect on the overall exchange and connectivity. From these results, we see that tide and wind forcing can have different relative significance depending on the timescales of interest for transport. For our results in the Far South Bay, we see that tidal forcing can be important for transport processes over timescales shorter than the tidal period, e.g. sediment transport from resuspension and deposition on different phases of the tide, but wind-forced residual circulation is likely to be much more important for long-term transport processes which occur over long time scales of multiple tidal cycles.

Chapter 5: Summary and Future Considerations

The study of hydrodynamic transport in estuaries is complex and multifaceted, with numerous methods and approaches to characterizing and analyzing the multiple scales and mechanisms of estuarine transport. In this dissertation work, I have focused on the study of hydrodynamic exchange processes near the estuarine perimeter, to contribute to a better understanding of perimeter estuarine transport processes which are important for environmental and ecological functions of estuaries and their perimeter habitats. In particular, I have focused my analysis on analyzing transport in South San Francisco Bay, which is a highly populated, environmentally and economically important estuary with multiple environmental management and restoration concerns, and which serves as a useful model example which is representative of shallow tidal estuarine systems. I have studied transport in this system using various Lagrangian analysis techniques applied to numerical modeling results and observations, in order to answer questions about hydrodynamic transport near the estuarine perimeter, including the scales of estuarine perimeter exchange and transport, the application of Lagrangian analysis techniques to the study of estuarine dispersion as affected by estuarine topography, and the effects of wind forcing on estuarine exchange and connectivity.

In Chapter 2, the exchange between an estuary and an intertidal marsh and slough was studied by applying a method using scalar class analysis to analyze exchange at the mouth of the perimeter slough in the Palo Alto Baylands in South San Francisco Bay. This method had been developed for estimating exchange at the mouth of much larger estuarine systems, and had not previously been applied to smaller-scale transport at the estuarine perimeter. The results of the method as applied to field observations produced estimates of exchange which were far greater than those expected from previous results in larger estuarine systems, and numerical modeling was introduced as a way of testing and verifying these results, as well as analyzing the validity of the method and its assumptions. When the model results were compared to the field results, it was found that the assumptions of the method with regard to mixing in tidal exchange were likely invalid in systems with very large tidal prism volume compared to total system volume. This demonstrated that the scale of hydrodynamic transport in estuarine perimeter habitats produces significant differences in exchange characteristics between perimeter sloughs and larger estuarine systems, and that methods which have been developed to analyze exchange in conventional estuarine systems must be carefully assessed before being applied to analyze small-scale estuarine perimeter transport. The modeling results were thus re-analyzed using a reinterpretation of the scalar class analysis method, producing an estimate of mixing and exchange characteristics of tidal exchange in small estuarine perimeter sloughs.

In Chapter 3, the Lagrangian techniques of particle-tracking and Lagrangian coherent structure (LCS) analysis using finite-time Lyanpunov exponent (FLTE) fields were applied to the study of tidal dispersion near the estuarine perimeter. Particle-tracking was applied to tidally forced numerical hydrodynamic modeling results for the region of the Far South Bay south of the Dumbarton Narrows in South San Francisco Bay, and the particle trajectory maps were used to calculate spatial FTLE fields, where ridgelines were identified as LCS representing local maxima of Lagrangian particle separation. These techniques have recently been applied to oceanic and estuarine flows, but have not previously been used to analyze the structure of estuarine transport near the estuarine perimeter on tidal timescales. The results demonstrated that perimeter interactions of tides with local estuarine topographical features significantly affected the Lagrangian transport of particle subregions identified and defined using LCS analysis. The trajectories of these Lagrangian subregions and their relative displacements over the tidal cycle was analyzed, and the effect of perimeter interactions was estimated to be comparable to other known estuarine dispersion mechanisms such as tidal vertical shear dispersion. These results implied that studies of tidal dispersion near the estuarine perimeter must include the effects of tidal interactions with complex estuarine perimeter topography, potentially including individual local topographic features. Thus, modeling using real estuarine bathymetric and topographic information may be preferable to modeling using idealized estuarine bathymetry in studies of tidal dispersion where such effects cannot be modeled using simple parameterizations. In addition, the Lagrangian deformation mechanism of tidal perimeter interactions was interpreted using concepts borrowed from dynamical systems analysis, and tidal straining was observed to amplify small perturbations induced by residual flows produced by local topographic and bathymetric features, producing significant Lagrangian dispersion over the tidal cycle.

In Chapter 4, the effects of wind forcing on estuarine exchange and connectivity were studied using the modeling and Lagrangian analysis techniques developed in Chapter 3. The particle-tracking and LCS analysis using FTLE were applied to numerical hydrodynamic modeling results for the Far South Bay, with the inclusion of wind forcing in various directions in addition to the tidal forcing. Although wind forcing has been studied in estuarine systems, previous studies have not focused on the effects of wind direction on estuarine exchange and connectivity near the estuarine perimeter, and have not used LCS analysis to study these effects. In addition to the LCS analysis, time-varying connectivity analyses of exchange between regions were applied over the tidal cycle between the Far South Bay and the main South Bay as well as between the perimeter slough at the Palo Alto Baylands and the Far South Bay. The results showed that wind forcing increased hydrodynamic exchange and connectivity between the main South Bay, the Far South Bay and the Palo Alto Baylands for all wind directions, with the most significant increase in exchange and connectivity when wind forcing was aligned with the main axis of the estuary. The LCS ridgelines were also found to be affected by wind-induced residual circulation, where residual rotation from wind-induced circulation produced rotation in the opposite sense of LCS ridgelines for FTLE fields mapped to initial particle locations. Finally, the concept of time-varying connectivity was used to interpret the large tidal variations in

comparison with relatively small residual transport, which was found to have implications for estuarine transport over short and long timescales for processes such as sediment transport and ecological population propagation.

As a whole, these results have demonstrated the utility of Lagrangian analysis techniques for studying hydrodynamic exchange in estuarine perimeter habitats. The study of point-to-point exchange in complex systems such as estuaries is essential to our understanding of hydrodynamic connectivity in these environments. The tidal exchange and transport results from each chapter contributes to our knowledge of the hydrodynamic processes controlling connectivity in estuarine perimeter habitats, which is relevant to answering many of the questions related to environmental management of these systems. A fundamental knowledge of transport is necessary for controlling contaminant transport, such as outfalls from wastewater treatment plants and contaminants which are bound to sediments. The study of transport of sediment itself has many applications for management of the environmental quality of estuaries, for example restoration of wetland habitats in the perimeter of San Francisco Bay. Ecological considerations such as control of invasive species, management of eutrophication and prevention of harmful algal blooms, and population dynamics of larval recruitment and seagrass colonization are all directly related to hydrodynamic transport and connectivity. The analysis of flushing and residence time based on tidal exchange, the analysis of Lagrangian tidal transport and effects of perimeter interactions, and the Lagrangian analysis of the effects of wind forcing on estuarine transport and connectivity explored in the previous chapters all contribute to our understanding of estuarine hydrodynamic transport for such applications.

The results of the studies presented in this dissertation have shown that there is still much to learn about hydrodynamic exchange in estuaries and their perimeters. Future advances in understanding may come from novel applications of analysis techniques to the study of hydrodynamic exchange and transport, such as the Lagrangian analysis methods of scalar class analysis, FTLE and LCS used in this work to study small-scale perimeter exchange, dispersive effects of tidal perimeter interactions, and wind effects on estuarine exchange and connectivity. Although these results have produced new insights into hydrodynamic exchange near the estuarine perimeter, there are still many questions to be asked and answered by future studies of estuarine exchange, using different model systems, parameter spaces, and analysis techniques, and focusing on different estuarine forcings and transport mechanisms. This work has focused on characterization of general hydrodynamic transport processes near the estuarine perimeter, but specific applications such as transport of salinity, sediment, and biota introduce additional dynamics will require additional analysis before they are fully understood. Thus, future study of estuarine hydrodynamics with respect to specific environmental goals and applications is necessary to produce further knowledge and understanding of hydrodynamic exchange which can be applied to environmental management of estuaries and their perimeter habitats.

References

Agrawal, Y.C., and D.G. Aubrey. 1992. Velocity observations above a rippled bed using laser Dopler velocimetry. J. Geophys. Res.- Oceans 97: 20249-20259.

Armi, L., and D.M. Farmer. 1986. Maximal two-layer exchange through a contraction with barotropic net flow. J. Fluid Mech. 164: 27-51.

Banas, N.S., Hickey, B.M., MacCready, P., and J.A. Newton. 2004. Dynamics of Willapa Bay, Washington: a highly unsteady, partially mixed estuary. Journal of Physical Oceanography 34: 2413-2427.

Beerens, S.P., H. Ridderinkhof, and J.T.F. Zimmerman. 1994. An analytical study of chaotic stirring in tidal areas. Chaos, Solitons, & Fractals 4: 1011-1029.

Benilov, A.Y., O.A. Kouznetsov, and G.N. Panin. 1974. On the analysis of wind wave-induced disturbances in the atmospheric turbulent surface layer. Boundary-Layer Meteorology 6: 269-85.

Boffetta, G., Lacorata, G., Radaelli, G., and A. Vulpani. 2001. Detecting barriers to transport: a review of different techniques. Physica D 159: 58-70.

Brand, A., J.R. Lacy, and K. Hsu, D. Hoover, S. Gladding, and M.T. Stacey. 2010. Wind-enhanced resuspension in the shallow waters of South San Francisco Bay: Mechanisms and potential implications for cohesive sediment transport. J. Geophys. Res.- Oceans 115 [doi:10.1029/2010JC006172].

Branicki, M., and R. Malek-Madani. 2010. Lagrangian structure of flows in the Chesapeake Bay: challenges and perspectives on the analysis of estuarine flows. Nonlin. Proc. Geophys. 17: 149-168.

Bricker, J.D., and S.G. Monismith. 2007. Spectral wave-turbulence decomposition. J. Atmos. Ocean. Tech. 24: 1479-1487.

Chao, S.Y., and W.C. Boicourt. 1986. Onset of estuarine plumes. Journal of Physical Oceanography 16: 2137-2149.

Chatwin, P.C. 1976. Some remarks on the maintenance of the salinity distribution in estuaries. Estuarine Coast. Mar. Sci. 4:555-66.

Chen, S.N. and L.P. Sanford. 2009. Axial wind effects on stratification and longitudinal salt transport in an idealized, partially mixed estuary. Journal of Physical Oceanography 39: 1905-1920.

Chen, S.N., Sanford, L.P. and D.K. Ralston. 2009. Lateral circulation and sediment transport driven by axial winds in an idealized, partially mixed estuary. Journal of Geophysical Research – Oceans 114: C12006.

Cloern, J.E. 2007. Habitat connectivity and ecosystem productivity: implications from a simple model. Am. Nat. 169: E000-E000.

Cowen, R.K., C.B. Paris, and A. Srinivasan. 2006. Scaling of Connectivity in Marine Populations. Science 311: 522-527.

Cowen, R.K. and S. Sponaugle. 2009. Larval Dispersal and Marine Population Connectivity. Annu. Rev. Mar. Sci. 1: 443-66.

Csanady, G.T. 1973. Wind-induced barotropic motions in long lakes. J. Phys. Oceanogr. 3: 429-438.

Elder, J.W. 1959. The dispersion of marked fluid in turbulent shear flow. J. Fluid Mech. 5: 544-560.

Feddersen, F., and A.J. Williams. 2007. Direct estimation of the Reynolds stress vertical structure in the nearshore. J. Atmos. Ocean. Tech. 24: 102-116.

Fischer, H.B. 1972. Mass transport mechanisms in partially stratified estuaries. Journal of Fluid Mechanics 53: 671-687.

Fischer, H.B. 1976. Mixing and Dispersion in Estuaries. Annual Review of Fluid Mechanics 8: 107-133.

Fischer, H.B., E.J. List, R.C.Y. Koh, J. Imberger, and N.H. Brooks. 1979. Mixing in Inland and Coastal Waters. Academic Press.

Fong, D., S.G. Monismith, M.T. Stacey, and J.R. Burau. 2009. Turbulent Stresses and Secondary Currents in a Tidal-Forced Channel with Significant Curvature and Asymmetric Bed Forms. J. Hydraul. Eng.-ASCE 135: 198-208.

Fram, J.P., M.A. Martin, and M.T. Stacey. 2007. Dispersive fluxes between the coastal ocean and a semienclosed estuarine basin. Journal of Physical Oceanography 37: 1645-1660.

Fringer, O.B., M. Gerritsen, and R.L. Street. 2006. An unstructured-grid, finite-volume, nonhydrostatic, parallel coastal ocean simulator. Ocean Modelling 14: 139-173.

Gerbi, G.P., J.H. Trowbridge, J.B. Edson, A.J. Plueddemann, E.A. Terray, and J.J. Fredericks. 2008. Measurements of momentum and heat transfer across the air-sea interface. J. Phys. Oceanogr. 38: 1054-1072.

Grant, W.D. and Madsen, O.S., 1979. Combined Wave and Current Interaction with a Rough Bottom. Journal of Geophysical Research 84: 1797-1808.

Hansen, D.V., and M. Rattray. 1965. Gravitational Circulation in Straits and Estuaries. J. Mar. Res. 23: 104-122.

Hansen, D.V. and M. Rattray. 1966. New Dimensions in estuary classification. Limnol. Oceanogr. 11: 319-26.

Herbers, T.H.C., and R.T. Guza. 1993. Velocity observations above a rippled bed using laser-Doppler velocimetry - comment. J. Geophys. Res.- Oceans 97: 20331-20333.

Hetland, R.D., and W.R. Geyer. 2004. An idealized study of the structure of long, partially mixed estuaries. Journal of Physical Oceanography 34: 2677-2691.

Hsu, K., M.T. Stacey, and R.C. Holleman. 2013. Exchange between an estuary and an intertidal marsh and slough. Estuaries and Coasts 36: 1137-1149.

Huhn, F., A. von Kameke, S. Allen-Perkins, P. Montero, A. Venancio, and V. Perez-Munuzuri. 2012. Horizontal Lagrangian transport in a tidal-driven estuary-Transport barriers attached to prominent coastal boundaries. Continental Shelf Research 39-40: 1-13.

Ivey, G.N. 2004. Stratification and mixing in sea straits. Deep-Sea Research Part II-Topical Studies in Oceanography 51: 441-453.

Jouon, A., P. Douillet, S. Ouillon, and P. Fraunie. 2006. Calculations of hydrodynamic time parameters in a semi-opened coastal zone using a 3D hydrodynamic model. Continental Shelf Research 26: 1395-1415.

Kaimal, J., J.C. Wyngaard, Y. Izumi, and O.R. Cote. 1972. Spectral characteristics of surface-layer turbulence. Quart. J. Roy. Meteor. Soc. 98: 563-589.

Kitaigorodskii, S.A., M.A. Donelan, J.L. Lumley, and E.A. Terray. 1983. Wave turbulence interactions in the upper ocean .2. Statistical characteristics of wave and turbulent components of the random velocity-field in the marine surface-layer. J. Phys. Oceanogr. 13: 1988-1999.

Lee, X., W. Massmann, and B. Law. 2004. Handbook of micrometeorology—a guide for surface flux measurement and analysis. Kluwer.

Lerczak, J.A., and W.R. Geyer. 2004. Modeling the lateral circulation in straight, stratified estuaries. Journal of Physical Oceanography 34: 1410-1428.

Li, C., and J. O'Donnell. 1997. Tidally driven residual circulation in shallow estuaries with lateral depth variation. J. Geophys. Res. 102: 27915-27929.

Li, C., and J. O'Donnell. 2005. The effect of channel length on the residual circulation in tidally dominated channels. J. Phys. Oceanogr. 35: 1826-1840.

Lucas L.V., J.R. Koseff, S.G. Monismith, and J.K. Thompson. 2009. Shallow water processes govern system-wide phytoplankton bloom dynamics: a modeling study. J. Mar. Sys. 75: 70-86.

Lumley, J., and E. Terray. 1983. Kinematics of turbulence convected by a random wave field. J. Phys. Oceanogr. 13:2000-2007.

MacCready, P., R.D. Hetland, and W.R. Geyer. 2002. Long-term isohaline salt balance in an estuary. Continental Shelf Research 22: 1591-1601.

MacCready, P., and W.R. Geyer. 2010. Advances in estuarine physics. Annual Review of Marine Science 2: 35-58.

MacCready, P. 2011. Calculating estuarine exchange flow using isohaline coordinates. Journal of Physical Oceanography 41: 1116-1124.

MacDonald, D.G. 2006. Estimating an estuarine mixing and exchange ratio from boundary data with application to Mt. Hope Bay (Massachusetts/Rhode Island). Estuarine, Coastal and Shelf Science 70: 326-332.

MacVean, L.J., and M.T. Stacey. 2011. Estuarine dispersion from tidal trapping: a new analytical framework. Estuaries And Coasts 34: 45-59.

Monsen, N.E., J.E. Cloern, L.V. Lucas, and S.G. Monismith. 2002. A comment on the use of flushing time, residence time, and age as transport time scales. Limnology and Oceanography 47: 1545-1553.

North, E.W., Z. Schlag, R.R. Hood, M. Li, L. Zhong, T. Gross, and V.S. Kennedy. 2008. Vertical Swimming behavior influences the dispersal of simulated oyster larvae in a coupled particle-tracking and hydrodynamic model of Chesapeake Bay. Mar. Ecol. Prog. Ser. 359: 99-115.

Nunes, R.A. and J.H. Simpson. 1985. Axial convergence in a well-mixed estuary. Estuarine Caost. Shalef Sci. 20: 637-49.

O'Donnell, J. 1990. The formation and fate of a river plume – a numerical-model. Journal of Physical Oceanography 20: 551-569.

Okubo, A. 1973. Effect of shoreline irregularities on streamwise dispersion in estuaries and other embayments. Neth. J. Sea Res. 6: 213-224.

Peng, J., and J. O. Dabiri. 2009. Transport of inertial particles by Lagrangian coherent structures: application to predator-prey interaction in jellyfish feeding. J. Fluid Mech. 623: 75-84.

Ridderinkhof, H., and J. T .F. Zimmerman. 1992. Chaotic stirring in a tidal system. Science 258: 1107-1111.

Sanford, L.P., W.C. Boicourt, and S.R. Rives. 1992. Model for estimating tidal flushing. Journal of Waterway Port Coastal and Ocean Engineering-ASCE 118: 635-654.

Shadden, S. C., F. Lekien, and J. E. Marsden. 2005. Definition and properties of Lagrangian coherent structures from finite-time Lyapunov exponents in two-dimensional aperiodic flows. Physica D 212: 271-304.

Shadden, S. C., F. Lekien, J. D. Paduan, F. P. Chavez, and J. E. Marsden. 2009. The correlation between surface drifters and coherent structures based on high-frequency radar data in Monterey Bay. Deep-Sea Research Part II 56: 161-172.

Shaw, W.J., and J.H. Trowbridge. 2001. The direct estimation of near-bottom turbulent fluxes in the presence of energetic wave motions. J. Atmos. Ocean. Tech. 18: 1540-1557.

Simpson, J.H., Brown, J., Matthews, J., and G. Allen. 1990. Tidal straining, density currents, and stirring in the control of estuarine stratification. Estuaries 13: 125-32.

Smith, R. 1976. Longitudinal dispersion of a buoyant contaminant in a shallow channel. J. Fluid Mech. 78: 677-688.

Smith, R. 1983. Effect of boundary absorption upon longitudinal dispersion in shear flows. J. Fluid Mech. 134: 161-177.

Soulsby, R.L., and J. D. Humphery. 1989. Field observations of wave-current interaction at the sea bed. In: Torum, A., Gudmestad, O.T. (eds), *Proceedings of NATO Advanced Research Workshop on Water Wave Kinematics*, Molde, Norway, 22-25 May 1989, Kluwer Academic Publishers, Dordrecht, Netherlands, 413-428.

Stacey, M.T., Burau, J., and S.G. Monismith. 2001. Creation of Residual flows in a partially stratified estuary. J. Geophys. Res. 106: 17013-37.

Stommel, H., and H.G. Farmer. 1952. On the nature of estuarine circulation. Woods Hole Oceanographic Technical Report 52-88.

Talke, S.A., and M.T. Stacey. 2003. The influence of oceanic swell on flows over an estuarine intertidal mudflat in San Francisco Bay. Estuarine Coastal and Shelf Science 58: 541-554.

Talke, S. 2005. An Investigation on the Hydrodynamics and Sediment Dynamics on an Intertidal Mudflat in Central San Francisco Bay. Ph.D. Thesis, 301 pp., University of California-Berkeley, Berkeley, California.

Talke, S.A., and M.T. Stacey. 2008. Suspended sediment fluxes at an intertidal flat: The shifting influence of wave, wind, tidal, and freshwater forcing. Continental Shelf Research [doi:10.1016/j.csr.2007.12.003].

Taylor, G.I. 1954. The dispersion of matter in turbulent flow through a pipe. Proc. R. Soc. London Ser. A 219: 186-203.

Uncles, R.J., Elliot, R.C.A., and S.A. Weston. 1985. Observed fluxes of water, salt, and suspended sediment in a partly mixed estuary. Estuarine Coastal and Shelf Science 20: 147-167.

Valle-Levinson, A., W.C. Boicourt, and M.R. Roman. 2003. On the linkages among density, flow, and bathymetry gradients at the entrance to the Chesapeake Bay. Estuaries 26: 1437-1449.

Walters, R. A. 1982. Low-frequency variations in sea level and currents in South San Francisco Bay. J. Phys. Oceanogr. 12: 658-668.

Wang, B., O.B. Fringer, S.N. Giddings, and D.A. Fong. 2009. High-resolution simulations of a macrotidal estuary using SUNTANS. Ocean Modelling 26: 60-85.

Wang, D.-P. 1979. Wind-driven circulation in the Chesapeake Bay, winter 1975. J. Phys. Oceanogr. 9: 564-572.

Wong, K.-C. 1994. On the nature of transverse variability in a coastal plain estuary. J. Geophys. Res. 99: 14209-14222.

Wiggins, S. 2005. The dynamical systems approach to Lagrangian transport in oceanic flows. Annu. Rev. Fluid Mech. 37: 295-328.

Zhong, L. and M. Li. 2006. Tidal energy fluxes and dissipation in the Chesapeake Bay. Cont. Shelf Res. 26: 752-770.

Zimmerman, J.T.F. 1976. Mixing and flushing of tidal embayments in the western Dustch Wadden Sea, II: analysis of mixing processes. Neth J. Sea Res. 10: 397-439.

Zimmerman, J.T.F. 1986. The tidal whirlpool: a review of horizontal dispersion by tidal and residual currents. Neth. J. Sea Res. 20: 133-54.

Appendix: Application of Single-Point Wave-Turbulence Decomposition Methods for Shallow Tidal Systems

A.1 Introduction

Calculating turbulent statistics from measured velocities is important for many applications which require estimates of mixing and transport. Two statistics that characterize turbulence are turbulent kinetic energy (TKE,) and Reynolds stresses, which are obtained from the variances and covariances, respectively, of the turbulent fluctuations in the *x, y, z* components of flow. Both quantities are fundamental to characterizing turbulent mixing and transport of scalars in environmental flows and have important applications such as implementing and evaluating turbulence closure in modeling.

However, calculating turbulent statistics in environmental flows is complicated by the presence of surface gravity waves (e.g. Trowbridge 1998, Shaw and Trowbridge 2001, Feddersen and Williams 2007). In the presence of surface waves, a measured signal x is composed of its mean value $\bar{x}$, fluctuations contributed by waves $\tilde{x}$, and fluctuations contributed by turbulence x', so that $x = \bar{x} + \tilde{x} + x'$. Because the frequencies of the wave fluctuations may overlap with those of the turbulent fluctuations, separating the wave fluctuations from the turbulent fluctuations in order to calculate turbulent statistics can be difficult. Using uncorrected data results in an overestimate of TKE, due to the extra energy in the wave fluctuations. Similarly, wave boundary layer processes or small uncertainties in instrument tilt produce spurious correlations between vertical and horizontal orbital velocities, i.e., in the turbulent Reynolds stresses (Shaw and Trowbridge 2001). Thus, wave-turbulence decomposition (WTD) is an important goal, and a number of methods are available to remove surface wave contamination from velocity data. In this study, we will focus on methods for removing surface waves from velocity data collected at a single point, such as that from acoustic Doppler velocimeters, or ADVs.

Various methods have been described and applied to remove wave contamination from turbulent statistics (e.g. Benilov et al. 1974, Agrawal and Aubrey 1992, Trowbridge 1998, Shaw and Trowbridge 2001, Bricker and Monismith 2007, Gerbi et al. 2008, Brand et al. 2010). Generally, the most accepted method of wave removal is the Shaw and Trowbridge 2001 (ST) method, which is a two-point method in which velocity data collected from a second "filter" sensor is used to remove surface wave contamination from velocity data collected from the original "target" sensor, thus requiring two velocity sensors in the vicinity of each point where calculation of turbulence statistics is desired (the method will be described in more detail later). In complex wave environments and/or near the water surface, however, the Shaw and

Trowbridge method can fail (Gerbi et al. 2008), and single-point methods become useful. Single-point methods are often also necessitated by experimental design or resource limitations. The various WTD methods for single-point velocity data each have advantages and disadvantages, depending on the measurement conditions, which can lead to some uncertainty as to which method to select as most appropriate and effective. The goal of this study is to characterize the effectiveness of these single-point WTD methods by comparing their performance under a variety of environmental conditions, in order to provide some guidance towards selecting the most appropriate method for removing surface wave contamination from velocity data.

A.2 Materials and Procedures

The methods examined in this study are meant to apply to high frequency time-series velocity data at a single point, such as velocity data collected by ADVs. In addition to this primary velocity data, additional supplementary data such as co-located pressure time-series or a second velocity time-series measurement may be used.

The effectiveness of various single-point methods for removing the surface wave contamination from turbulent statistics under varying conditions were tested and compared against the two-point ST method of linear wave filtration. The three single-point methods are the 'pressure' method, the 'interpolation method', and the 'phase' method. Wave-turbulence decomposition can be accomplished either through linear filtration in the time domain such as the ST and pressure method, or through spectral approaches such as the interpolation and phase method. Each of these methods will be described in the following sections.

A.2.1 Linear Filtration Methods

Shaw and Trowbridge (2001)

The Shaw and Trowbridge (2001) (ST) method uses a second velocity sensor to filter waves in velocity data from the primary sensor. It relies on the assumption that the spatial coherence scale of the wave-induced fluctuations in velocity are large in comparison to the turbulent fluctuations, which are assumed to be incoherent with each other. Thus in order for the method to effectively remove wave fluctuations but not turbulent fluctuations, the two velocity sensors must be in close enough proximity so that wave-induced fluctuations are well-correlated between both sensors, allowing them to be filtered, but they must also be separated beyond the turbulent correlation length, so that the largest turbulent eddies remain unfiltered. The filtration is linearly adaptive, allowing for wave removal even in the presence of temporal delay and changes in magnitude in the wave signal between sensors.

The wave induced signal at ADV 1, $\widetilde{x_1}\ (t)$, can be predicted by

$$\widetilde{x_1}(t) = \int_{-\infty}^{\infty} h(t')\, \widetilde{x_2}(t - t')dt' \qquad \text{(A.1)}$$

where $\widetilde{x_2}(t)$ is the signal at ADV 2, t is time and $h(t')$ is a filter which represents the relationship between the wave induced fluctuations at both locations. We can obtain a wave-free signal $\Delta x_1 = x_1 - \widehat{x_1}$ using

$$\widehat{x_1}(t) = \int_{-\infty}^{\infty} \hat{h}(t')\, x_2(t - t')dt' \qquad \text{(A.2)}$$

The estimates of the filter weights $\hat{h}(t')$ are determined by finding the least squares solution of the transversal filter model. More details of this calculation can be found in Shaw and Trowbridge (2001). Once the wave-free signals in horizontal and vertical velocity ($\Delta U_1(t)$ and $\Delta W_1(t)$) are obtained, these signals can be used to calculate turbulent quantities such as TKE components and Reynolds stresses, assuming that subtracting the filter $\widehat{x_1}$ effectively removes the wave signal $\widetilde{x_1}$ from x_1 while contributing a negligibly small amount of turbulent signal from ADV 2, $\delta x'_2$. The contribution of this term is greatly reduced in magnitude compared to the original turbulent signal from ADV 2 x'_2 because of the effects of the time-dependent linear filtration using $\hat{h}(t')$, which in theory passes only the correlated wave signal at ADV 1 predicted from velocity at ADV 2 (see Feddersen and Williams 2007).

Pressure Method

It is also possible to use similar techniques of linear filtration to remove wave contamination using measured pressure data as a proxy for surface wave fluctuations instead of velocity (e.g. Benilov et al. 1974, Kitaigorodskii et al. 1983, Agrawal and Aubrey 1992). We used a linear adaptive filtration method similar to the one used in Shaw and Trowbridge (2001), rather than removing wave energy in the spectral domain as is usually done (e.g. Benilov et al. 1974). This allows for a more direct comparison between the effectiveness of using velocity and pressure data as filters for wave fluctuations.

A.2.2 Spectral Methods

Interpolation Method

Another approach is to use spectral methods to define and separate the wave and turbulent portions of the velocity autospectra and cospectra in order to calculate TKE components and Reynolds stresses (e.g. $\overline{u'^2}$, $\overline{w'^2}$, $\overline{u'w'}$). The presence of wave fluctuations often appears in the velocity spectra as one or several wave peaks which fall within the same spectral frequencies as the inertial subrange of turbulence (Bricker and Monismith, 2007). Thus one method of wave removal is to use a linear interpolation in order to remove the wave peak from the power spectral density (PSD) which represents the energy spectra of each velocity component (Soulsby & Humphery 1989). The remaining velocity autospectra are integrated to calculate turbulent velocity variances (TKE components, $\overline{u'^2}$ and $\overline{w'^2}$ for horizontal and vertical velocity, respectively). The interpolation method relies on an energy spectrum containing both a well-defined wave peak or peaks and a well-defined inertial subrange of the turbulent energy

spectrum with a constant slope, theoretically -5/3 from dimensional considerations following the frozen turbulence hypothesis (Taylor 1938). A potential limitation of this method is that turbulent energy is aliased into the wave peak (see Lumley & Terray, 1983) and is removed, possibly causing an underestimation of TKE.

The interpolation method can be applied to estimate wave contamination of the Reynolds stress $\overline{u'w'}$, which can be calculated by integrating the cross-spectral density (CSD) $Co_{u'w'}(f)$ produced from the cospectra of the turbulent velocity components in the horizontal (u) and vertical (w) directions. The turbulent Reynolds stress can thus be found by removing the wave contribution $\overline{\tilde{u}\tilde{w}} = \int Co_{\tilde{u}\tilde{w}}(f)df$ from $\overline{uw}$, the raw estimate of the Reynolds stress, assuming negligible wave-turbulence interaction (Bricker and Monismith 2007). To accomplish this, first the raw estimate of the Reynolds stress is calculated by integrating the raw CSD ($\overline{uw} = \int Co_{uw}(f)df$). Then for each velocity component the autospectral PSD is obtained, e.g. for $u(t)$, $S_{uu_j}(f_j) = \frac{1}{d\omega}|U_j|^2$, where $U_j = U(f_j)$ is the Fourier transform of $u(t)$ at frequency f_j and t is time. The magnitudes of the spectral wave fluctuations $|\widetilde{U_j}|$ and $|\widetilde{W_j}|$ are found by taking the square root of the magnitude of the spectral wave energy $|\widetilde{U_j}|^2$ removed from S_{uu_j} and S_{ww_j} by interpolation across the wave peak. These magnitudes are used to estimate the wave contributions to the raw CSD for each frequency, $\widetilde{U_j} * \widetilde{W_j}$, which is equal to $|\widetilde{U_j}||\widetilde{W_j}|$ if the two velocity components are assumed to be perfectly in phase (the validity of this assumption will be discussed in further detail later). Summing the wave contributions yields the total wave contamination $\overline{\tilde{u}\tilde{w}} = \sum_j \widetilde{U_j} * \widetilde{W_j}$, or using the perfect correlation assumption, $\overline{\tilde{u}\tilde{w}} = \sum_j |\widetilde{U_j}||\widetilde{W_j}|$. This value is subtracted from the Reynolds stress estimated from integrating the raw CSD to yield the corrected estimate for the Reynolds stress, $\overline{u'w'} = \overline{uw} - \overline{\tilde{u}\tilde{w}}$.

Phase Method from Bricker and Monismith (2007)

The phase method from Bricker and Monismith (2007) is a modification of the interpolation method for calculating turbulent Reynolds stress which avoids the assumption of perfect correlation or synchronous phasing of wave fluctuations. When the Fourier coefficients are written in phasor notation as $U_j = |U_j|e^{i\angle U_j}$, the phase is $\angle U_j = \arctan\left[\frac{\mathrm{Im}(U_j)}{\mathrm{Re}(U_j)}\right]$. Each spectral component of the CSD $Co_{uw_j}(f_j)$ is then $U_j * W_j = |U_j||W_j|e^{i(\angle W_j - \angle U_j)}$, or using the Euler relation, $U_j * W_j = |U_j||W_j|[\cos(\angle W_j - \angle U_j) + i\sin(\angle W_j - \angle U_j)]$, where only the real part contributes when summing over the double-sided spectrum. The phase method relies on the assumption that surface waves dominate the velocity field at the wave frequencies. Hence, the observed spectral phases of the horizontal and vertical components of velocity are assumed to be $\angle U_j$ and $\angle W_j$, even in the presence of turbulent fluctuations. Therefore, summing over the real portion, Bricker and Monismith estimate wave stress as $\overline{\tilde{u}\tilde{w}} = \sum_j \widetilde{U_j} * \widetilde{W_j} = \sum_j |\widetilde{U_j}||\widetilde{W_j}|cos(\angle W_j - \square U_j)$, where $|\widetilde{U_j}|$ and $|\widetilde{W_j}||$ are found by interpolation over the spectral peak and the phases are found from the Fourier coefficients. When the

horizontal and vertical phases at a frequency *f* are 90 degrees out of phase, the wave stress contribution becomes negligible.

A.3 Assessment

A.3.1 Field Data for Experimental Method Comparison

The methods were applied to data collected from two field sites in San Francisco Bay, one in South San Francisco Bay and one at the Richmond Field Station (RFS), on the northeast shore of Central San Francisco Bay. San Francisco Bay is a shallow estuarine system forced by mixed semi-diurnal/diurnal tides and wind. The velocity data collected from the two field sites provided significantly different environments within which to test the effectiveness of the wave removal methods. Data from the South Bay were collected from instruments moored at stations located on the broad shoals of the southern end of the bay (Figure A.1) (Brand et al. 2010). The South Bay is strongly tidally forced, with currents around 0.4 m/s at our stations, resulting in a well-developed turbulent velocity field. Strong, sustained winds during afternoons or storm events result in a relatively well-defined wave field consisting of waves with periods of 2-3 seconds and waves heights up to the range of 1 m. Data from Richmond Field Station were collected from instruments located on an intertidal mud flat located in central San Francisco Bay (Talke et al. 2008). The tidal currents are much smaller than in the South Bay, generally reaching a maximum of about 0.1 m/s, resulting in weaker, less-developed turbulence. The location of the RFS site in central San Francisco Bay results in the presence of ocean swells of periods ranging from 6-20 s and magnitudes up to 0.1 m, along with locally forced wind waves with periods of about 1-4 s and magnitudes up to 0.3 m (Talke & Stacey, 2003). Details on the data collection in the two sites are contained in the following sections.

South San Francisco Bay Data Collection

The South Bay data were collected from a study conducted in South San Francisco Bay (Brand et al. 2010) at a shallow water site south of the San Mateo Bridge on the eastern edge of the deep channel that bisects the Bay (Fig. A.1). The South Bay is characterized by two broad shoals (each 2-4 meters deep) which are divided by a deep channel (approximately 14 m MLLW). Two instrument platforms were deployed as part of a larger-scale study of transport in the shallow waters of the South Bay (Fig. A.1) from 02/24/2009 to 03/16/2009 (spring) and from 09/09/2009 to 10/07/2009 (fall). The stations were deployed on a line perpendicular to the channel at locations 1000 and 2000 m distant from the middle of the channel. The station closer to the shore (Lon: 122.20977, Lat: 37.58633, elevation 2.19 m MLLW) will be referred to as the benthic station. Two 10 MHz ADVs (Sontek Hydra) recorded 8 minute bursts at 10 Hz every 12 minutes at 0.36 and 0.72 m above the bottom. The station closer to the channel (Lon: 122.21622, Lat: 37.57788, elevation 2.59 m MLLW), called the shoal station, was equipped with two ADVs. A 10 MHz ADV (Sontek Hydra) was mounted 0.25 m above the bed and a 6 MHz ADV (Nortek Vector) was mounted 0.50 m above the bed. Both ADVs recorded 10 minute bursts at 8 Hz every 60 minutes.

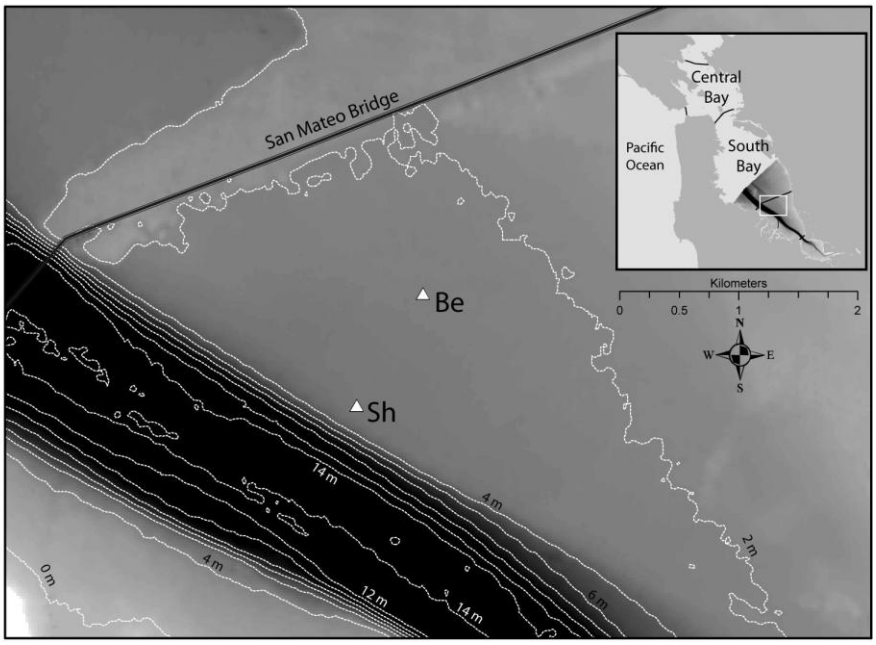

Figure A.1: Location of South Bay study site and field stations. Shoal Station at 2.59 m MLLW elevation closer to the channel, Benthic Station closer to the shore at 2.19 m MLLW elevation. Reprinted from Brand et al. 2010.

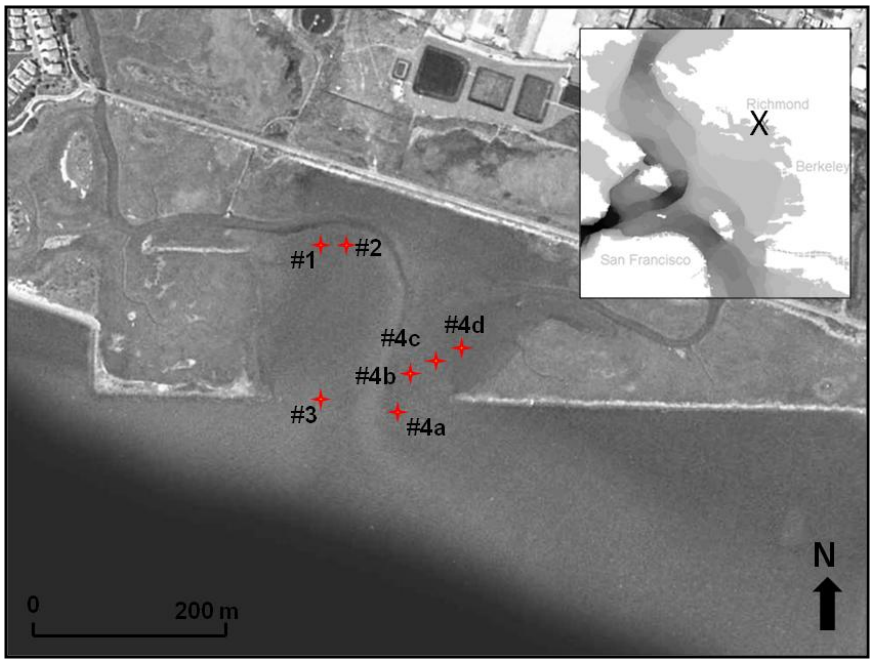

Figure A.2: Location of Richmond Field Station study site. Location of RFS site within inset map of central San Francisco Bay marked with an 'X'. Data for this study was taken from experiment site #3.

Richmond Field Station Data Collection

Intertidal velocity and pressure data from the central San Francisco Bay (Figure A.2) in Richmond, CA (37^0 54' 27.9'' N, 122^0 20' 2.0'' W) was obtained between April 11th and April 15th, 2003, (see also Talke & Stacey, 2008). We refer to this data as the Richmond Field Station (RFS) data set. Six velocimeters were deployed on an aluminum frame at heights of 2 cm, 5 cm, 10 cm, 15.5 cm, 28.5 cm, and 33 cm above the bed. The instruments at 10 cm and 33 cm were mounted in a sideward looking configuration; the others were oriented vertically. Three-component flow velocity was measured at frequencies of 8-16 Hz over burst lengths of 180 to 590 seconds, repeated every 600 seconds. Each instrument also measured pressure in the instrument body, with an effective frequency resolution of about 1 Hz due to sensor limitations.

A.3.2 Spectral and Cospectral Comparisons

To examine the efficacy of the different WTD methods over a burst, we compared both velocity spectra and cospectra before and after application of each wave removal technique. In particular, the integrated cospectrum of u and w (horizontal and vertical velocity, respectively) was examined for wave removal efficiency. This curve, known as an ogive curve, is produced by cumulatively integrating the cospectrum Co_{uw}, which we will do starting from the highest frequencies such that $Og_{uw}(f) = \int_f^\infty Co_{uw}(f')\,df'$. The ogives are used because they provide a clearer visualization of the effectiveness of wave removal in the spectral Reynolds stress calculation than directly looking at cospectra, which are often noisy (e.g. Figure A.3)

As an initial comparison of the effectiveness of each of the WTD methods, the methods were applied to remove waves from a single wave-influenced burst collected in the South Bay shoal station during spring at 50 cm above the bed (mean velocity 32.8 cm/s). For the second sensor in the Shaw and Trowbridge method, we used the sensor at 25 cm height. To compare methods under different environmental conditions, we also applied WTD to an ADV burst collected from Richmond Field Station at 33 cm above the bed at 8 Hz over a period of about 3 minutes (mean velocity 10.5 cm/s). A similar burst at 10 cm above the bed provided the second measurement required by the Shaw and Trowbridge method. The bursts were chosen to be representative of periods in which WTD methods would be most necessary due to significant wave contamination. In such periods, errors due to wave contamination would be largest and thus easiest to measure. Before application of the methods, velocity data from each burst were rotated into horizontal, lateral, and vertical velocities u, v, and w (see Lee et al. 2004), and the data were linearly detrended. Plots of horizontal and vertical velocity autospectra, cospectra, and ogives were produced for each method in both environments, with each plot including "raw" or uncorrected data, "filtered" data which shows wave energy or stress removed, and final "corrected" data after wave removal. The results for each case are discussed below.

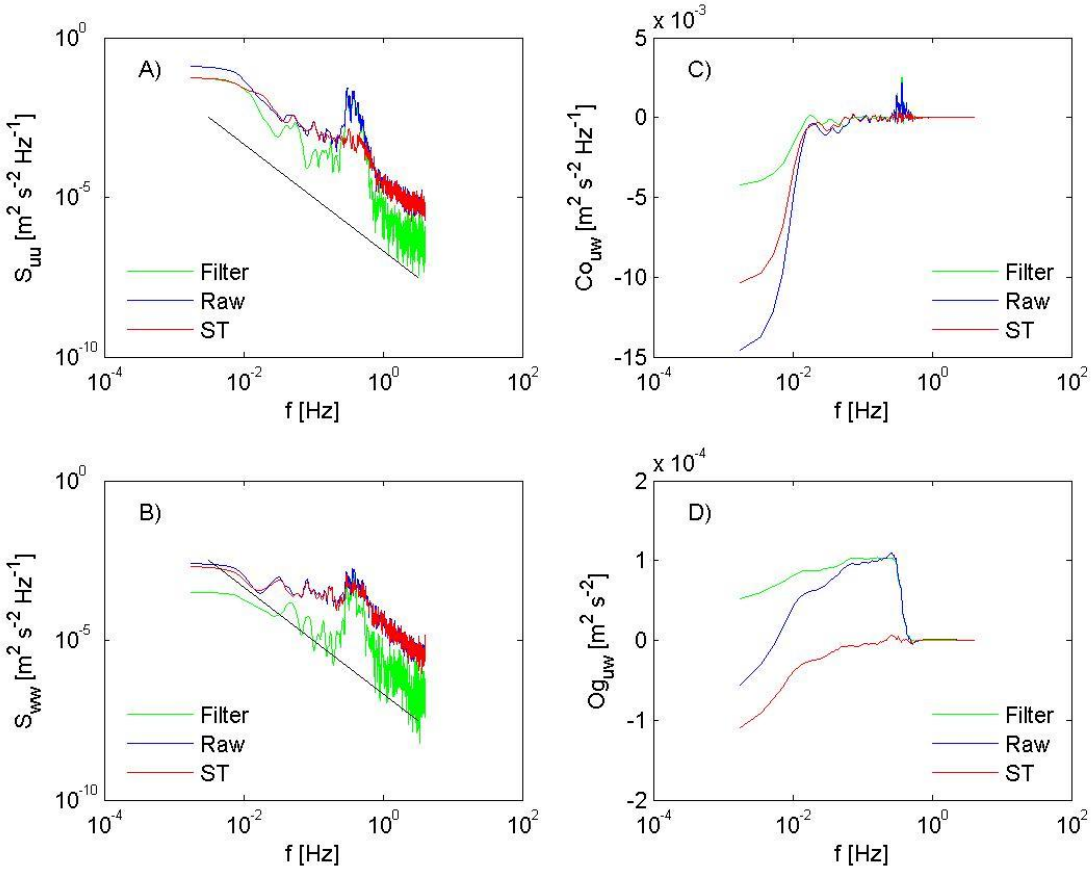

Figure A.3: Results for South Bay burst using the Shaw and Trowbridge (ST) method. Subplots show A) velocity autospectra for horizontal velocity (u), B) velocity autospectra for vertical velocity (w), C) cospectrum of u and w, and D) integrated cospectrum (ogive) of u and w. Raw data shown in blue (Raw), wave energy or stress removed shown in green (Filter), and corrected data shown in red (ST). On autospectral plots, solid black line shows predicted -5/3 slope for the inertial subrange of turbulence for comparison.

Shaw and Trowbridge (2001)

For the Shaw and Trowbridge (ST) method, qualitative examination of the velocity spectra for *u* and *w* at both sites (Figures A.3 and A.4) show that for both bursts the method is able to remove most of the wave peak for *u*, but is less successful in removing the wave peak in *w*. There could be several reasons for this, from environmental variability in the wave field (discussed further in a later section) or simply difficulties resulting from the smaller magnitudes of the wave fluctuations in *w* compared to *u* in near-bed environments.

The wave peak results in elevated correlation between *u* and *w* in the wave frequencies, and this is reflected in ogive curves as a discontinuity (jump) in the integrated cospectrum at the wave peak. These jumps are observed in the ogive curves for the raw, uncorrected data, with

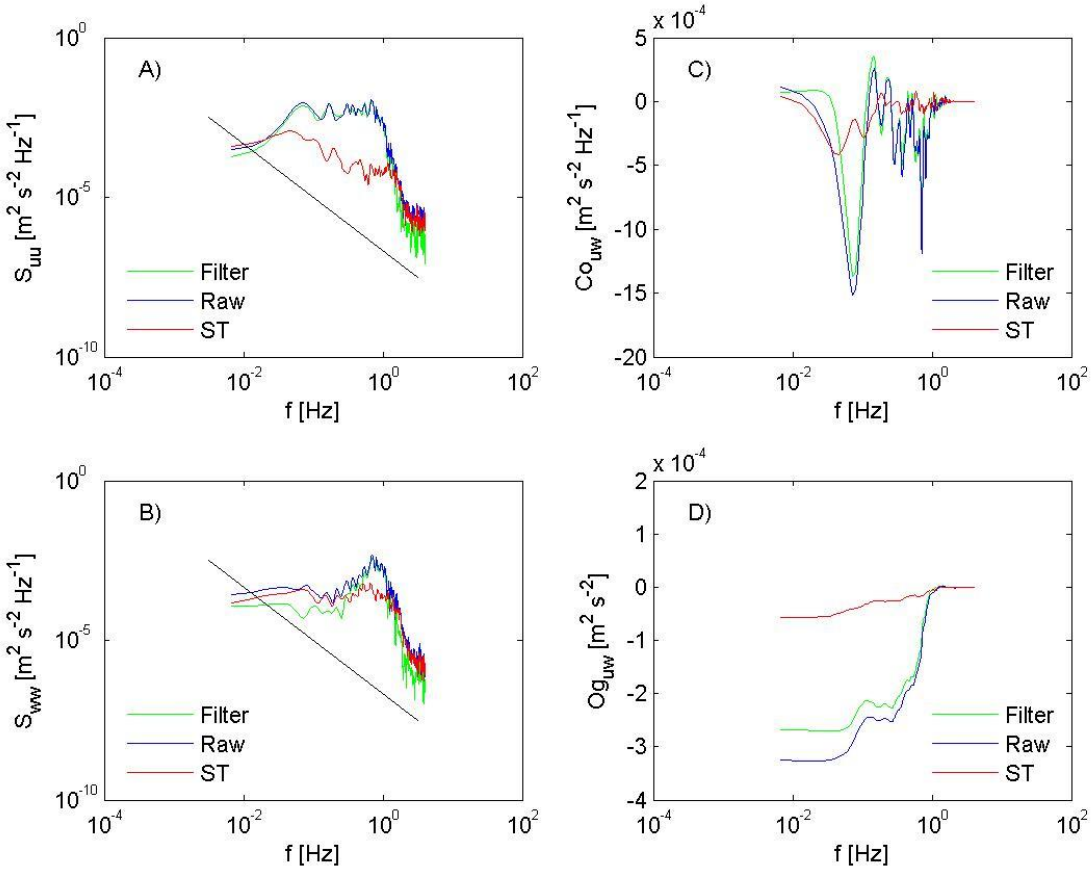

Figure A.4: Results for RFS burst using the Shaw and Trowbridge (ST) method. Subplots show A) velocity autospectra for horizontal velocity (u), B) velocity autospectra for vertical velocity (w), C) cospectrum of u and w, and D) integrated cospectrum (ogive) of u and w. Raw data shown in blue (Raw), wave energy or stress removed shown in green (Filter), and corrected data shown in red (ST). On autospectral plots, solid black line shows predicted -5/3 slope for the inertial subrange of turbulence for comparison.

wave peaks occurring at frequencies of about 0.3-0.5 Hz for the South Bay (Fig. A.3) and two main wave peaks in the RFS data at frequencies of about 0.05-0.15 Hz and 0.2-1.0 Hz (Fig. A.4), corresponding to ocean swell and local wind waves respectively (see Talke & Stacey, 2003). The discontinuities in the ogives occur in either the positive or negative direction depending on the sign of the wave contamination, a product of the relative phases of the observed wave components (the South Bay burst shows positive wave contributions, while the RFS burst shows negative wave contributions). In theory, removing wave contributions to the ogive should result in a smooth curve representing the scale-dependent distribution of turbulent stresses (such as those measured by Kaimal, 1972). The ogives are thus useful as visual indicators of wave removal behavior because they show integrated correlation as a function of frequency, as well as

the total correlation (the low frequency limit represents the integrated value over the entire frequency range). The "filtered" ogive shows the total (integrated) amount of wave correlation removed as a function of frequency, and its low frequency limit provides an estimate of the total wave removal from the Reynolds stress calculation. From the ogives, we observe that the ST method removes most of the wave jump, resulting in a much smoother ogive curve (Fig. A.3D).

Without an independent measure of TKE or Reynolds stress, it is difficult to absolutely quantify how well each method performs in removing wave contamination from velocity data. The ST method, which we use as our benchmark, cannot be assumed to perfectly separate wave energy and turbulence. For example, we note that the ST method removes large-scale, low-frequency variations in both the spectra for *u* and the ogive curves of the South Bay (Fig. A.3). These low frequency scales, which may dominate the turbulent spectra and cospectra, are outside of the main wave peak. The low frequency content is removed because their scale is much larger than the separation distance between the two filtering sensors. Hence, application of the ST differencing method removes low-frequency, possibly turbulent motions. Other errors are introduced when the length scale of waves become decorrelated over the separation distance of the velocity measurement pair. This may particularly affect high frequency waves in the shallow intertidal site (RFS) when water depths are less than 0.5-1 m.

If the ST method were assumed to be perfect or near-perfect in wave removal efficiency, it could be used to quantitatively measure the performance of the single-point WTD methods. However, on a burst-by-burst basis the errors in wave removal can be large enough so that using the ST estimate as an absolute measure of wave removal efficiency for the other methods may be misleading. Hence we will rely here on qualitative examinations of different methods on an individual burst basis. Despite this, we find that the ST method provides reasonably accurate estimates of turbulent statistics, and can still be used as a benchmark for assessing the wave removal efficiency of WTD methods (this will be validated at the end of the assessment section).

Pressure Method

Examination of the spectra and ogive plots for the pressure method applied to the South Bay burst show that the method is quite effective in removing wave contamination (Figure A.5). In fact, the method appears to perform better in certain aspects than the ST method, such as removing more of the vertical wave spectra because pressure is well-correlated with vertical motions (Agrawal and Aubrey 1992, Herbers and Guza 1993). Similarly, the pressure method avoids removing non-wave fluctuations at lower frequencies. This establishes the pressure method as a viable single-point alternative to the Shaw and Trowbridge method for wave-turbulence decomposition.

The results for the RFS burst also show quite good results for wave removal, especially for the ogive plot (Figure A.6). The velocity spectra show better wave removal in *w* but worse wave removal in *u* as compared to Shaw and Trowbridge. The spectrum for *w* does not show a well-defined turbulent inertial subrange, but this can most likely be attributed to the strong domination of wave energy over turbulent energy at this site, especially for the vertical velocity. Further, the

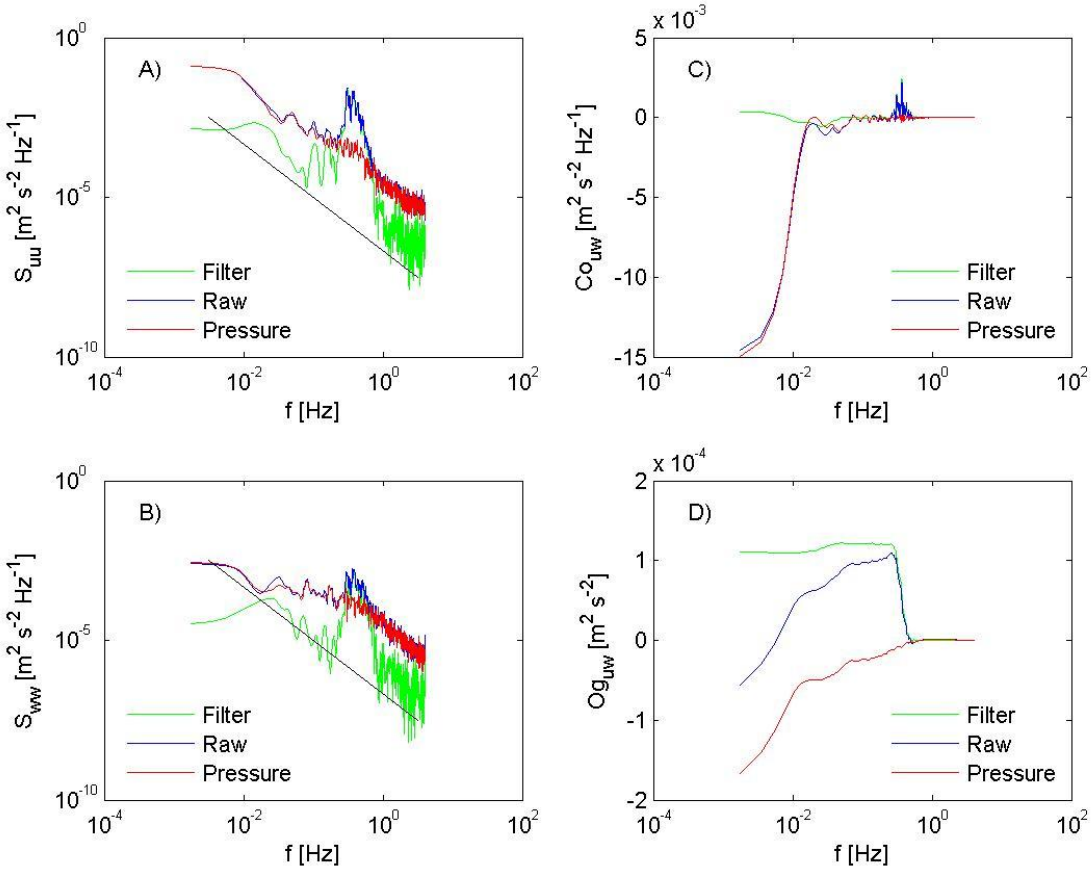

Figure A.5: Results for South Bay burst using the pressure method. Subplots show A) velocity autospectra for horizontal velocity (u), B) velocity autospectra for vertical velocity (w), C) cospectrum of u and w, and D) integrated cospectrum (ogive) of u and w. Raw data shown in blue (Raw), wave energy or stress removed shown in green (Filter), and corrected data shown in red (Pressure). On autospectral plots, solid black line shows predicted -5/3 slope for the inertial subrange of turbulence for comparison.

orientation of the instruments in the sideways looking direction reduces the resolution of the vertical component (compared to the South Bay measurements).

Spectral Methods: Interpolation and Phase Method

The spectral methods rely on directly modifying the spectra by interpolating the turbulent spectrum across the wave peak (Figures A.7-A.10). It is straightforward to remove wave energy from the South Bay burst (Figs. A.7 and A.9), since the wave peak and turbulent inertial subrange are well-defined. Identifying the wave peak and interpolating across a theoretical turbulent inertial subrange is more problematic and ambiguous in the RFS burst spectra (Figs. A.8 and A.10). Because the turbulent subrange could not be resolved past the lower frequencies

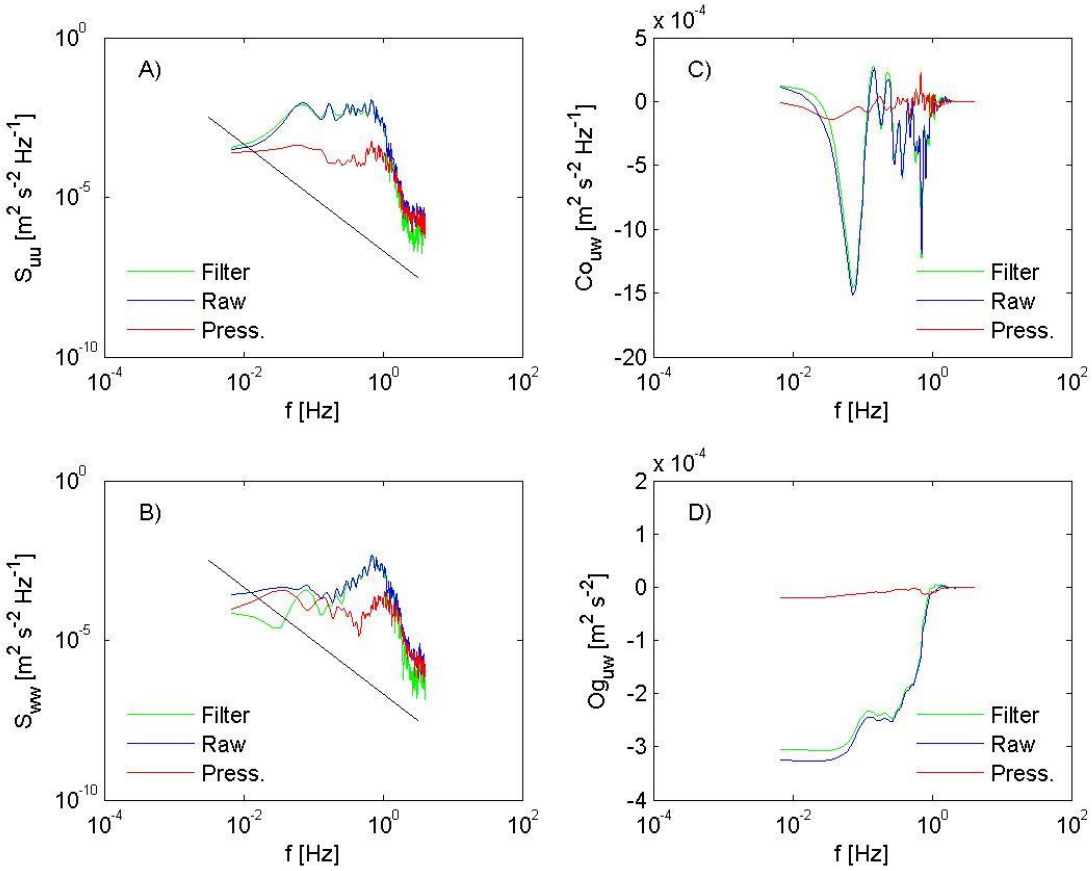

Figure A.6: Results for RFS burst using the pressure method. Subplots show A) velocity autospectra for horizontal velocity (u), B) velocity autospectra for vertical velocity (w), C) cospectrum of u and w, and D) integrated cospectrum (ogive) of u and w. Raw data shown in blue (Raw), wave energy or stress removed shown in green (Filter), and corrected data shown in red (Press.). On autospectral plots, solid black line shows predicted -5/3 slope for the inertial subrange of turbulence for comparison.

of the waves, the interpolations in Figs. A.8 and A.10 are less well-constrained than Figs. A.7 and A.9.

Interpolation is thus a fairly straightforward method of removing wave energy in calculating TKE statistics, provided that the turbulent energy can be effectively interpolated under the wave peak. A more interesting test of the spectral methods' effectiveness comes from examination of the ogive curves. Examination of the ogives for both bursts after application of the phase method shows that, although much of the wave contamination has been removed (Figs. A.9D and A.10D), a significant portion still remains compared to the linear filtration methods (Figs. A.3D-A.6D). Since the spectral plots show that the magnitudes of the wave peaks are reasonably estimated through direct interpolation (at least for the South Bay spectra), we conclude that

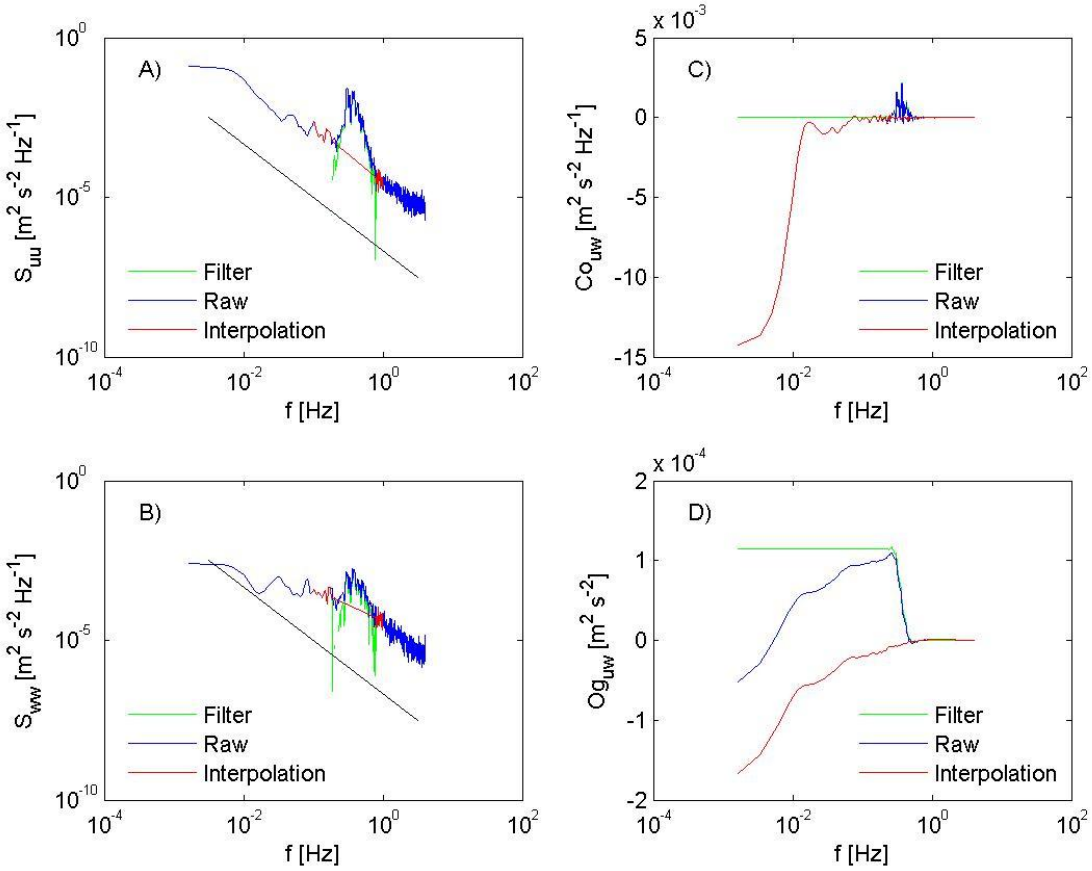

Figure A.7: Results for South Bay burst using the interpolation method. Subplots show A) velocity autospectra for horizontal velocity (u), B) velocity autospectra for vertical velocity (w), C) cospectrum of u and w, and D) integrated cospectrum (ogive) of u and w. Raw data shown in blue (Raw), wave energy or stress removed shown in green (Filter), and corrected data (including both interpolation under wave peak and raw data points used for linear interpolation) shown in red (Interpolation). On autospectral plots, solid black line shows predicted -5/3 slope for the inertial subrange of turbulence for comparison.

inaccuracy must be introduced through the phase correction factor. We note that the simple interpolation (Figs. A.7D and A.8D) performs much better in removing the wave contamination in the ogive than interpolation with phase correction (Figs. A.9D and A.10D), despite assuming perfect correlation between vertical and horizontal motions. However, the simple interpolation produces an estimate of $\widetilde{\tilde{u}}\widetilde{\tilde{w}}$ that slightly exceeds $\overline{uw}$, resulting in a greater jump (discontinuity) at the wave frequency than the raw ogive (Figs. A.7D and A.8D).

The success of the interpolation method implies that under the conditions of both datasets, which were both collected in shallow environments and fairly close to the bed, wave fluctuations in *u* and *w* are close to being perfectly correlated. This occurs perhaps because wave orbital

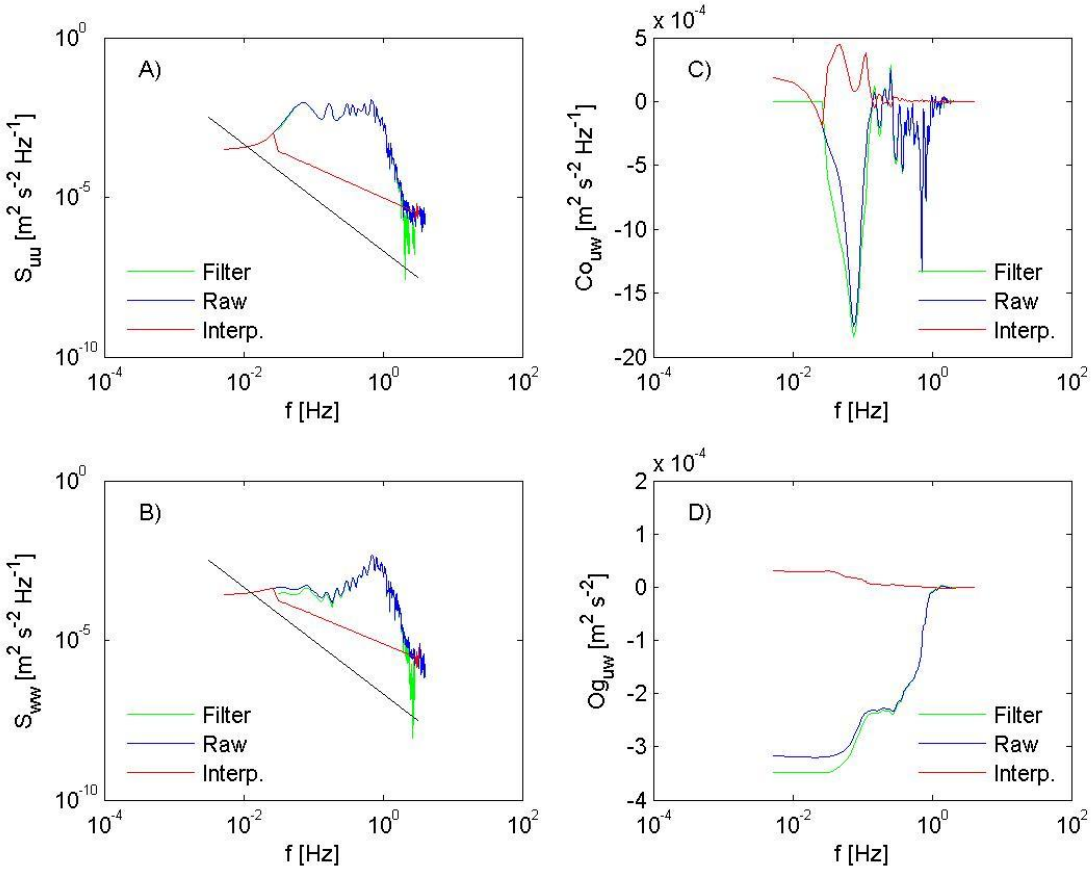

Figure A.8: Results for RFS burst using the interpolation method. Subplots show A) velocity autospectra for horizontal velocity (u), B) velocity autospectra for vertical velocity (w), C) cospectrum of u and w, and D) integrated cospectrum (ogive) of u and w. Raw data shown in blue (Raw), wave energy or stress removed shown in green (Filter), and corrected data (including both interpolation under wave peak and raw data points used for linear interpolation) shown in red (Interp.). On autospectral plots, solid black line shows predicted -5/3 slope for the inertial subrange of turbulence for comparison.

motions take the form of ellipses which progressively flatten near the bed. Although the ellipses are symmetric and thus $\overline{\tilde{u}\tilde{w}}$ would be zero in potential flow, the presence of instrument tilt and the effect of boundaries (e.g., wave boundary layer effects) produces wave contributions in $\overline{uw} = \overline{\tilde{u}\tilde{w}} + \overline{u'w'}$. The observed horizontal and vertical wave velocities $\tilde{u}_o$ and $\tilde{w}_o$ are functions of instrument tilt θ as well as the real vertical and horizontal velocities induced by wave orbital motions $\tilde{u}_r$ and $\tilde{w}_r$, such that $\tilde{u}_o = \tilde{u}_r \cos\theta + \tilde{w}_r \sin\theta$ and $\tilde{w}_o = \tilde{w}_r \cos\theta + \tilde{u}_r \sin\theta$. Because wave velocities are often much larger than turbulent velocities, even small instrument tilt, which in practice is often unable to be corrected to more than 1 or 2 degree accuracy, can cause significant wave contamination $\overline{\tilde{u}_o\tilde{w}_o}$ of the Reynolds stress calculation (Shaw and

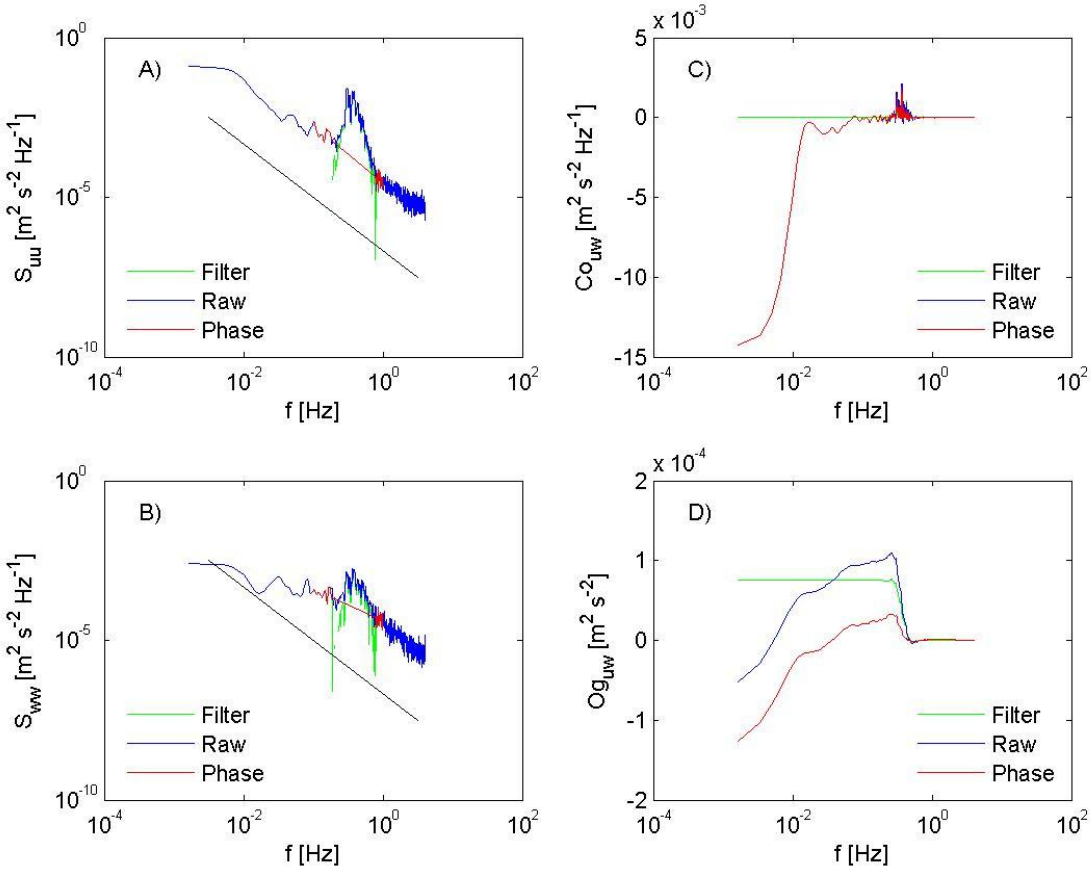

Figure A.9: Results for South Bay burst using the phase method. Subplots show A) velocity autospectra for horizontal velocity (u), B) velocity autospectra for vertical velocity (w), C) cospectrum of u and w, and D) integrated cospectrum (ogive) of u and w. Raw data shown in blue (Raw), wave energy or stress removed shown in green (Filter), and corrected data (including both interpolation under wave peak and raw data points used for linear interpolation) shown in red (Phase). On autospectral plots, solid black line shows predicted -5/3 slope for the inertial subrange of turbulence for comparison.

Trowbridge 2001). In the case of very flat, near-bed wave orbital motions with small or irregular $\tilde{w}_r$ both $\tilde{u}_o$ and $\tilde{w}_o$ would be largely dependent on $\tilde{u}_r$ and thus nearly in phase. This explains the effectiveness of the interpolation method's assumption of near perfect correlation in removing wave contributions to the cospectrum. By extension, the interpolation method will become more inaccurate for less flattened orbital motions (i.e., further from the bed).

We next examine why the phase method fails at completely removing the wave contributions. In Bricker (2007), the phase method was found to work well in the laboratory, but performed less effectively in field conditions (measured in the shoals of South San Francisco Bay). This conclusion is consistent with our field test of the method. By definition, spectral

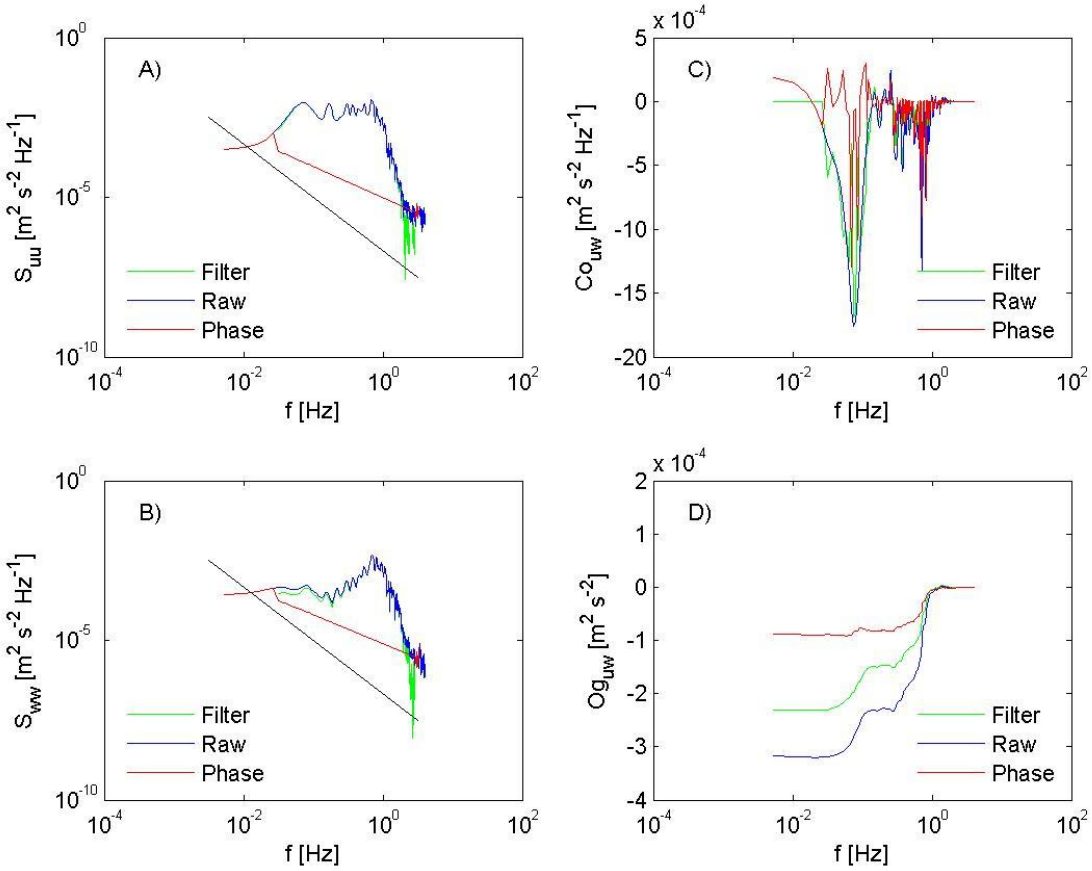

Figure A.10: Results for RFS burst using the phase method. Subplots show A) velocity autospectra for horizontal velocity (u), B) velocity autospectra for vertical velocity (w), C) cospectrum of u and w, and D) integrated cospectrum (ogive) of u and w. Raw data shown in blue (Raw), wave energy or stress removed shown in green (Filter), and corrected data (including both interpolation under wave peak and raw data points used for linear interpolation) shown in red (Phase). On autospectral plots, solid black line shows predicted -5/3 slope for the inertial subrange of turbulence for comparison.

methods only estimate an average power (magnitude) and phase at each frequency. Hence, error may be introduced for conditions in which magnitude and phase varies significantly over the time period of calculation. Phase variation may occur when a wave field at a given frequency is sourced from different processes, e.g., contains components due wind-waves, reflected waves, non-linear harmonics, and/or time-varying Doppler shifts. Variations in magnitude produce phase shifts in the linear combination of these waves. Directional spreading may also introduce error.

Because the only difference between the interpolation and phase methods is in the calculation of the phase correction factor, the sensitivity of the phase method to environmental conditions

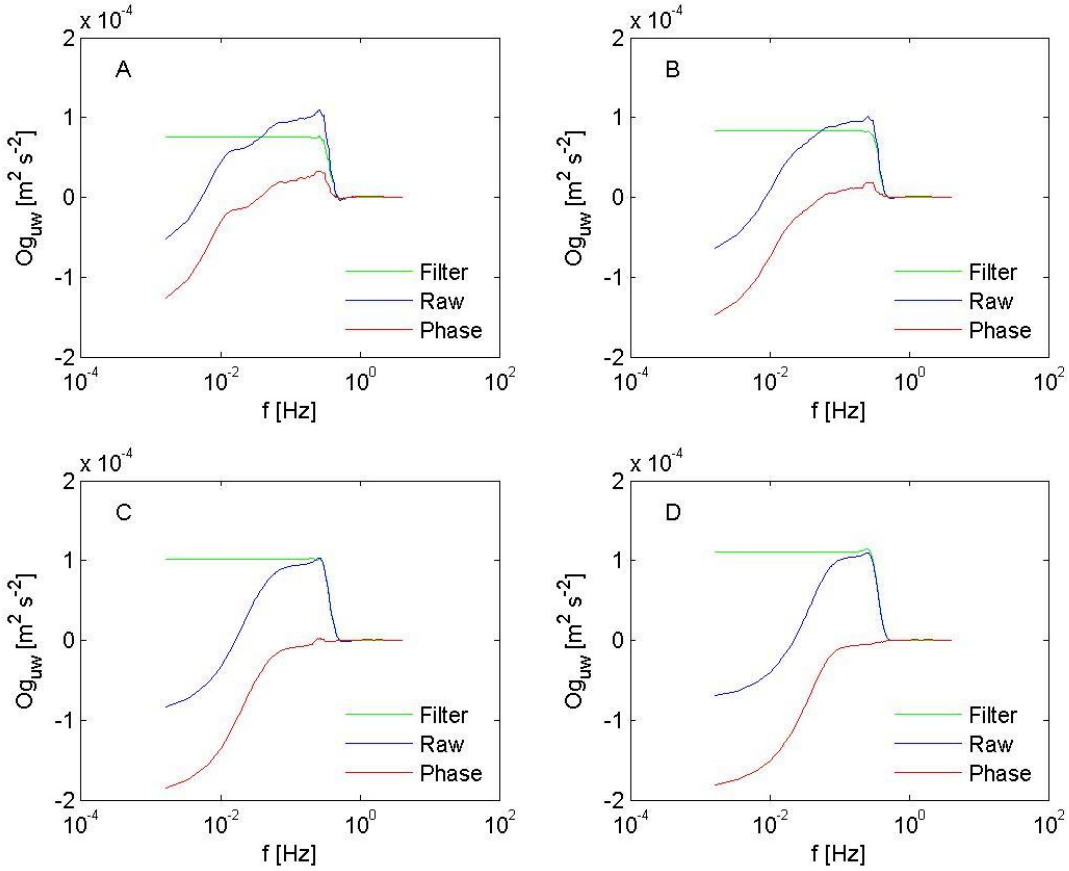

Figure A.11: Results for South Bay burst using the phase method. Integrated cospectra (ogives) of u and w are shown, with results for various numbers and length of the Hamming averaging windows in Welch's method for calculating PSDs. The subplots show A) n = 4.5, B) n = 9, C) n = 18, and D) n = 36, where n is the number of averaging windows used, hence higher n also corresponds to shorter window length.

must come from this calculation. The accurate calculation of a wave phase requires a regular, nearly constant wave field that is resolved using techniques such as Welch's method for calculating PSDs. One aspect of this calculation that was explored was the number (*n*) and length of the Hamming averaging windows that were used in Welch's method as used in MATLAB (Figures A.11 and A.12). The effectiveness of the phase method can be qualitatively assessed by observing removal of the wave jump in the "raw" ogive, with total wave removal shown by the "filter" ogive. The results show that the effectiveness of the estimated phase correction factor depends on the relationship between variability in wave phasing over the length of the burst and the number and length of averaging windows for phase calculation. By decreasing the averaging window length (by increasing *n*), more wave energy is removed from

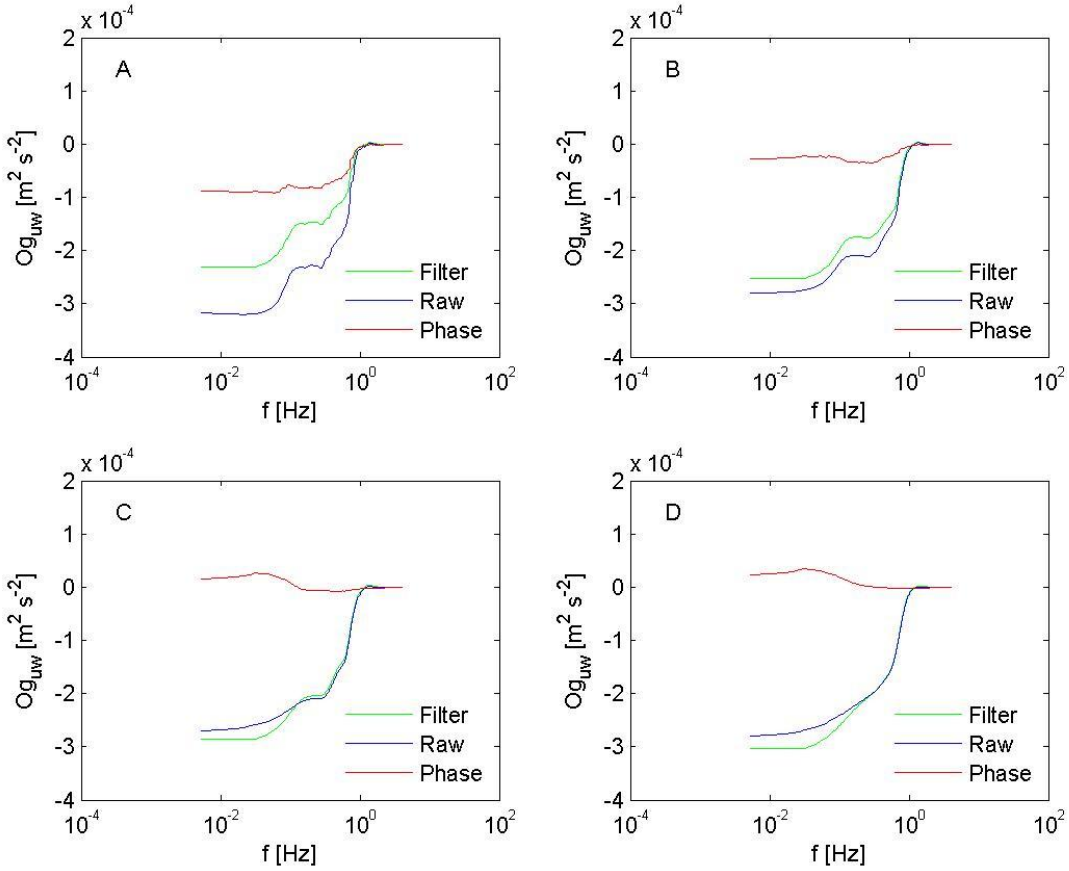

Figure A.12: Results for RFS burst using the phase method. Integrated cospectra (ogives) of u and w are shown, with results for various numbers and length of the Hamming averaging windows in Welch's method for calculating PSDs. The subplots show A) n = 4.5, B) n = 9, C) n = 18, and D) n = 36, where n is the number of averaging windows used, hence higher n also corresponds to shorter window length.

the ogive curve. Hence the phase correction error can be mitigated in variable environmental conditions, though at the cost of decreased resolution at lower frequencies.

A.3.3 Ogive Comparisons of Wave Removal from Reynolds Stress Calculations

The ogive curves before and after application of the four methods to the South Bay burst were plotted together to directly compare their removal of wave contamination in Reynolds stress calculations (Figure A.13). The Reynolds stress estimate for each method can be evaluated by comparing the values of the ogives at the low frequency limit (left-hand side) of the plot, representing the total integration of the corrected cospectra. Differences between the methods can be clearly seen: for example, the Shaw and Trowbridge method underestimates

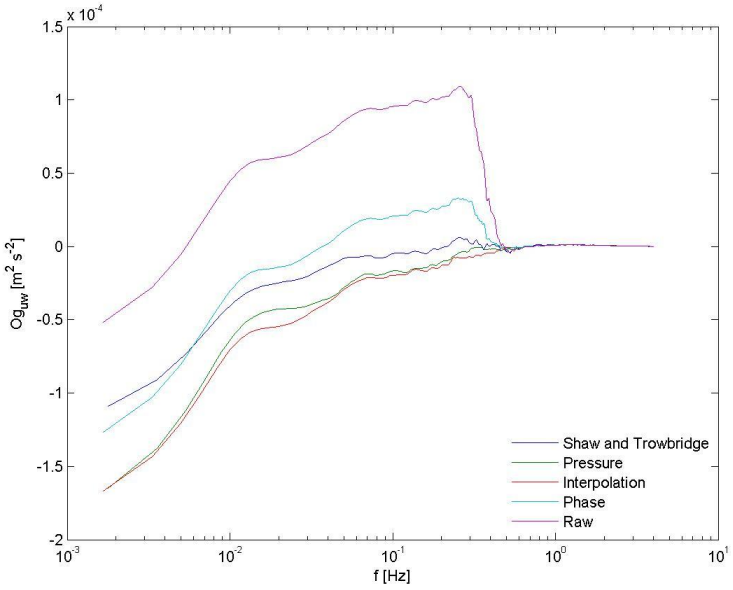

Figure A.13: Ogive comparison of methods applied to South Bay burst for cospectrum of horizontal and vertical velocity u and w. Both corrected data for each method and uncorrected (Raw) data shown.

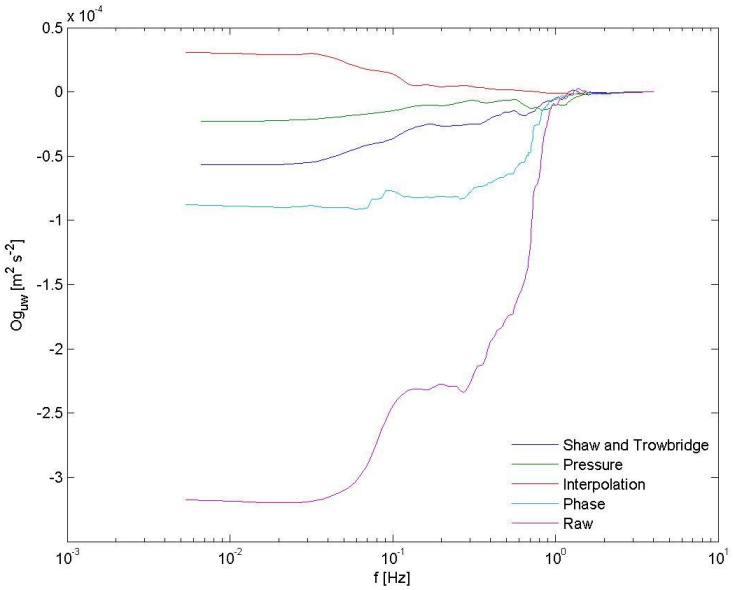

Figure A.14: Ogive comparison of methods applied to RFS burst for cospectrum of horizontal and vertical velocity u and w. Both corrected data for each method and uncorrected (Raw) data shown.

Reynolds stress by removing turbulence at low frequencies while the phase method only incompletely removes wave energy.

The comparison for the RFS site shows similar results (Figure A.14), except that for this burst the pressure method gives a smaller estimate of the Reynolds stress than the Shaw and Trowbridge method, though both are small relative to the wave contamination; this is typical for this site. Evaluating the ogives for the spectral methods (interpolation and phase), we note that even though coarsely constrained interpolation was used, these methods remove the same order of magnitude wave energy as the linear filtration methods. A probable explanation is that wave energy dominates over turbulent energy at the site (see next section and Discussion).

A.3.4 Comparison of Wave Removal Efficiencies for Reynolds Stress Calculations

The previous comparisons of the methods were only applied to a single individual burst of velocity data for each site. To compare the efficiencies of the methods in wave removal, the methods were applied to calculate Reynolds stresses from data collected over longer periods at both sites. For the South Bay, the data used were collected in the fall campaign at the benthic station in 8-minute bursts every 12 minutes at 10 Hz at a height of 36 cm above the bed over a roughly 2-day period of significant wave activity during a storm event with maximum wind speeds of above 17 m/s. For the RFS site we use roughly 3-minute bursts collected every 10 minutes at 8 Hz at a height of 33 cm above the bed over a single tidal period with significant wave contamination.

The time-series plots for both sites shows that in general, the wave removal methods are able to remove much of the wave contamination in the Reynolds stress calculations: Figures A.15 and A.16 show Reynolds stress time-series in the South Bay and RFS sites, respectively, and Figures A.17 and A.18 horizontal and vertical velocity variance at the RFS site. For the South Bay Reynolds stress time-series estimates (Fig. A.15), there appear to be certain wavy periods where the pressure and/or phase methods are less effective than the Shaw and Trowbridge method in removing waves (e.g. at d=271.8 and 272.2), which could be due to a number of reasons (see Discussion section). We note that the interpolation method seems to be the single-point method which most closely follows the behavior of the ST method, both validating it as an efficient single-point method of wave-turbulence decomposition when it can be unambiguously applied and providing some confirmation that both methods are working reasonably well, given that they arrive at such similar results despite having quite different procedures.

Figure A.19 is a scatterplot of the South Bay Reynolds stresses vs. the ST method over the same time period as that shown in Fig. A.15. Confirming our qualitative analysis from the burst comparisons, the interpolation method is more effective in matching the ST method than the pressure and phase methods, though in general the single-point methods reasonably agree ($R^2 \approx 0.55 - 0.82$).

Our analysis of the effectiveness of the single-point methods (Fig. A.19) assumes that the ST method is accurately removing wave contamination. To validate the ST method, we test whether

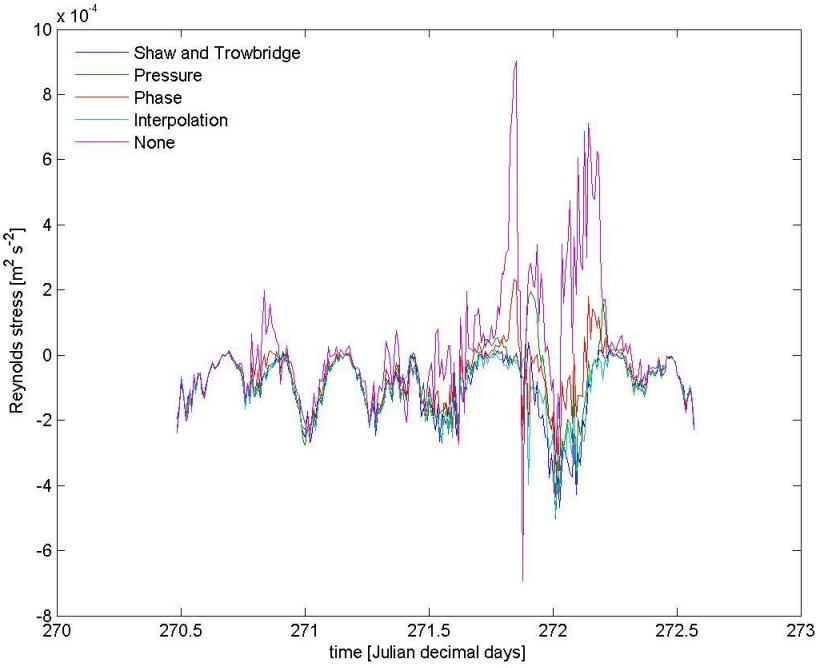

Figure A.15: Time-series plot of calculated turbulent Reynolds stresses at South Bay site. Both corrected data for each method and uncorrected (labeled None) data shown.

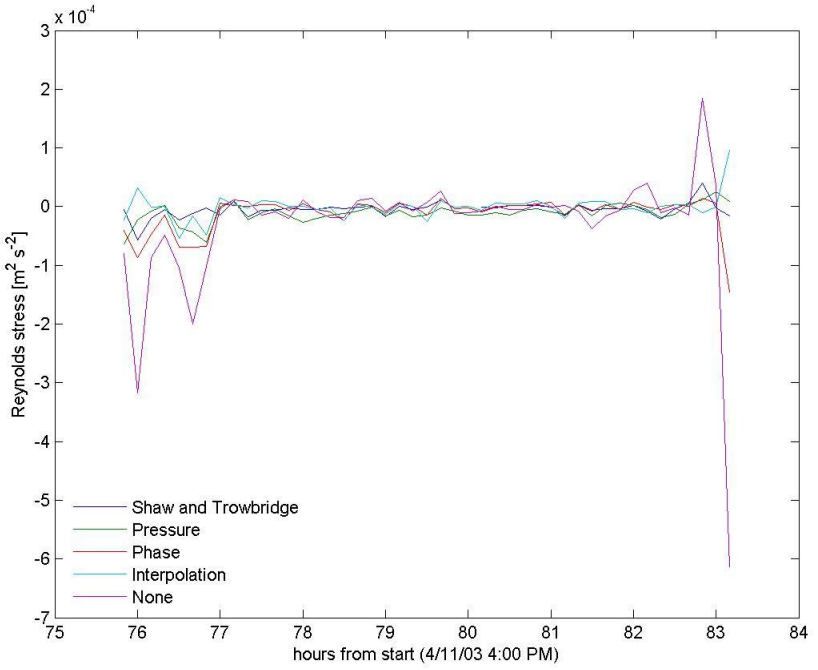

Figure A.16: Time-series plot of calculated turbulent Reynolds stresses at RFS site. Both corrected data for each method and uncorrected (labeled None) data shown.

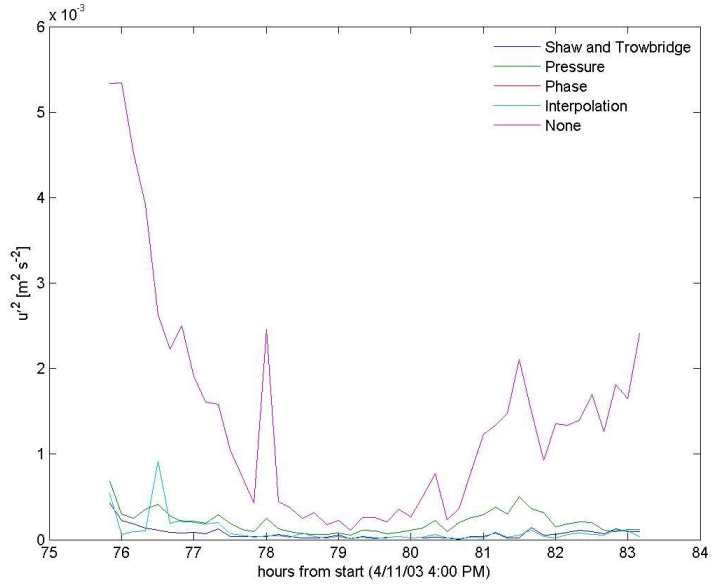

Figure A.17: Time-series plot of horizontal (u) component of velocity variance at RFS site. Both corrected data for each method and uncorrected (labeled None) data shown (for variance calculations Phase and Interpolation methods are equivalent).

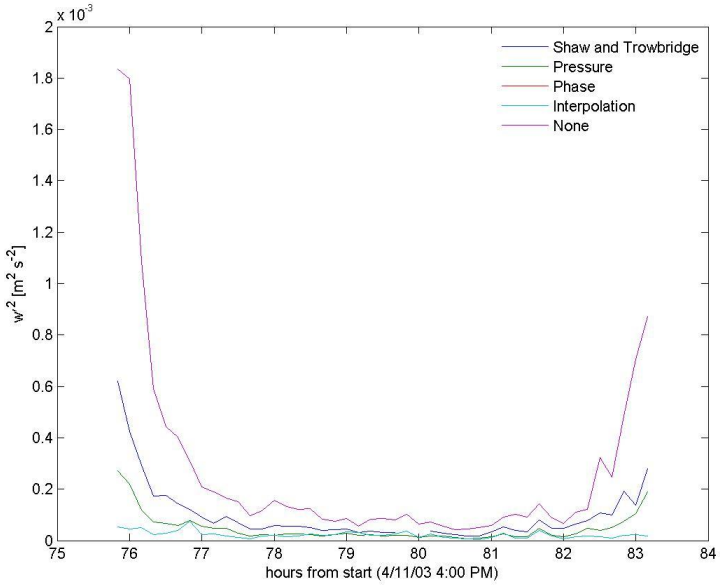

Figure A.18: Time-series plot of vertical (w) component of velocity variance at RFS site. Both corrected data for each method and uncorrected (labeled None) data shown (for variance calculations Phase and Interpolation methods are equivalent).

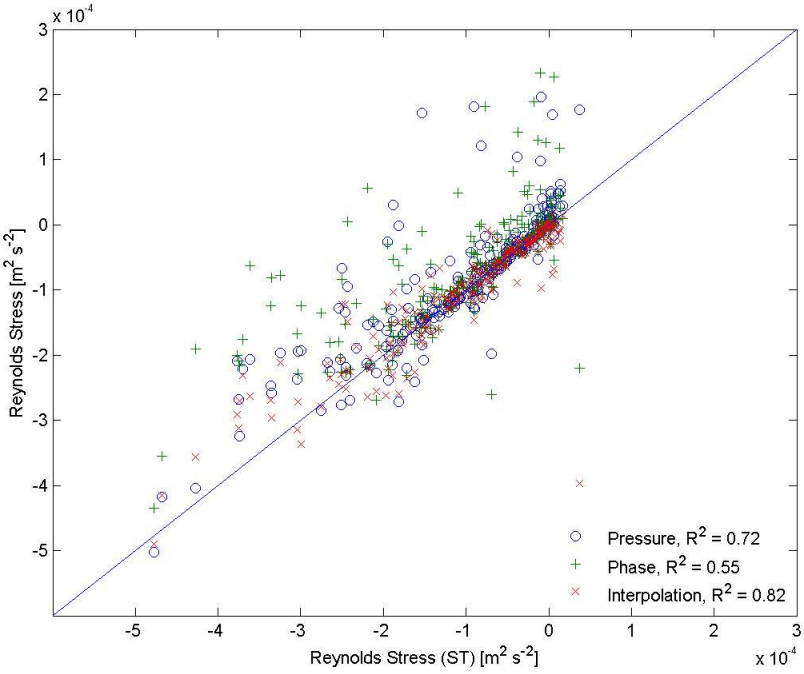

Figure A.19: Scatterplot of Reynolds stress data from South Bay site for each single-point method as plotted against results from the Shaw and Trowbridge method. R^2 for each method as compared to Shaw and Trowbridge also shown.

the results are consistent with simple drag-based estimates of Reynolds stress, using the constant stress layer assumption that $|\overline{u'w'}| = C_D U^2$, where C_D is a drag coefficient and U is the mean horizontal velocity. As a first check, we show a scatter plot of $|\overline{u'w'}|$ vs. U^2 (Figure A.20), based on 16 days of data that contains both wavy and non-wavy periods. If wave energy is incompletely removed, the scatter plot would show large variability. However, a least squares fit to the line yields a coefficient of determination of $□^2 = 0.83$, which indicates that wave removal is good and that a strong correlation exists between Reynolds stress and the mean tidal forcing (U^2), as expected by turbulence scaling. Further, the slope of the line—which represents the drag coefficient—yields $□_□ = 3.9 \times 10^{-3}$, a result that is consistent with previous estimates in shallow estuarine flows (Fong et al., 2009), perhaps slightly elevated due to wave-current boundary layer interactions (Grant and Madsen 1979). We next compare the Reynolds stress calculated using $C_d U^2$ with the ST method (Figure A.21). Any intermittent wave contamination in the ST method would show up as a large deviation from $C_d U^2$, and this is indeed what we observe for the uncorrected, raw Reynolds stress. However, except for a few periods in which the ST method and $C_d U^2$ slightly disagree, the overall agreement is quite good over both wavy and non-wavy periods. Hence, even in shallow water environments, the ST method effectively removes wave energy and produces turbulent statistics which are of a reasonable magnitude. Finally, we note that regressions of Reynolds stress estimates from the single-point methods to

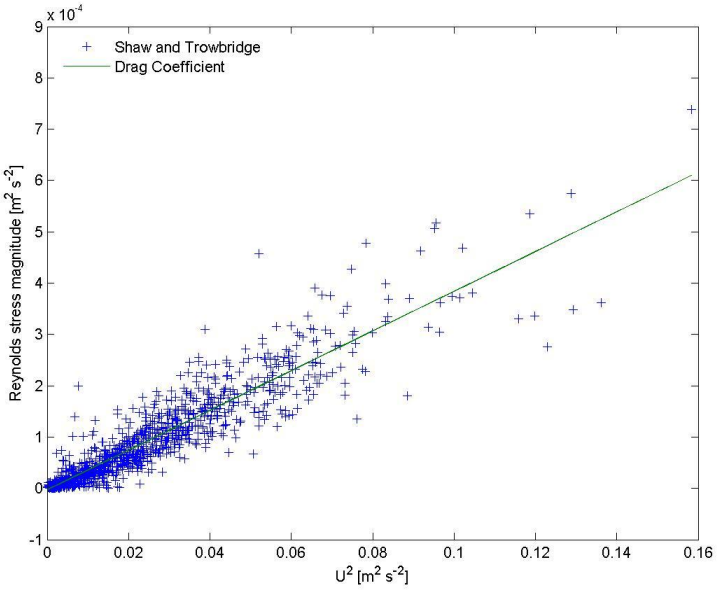

Figure A.20: Scatterplot of Reynolds stress maginitudes estimated from the ST method from the South Bay benthic station over a roughly 16-day period as plotted against mean velocity squared (U^2). Solid line shows drag coefficient relationship as predicted using a linear regression of the results ($\left|\overline{u'w'}\right| = C_D U^2$). ST method compared to drag prediction has $R^2 = 0.83$.

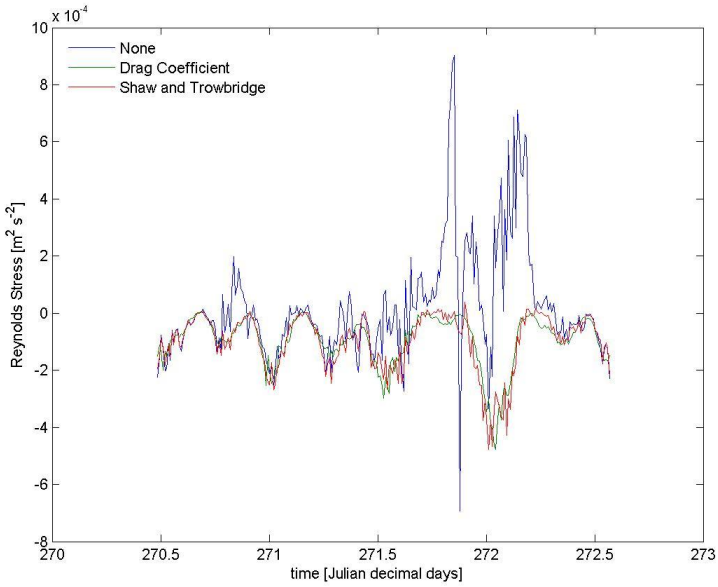

Figure A.21: Time series comparison of Reynolds stress estimates from raw data (labeled None), drag coefficient relationship, and Shaw and Trowbridge method. Drag coefficient results provide independent confirmation that Shaw and Trowbridge method is producing reasonable Reynolds stress estimates over wavy and non-wavy periods.

the drag-based ($C_D U^2$) estimates also produce reasonable agreement (R^2 = 0.71, 0.80, 0.57 for pressure, interpolation, and phase methods, respectively).

For the RFS data (Fig. A.16), a time-series plot of raw and corrected Reynolds stresses shows that all methods result in Reynolds stresses close to the noise floor of the WTD methods (estimated to be on the order of 1e-4 $(m/s)^2$ from the South Bay data, e.g. Fig. A.19), due to the small tidal currents (< 0.1 m/s). Assuming that Reynolds stress scales as the drag ($|\overline{\square'\square'}| = \square_{\square}\square^2$), and assuming a maximum wave-enhanced drag coefficient of 0.01 (Talke & Stacey, 2003), we find that the order of magnitude of Reynolds stress during the early flood at RFS should be approximately 1e-4 $(m/s)^2$ or less. Estimates indeed show this magnitude during the first few bursts, then decay as tidal currents reduce. Time-series plots of the variance of *u* and *w* before and after application of wave removal methods confirm that most of the energetic velocity fluctuations are indeed dominated by wave and not turbulent energy (Fig. A.17 and Fig. A.18). These results show that for the RFS data, all the WTD methods tested are successful in removing most of the wave contamination, although in this case the accurate resolution of turbulent statistics after waver removal is difficult due to the small magnitudes of turbulent energy and stresses being measured.

A.4 Discussion

As the purpose of this appendix is to compare the effectiveness of single-point methods, it is worth exploring in further detail the reasons why single-point methods may be less effective at wave removal under various conditions than the ST method. These reasons generally have to do with variability in wave phasing or directional spreading in complex wave environments. As discussed earlier, even the two-point ST method has shortcomings, which should be kept in mind when considering which method is likely to be most effectively applied under specific conditions.

Pressure Method: Wave Directional Spreading

From the individual burst comparisons for South Bay and RFS (Fig. A.13 and Fig. A.14), it can be seen that the pressure method can work very well for removing wave contamination in the Reynolds stresses. However, despite appearing to remove wave energy equally as well or better than the ST method for these bursts, this does not imply that the pressure method is always more effective in all situations. When the wave field is regular, the pressure method is indeed quite effective at wave removal, but problems for the pressure method arise if there is significant variability in the wave field, particularly from wave directional spreading (Agrawal and Aubrey 1992, Herbers and Guza 1993) that is caused by fluctuating wind direction, diffraction and refraction of waves, wave reflection, or wave interactions and harmonics.

Directional spreading of wave energy is often observed, especially in fetch-limited conditions where the wave environment is variable and not well-developed. When fetch-limited waves produce a wave field where directionality is variable or ill-defined, filtration of horizontal wave velocity data by the pressure method can introduce errors because pressure data gives no

information about wave directionality, and leads to poor wave filtration. Failure of the pressure method to completely remove wave fluctuations is most clearly observed in our data in the residual energy in the horizontal velocity *u* after application of the pressure method in the RFS data examples (Fig. A.17, also Fig. A.6 cf. Fig. A.4), and could also be a possible explanation for the periods in the South Bay data where the pressure method does not work as well.

Interpolation Method: Problems with Interpolating Wave-Influenced Turbulence Spectra

The interpolation method works well when the wave peak and turbulent inertial subrange are well-defined, as in the burst data from the South Bay. However, it is not always trivial to perform the necessary interpolation to remove the wave peak. If the wave peak or turbulent inertial subrange are poorly defined or difficult to identify across one or more bursts in data, the application of the method becomes ambiguous, and negatively impacts its effectiveness. Also, turbulent energy can be aliased into the wave energy and removed (Lumley & Terrary, 1983).

At the Richmond Field Station, both spectral methods were able to perform reasonably well in the removal of wave contamination in the Reynolds stress calculation, despite the relatively rough interpolation of the turbulent energy spectrum under the wave-dominated energy spectrum (Figs. A.8, A.10, A.16). However, it is possible that the success of the spectral methods for the RFS data despite the ambiguous interpolation of the spectra may be due in part to the fact that the domination of waves over turbulent energy resulted in the greater part of the energy being removed (Figs. A.17 and A.18). Hence, nearly all of the velocity correlation was in fact wave contributions, with the actual turbulent Reynolds stress much smaller in comparison. Because of this the spectral methods were able to remove roughly the correct magnitude of wave contamination, even though the true accuracy of the interpolation in separating waves and turbulence is obscured due to proximity of the actual Reynolds stresses to the noise floor of the methods.

Phase Method: Environmental Variability

All the WTD methods rely to some extent on the assumption that the statistics of the velocity field induced by waves and turbulence are constant or somewhat close to constant; however, the phase method appears to be particularly vulnerable to temporal variability in the wave field, due to the sensitivity of the phase calculation. As noted in the assessment, there may be ways to improve the performance of the phase calculation, such as increasing the number and decreasing the length of averaging windows in the calculation of the PSD, but this may come at costs such as loss of resolution of low frequencies. Because TKE and Reynolds stress are often dominated by low frequency motions, improving wave removal by such strategies may therefore have the unintended effect of biasing estimates of turbulent statistics low.

A.5 Comments and Recommendations

The results of this study show that various single-point methods of wave-turbulence decomposition can be employed as effective alternatives to the two-point method of Shaw and

Trowbridge (2001). These methods have been compared in terms of wave removal behavior and efficiency by examining energy spectra and ogives for calculating turbulent statistics before and after method application to burst velocity data, as well as aggregate comparisons of performance over long-term time-series velocity data, and have been found to perform reasonably well under a variety of environmental conditions. Though each method is also found to have specific shortcomings, these can be understood and minimized in order to choose and apply the most effective method in a given situation. For example, comparison of method effectiveness between the two sites in this study showed that wave directional spreading contributed to problems in applying the pressure method to horizontal velocity at the RFS site. In cases such as this, alternative methods to using pressure methods should be considered, though in cases where wave directional spreading is not a problem, the pressure method also performs as well or better than other methods. Also, our results showed that in both environments tested, using the interpolation method and ignoring the phase calculation yielded Reynolds stress results in as good or often better agreement with ST results than using the phase correction factor in the phase method. This suggests that the phase method should be restricted to environments where variability in wave phasing is low and phases of spectral wave fluctuations can be calculated accurately. The interpolation method can be substituted when horizontal and vertical wave motions are close to perfectly correlated, as occurs when instrument tilt is playing a role in establishing wave correlation in shallow environments such as in the cases evaluated here.

Ideally, environmental conditions can be characterized beforehand in order to choose the most appropriate wave removal method. For example, the presence of sea walls near the RFS site make it vulnerable to the problem of variations in wave directions, whereas the South Bay site is relatively open and farther from boundaries and thus can be expected to be less affected by this issue. Also, method choice may be affected by which turbulent quantity is of interest; for example, the pressure method may still be used to calculate Reynolds stress even when horizontal wave components are incompletely removed, since eliminating all vertical wave fluctuations is sufficient to remove all wave correlations in the Reynolds stress calculation. For sites with significant turbulent fluctuations at scales that are large compared to instrument spacing, the pressure method at low frequencies can be used to estimate error in the ST method. If environmental conditions in a field site are uncertain, multiple methods can and should be tested on field data in order to observe which method is working best in a certain environment. This can be done as in this study through qualitative comparisons of method behavior by examining individual burst spectra and cospectra, by comparison of the Reynolds stress to a drag coefficient relationship, or by bulk comparisons of total wave removal efficiency metrics (e.g. wave energy or stress removed) over extended wavy periods. These methods of assessment require additional analysis but have the added benefit of cross-checking different WTD methods to make sure that they are producing reasonable results. Finally, the results from this study have shown that single-point methods are generally effective at surface wave removal in estimating turbulent statistics in shallow tidal systems, performing reasonably well under most environmental conditions. An important implication of this work is that single-point methods

can be employed as a back-up alternative and check on the ST method, either in the case of limited availability of sensors or the failure of the ST method.